Climate Assessment for 1998

Gerald D. Bell,* Michael S. Halpert,* Chester F. Ropelewski,+ Vernon E. Kousky,*
Arthur V. Douglas,# Russell C. Schnell,@ and Melvyn E. Gelman*

ABSTRACT

The global climate during 1998 was affected by opposite extremes of the ENSO cycle, with one of the strongest Pacific warm episodes (El Niño) in the historical record continuing during January–early May and Pacific cold episode (La Niña) conditions occurring from July–December. In both periods, regional temperature, rainfall, and atmospheric circulation patterns across the Pacific Ocean and the Americas were generally consistent with those observed during past warm and cold episodes.

Some of the most dramatic impacts from both episodes were observed in the Tropics, where anomalous convection was evident across the entire tropical Pacific and in most major monsoon regions of the world. Over the Americas, many of the El Niño– (La Niña–) related rainfall anomalies in the subtropical and extratropical latitudes were linked to an extension (retraction) of the jet streams and their attendant circulation features typically located over the subtropical latitudes of both the North Pacific and South Pacific.

The regions most affected by *excessive* El Niño–related rainfall included 1) the eastern half of the tropical Pacific, including western Ecuador and northwestern Peru, which experienced significant flooding and mudslides; 2) southeastern South America, where substantial flooding was also observed; and 3) California and much of the central and southern United States during January–March, and the central United States during April–June.

El Niño–related rainfall *deficits* during 1998 included 1) Indonesia and portions of northern Australia; 2) the Amazon Basin, in association with a substantially weaker-than-normal South American monsoon circulation; 3) Mexico, which experienced extreme drought throughout the El Niño episode; and 4) the Gulf Coast states of the United States, which experienced extreme drought during April–June 1998. The El Niño also contributed to extreme warmth across North America during January–May.

The primary La Niña–related precipitation anomalies included 1) increased rainfall across Indonesia, and a nearly complete disappearance of rainfall across the east-central equatorial Pacific; 2) above-normal rains across northwestern, eastern, and northern Australia; 3) increased monsoon rains across central America and Mexico during October–December; and 4) dryness across equatorial eastern Africa.

The active 1998 North Atlantic hurricane season featured 14 named storms (9 of which became hurricanes) and the strongest October hurricane (Mitch) in the historical record. In Honduras and Nicaragua extreme flooding and mudslides associated with Hurricane Mitch claimed more than 11 000 lives. During the peak of activity in August–September, the vertical wind shear across the western Atlantic, along with both the structure and location of the African easterly jet, were typical of other active seasons.

Other regional aspects of the short-term climate included 1) record rainfall and massive flooding in the Yangtze River Basin of central China during June–July; 2) a drier and shorter-than-normal 1997/98 rainy season in southern Africa; 3) above-normal rains across the northern section of the African Sahel during June–September 1998; and 4) a continuation of record warmth across Canada during June–November.

Global annual mean surface temperatures during 1998 for land and marine areas were 0.56°C above the 1961–90 base period means. This record warmth surpasses the previous highest anomaly of +0.43°C set in 1997. Record warmth was also observed in the global Tropics and Northern Hemisphere extratropics during the year, and is partly linked to the strong El Niño conditions during January–early May.

*Climate Prediction Center, NCEP/NWS/NOAA, Washington, D.C.

+International Research Institute for Climate Prediction, Palisades, New York.

#Creighton University, Omaha, Nebraska.

@Climate Monitoring and Diagnostics Laboratory, NOAA, Boulder, Colorado.

Corresponding author address: Michael S. Halpert, Climate Prediction Center, NCEP/NOAA, W/NP52, NSC, Rm. 605, 5200 Auth Rd., Camp Springs, MD 20746.

Table of Contents

1. Introduction

This annual climate assessment is the ninth in an ongoing series produced by the Climate Prediction Center. It is designed to provide a timely summary of the global climate system during 1998. Specific components of the assessment include a documentation of global climate variations, an examination of oceanic and atmospheric anomalies in the global Tropics and extratropics, and an analysis of selected significant regional climate highlights.

Issues related to global and regional climate change, including atmospheric temperatures, ozone, carbon dioxide, and snow cover are addressed in section 2. In section 3 an analysis is presented of the very strong Pacific warm episode (El Niño) conditions that continued during January–May 1998, and the development of Pacific cold episode (La Niña) conditions during the second half of the year. The impacts of these extremes in the El Niño/Southern Oscillation (ENSO) cycle on the wintertime jet streams in both the Northern and Southern Hemispheres are also examined. Regional climate highlights and summaries of the major monsoon systems are discussed in section 4. Topics include severe flooding during June–August in the Yangtze River basin of central and eastern China, a very active North Atlantic hurricane season, a summary of the rainy seasons in southern and western Africa, extreme heat and drought in the south-central and southeastern United States during April–June, and temperature and precipitation highlights over South America. In section 5, seasonal maps of temperature anomalies, precipitation percentiles, and 500-hPa heights and anomalies are presented. These maps are included for reference, and to continue the set of maps that have appeared in previous annual climate assessments. Although each section is essentially self-contained, there is liberal cross-referencing between sections to aid navigation through the document.

A variety of data sources were used in the compilation of this assessment, including 1) gridded analyses from the National Centers for Environmental Prediction–National Center for Atmospheric Research (NCEP–NCAR) Climate Data Assimilation System (CDAS)/Reanalysis Project (Kalnay et al. 1996), 2) surface data obtained from the operational Global Telecommunications System, 3) satellites, 4) radiosondes, and 5) ship reports. Selected analyses were also obtained from international climate data centers. It should be noted that due to the variety of different data sources used in this assessment, it is not possible to maintain a consistent base period among all fields for anomaly computations.

2. Climate and global change issues

a. *Surface temperature*

The estimated 1998 global mean temperature over land and marine areas combined (based on data collected from over 1000 land-based weather stations and approximately 7000 ships and 1000 ocean buoys) was +0.56°C above the 1961–90 base period mean (Fig. 1a), which made it the warmest year in the historical record dating back to 1860. This value far exceeded the previous estimated record departure of +0.43°C set in 1997. Estimated global mean temperatures have been above the 1961–90 average for the past 20 years, with the last below-average annual global temperature recorded in 1978 (Fig. 1a). Also, the three warmest years in the record (1995, 1997, and 1998) have occurred in the past four years. The very strong 1997/98 Pacific warm episode (see section 3b) contributed substantially to the record-breaking temperatures observed in both 1997 and 1998.

Record annual temperatures were also set in both the Northern Hemisphere (Fig. 1b) and Southern Hemisphere (Fig. 1c) during 1998. The Southern Hemisphere anomaly of +0.47°C exceeded the previous record set in 1997 by 0.12°C, while the Northern Hemisphere anomaly of +0.64° surpassed the 1995 record anomaly by 0.11°C.

By partitioning the globe into the extratropics (30°–90°N, 30°–90°S) and Tropics (30°S–30°N), it becomes evident that record temperatures were also observed during 1998 in both the global Tropics and Northern Hemisphere extratropics. In the Tropics, the annual mean value of 0.60°C above the 1961–90 mean exceeded the previous record anomaly of 0.43°C set in 1997 (Fig. 2a). In the Northern Hemisphere extratropics, the 1998 value slightly surpassed the previous record anomaly set in 1995 (Fig. 2b). In the Southern Hemisphere extratropics the 1998 temperature anomaly was similar to that observed in 1990 but below the record value set in 1993 (Fig. 2c). In each of these three regions, temperatures have averaged well-above normal during most of the 1990s.

Annual land-only temperature (Fig. 3a) and ocean-only temperature (Fig. 3b) records were also set in 1998. The land-only temperature averaged more than 1.0°C above the 1880–1997 base period mean, and was approximately 0.3°C warmer than the previous
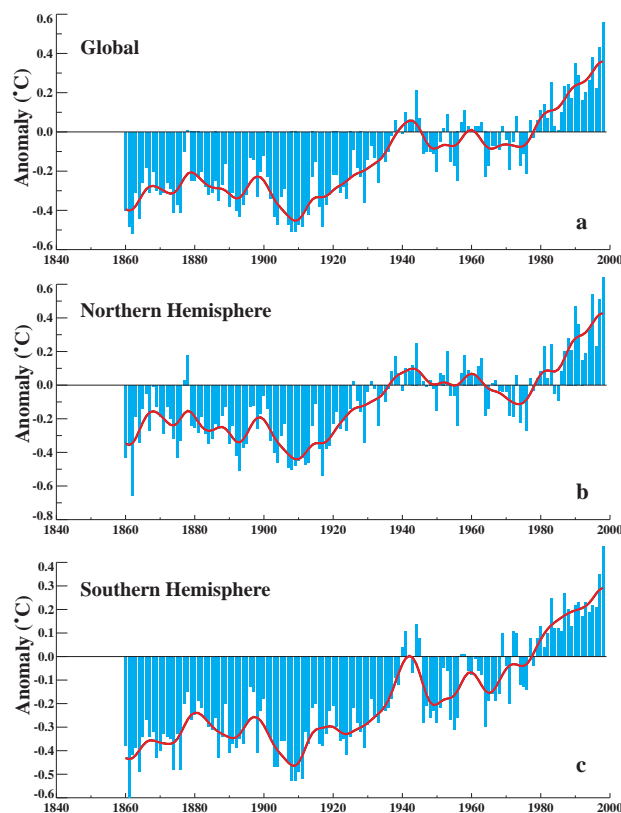
FIG. 1. Annual averages of combined land–air temperature and SST anomalies (blue bars, °C): (a) global, (b) Northern Hemisphere, and (c) Southern Hemisphere. Anomalies are departures from the 1961–90 base period means. Smoothed values (red curve) were obtained using a 13-term Gaussian filter designed to suppress variations on timescales less than 10 yr. (Source: Hadley Centre for Climate Prediction and Research, United Kingdom, and Climatic Research Unit, University of East Anglia, United Kingdom.)

FIG. 2. Annual averages of combined land–air temperature and SST anomalies (blue bars, °C): (a) Tropics, (b) Northern Hemisphere extratropics, and (c) Southern Hemisphere extratropics. Anomalies are departures from the 1961–90 base period means. Smoothed values (red curve) were obtained using a 13-term Gaussian filter designed to suppress variations on timescales less than 10 yr. (Source: Hadley Centre for Climate Prediction and Research, United Kingdom, and Climatic Research Unit, University of East Anglia, United Kingdom.)

record set in 1995. The ocean-only average temperature was 0.51°C above the 1880–1997 base period mean, which exceeded the previous record anomaly of 0.47°C set in 1997. In both of these time series annual mean temperatures have been above average every year since 1977.

During 1998 the pattern of annual temperature anomalies (Fig. 4) was dominated by above-normal temperatures across most of the globe between 30°S and 60°N, with the strong El Niño (see section 3) contributing to above-average temperatures throughout the Tropics and across North America. Below-average temperatures were observed primarily over the Southern Hemisphere oceans south of 30°S, across the central North Pacific, over the central tropical Pacific, and over northern Russia. Over the central tropical Pacific Ocean (160°E and 130°W) the below-normal sea sur-
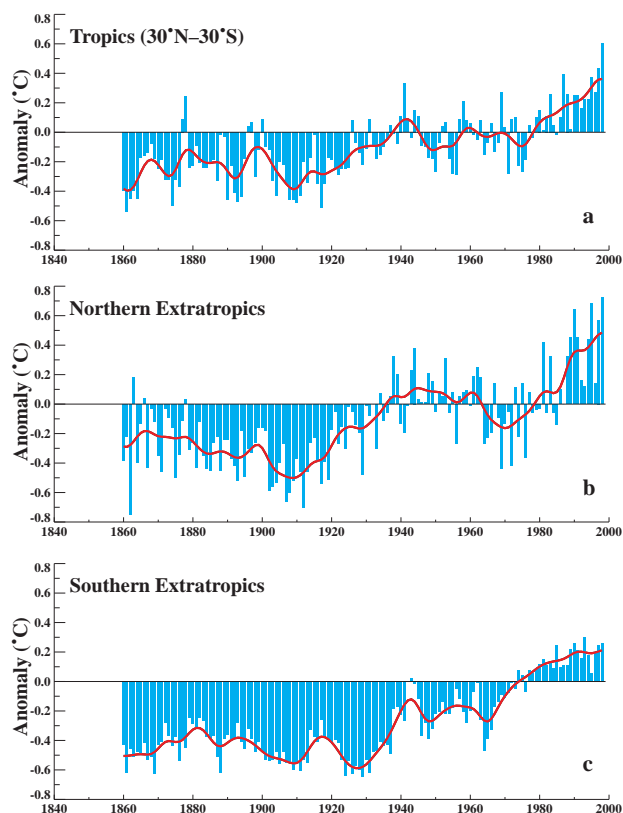
face temperatures (SSTs) reflected the rapid demise of El Niño conditions during May and the subsequent development of La Niña conditions (see section 3d). In contrast, annual temperatures in the eastern tropical Pacific averaged 1°–2°C above normal, as SSTs were above average from January–August. Over the tropical and subtropical Atlantic and Indian Oceans, SSTs were also above normal during most of 1998, with the largest anomalies observed during December 1997–February 1998 (DJF) (see section 5, Fig. 63) and March–May (MAM) (see section 5, Fig. 65).

Over the land areas, the most prominent regions of above average annual temperatures during 1998 included most of North America, all of southern Europe and southern Asia, and all of northern Africa (Fig. 4). Over North America, annual mean temperatures ranged from 1.0°–3.0°C above normal across Canada,

with the largest anomalies observed over the Northwest Territories. Overall, Canada recorded it warmest year in the 51-yr record (Fig. 5a), as annual mean temperatures were 2.5°C above the 1951–80 base period mean and more than 0.5°C greater than the previous record set in 1981. National average seasonal temperature records were set in Canada during MAM, June–August (JJA), and September–November (SON) 1998, with DJF 1997–98 the second warmest such period on record. Individual monthly national temperature records were set during February, April, May, July, August, and September, with July being the warmest month in the historical record for that country.

Over the contiguous United States, annual mean 1998 temperatures averaged 1.2°C above the 1961–90 mean, which is the nation's second warmest year in the historical record (Fig. 5b). Temperatures over the eastern half of the country averaged 1.0°–2.0°C above normal for the year as a whole, while below-average temperatures were confined to the far West (Fig. 4). Eleven states located mainly in the Midwest and the Northeast set annual record temperatures during 1998, and 22 states recorded annual temperatures that ranked in the top five of the 104-yr record dating back to 1895 (Fig. 6). California was the only state to record below-average annual mean temperatures during the year. It is interesting to note that the overall warmth observed over the United States during the 1980s and 1990s is comparable to that recorded during the 1920s and 1930s.

Annual mean temperatures across Europe and Asia were generally higher than average during 1998 in the region south of 60°N, and lower than average farther north (Fig. 4). Over northeastern Asia, temperatures averaged 0.5°–2.0°C below normal, with negative anomalies recorded during DJF, MAM, and SON (see section 5, Figs. 63, 65, 69). During SON temperatures averaged more than 4°C below normal across central Siberia (see section 5, Fig. 69). These conditions contrast with the much-above-normal temperatures that had previously prevailed throughout this region during much of the past two decades (e.g., Hurrell 1995).

Over southeastern Asia temperatures averaged 1°–2°C above normal for the year, with positive temperature anomalies observed during all four sea-
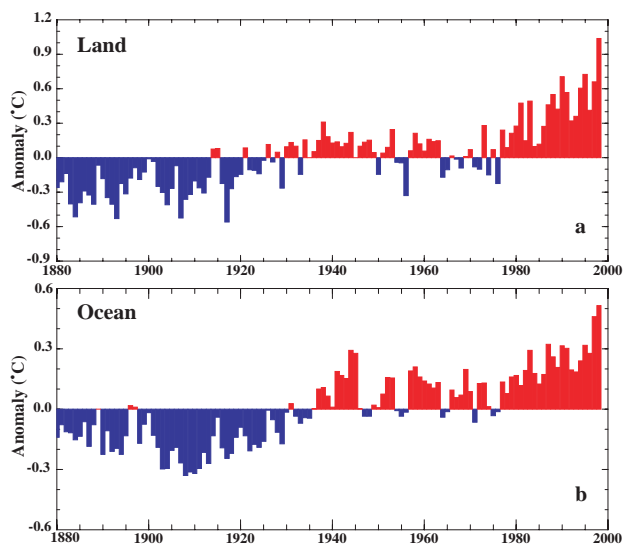

FIG. 3. Annual averages of global (a) land–air temperature and (b) SST anomalies (°C). Anomalies are departures from the 1880–1997 base period means. (Source: National Climatic Data Center.)

sons (see section 5, Figs. 63, 65, 67, 69). In Japan, the annual mean temperature was the highest in the 101-yr record (1.3°C above average), which broke the previous record anomaly of 1.2°C set in 1990 (Fig. 5c). Seasonal temperatures over most of Japan averaged more than 1.0°C above normal during all four individual seasons, with record warmth observed during MAM. More than 90% of the Japanese network of stations set springtime record high temperatures, and 75% of the country observed record high October temperatures.

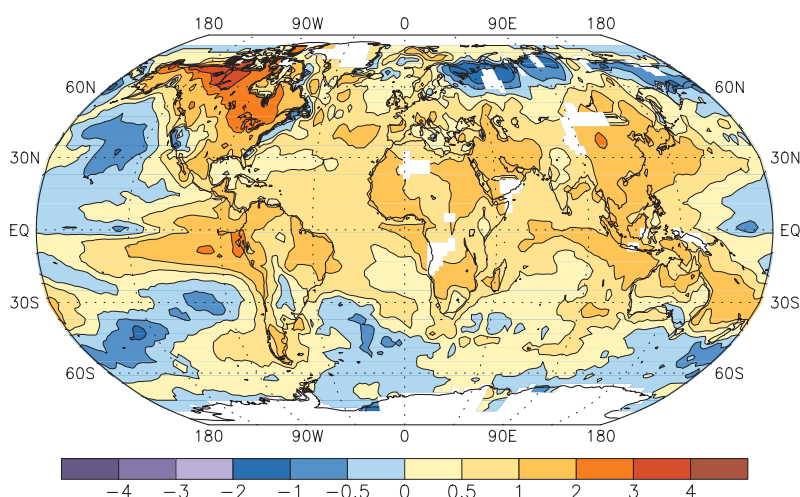FIG. 4. Annual surface temperature anomalies (°C) for 1998. Analysis is based on station data over land and on SST data over the oceans. Anomalies are departures from the 1961–90 base period means. White areas are regions with insufficient data for analysis.
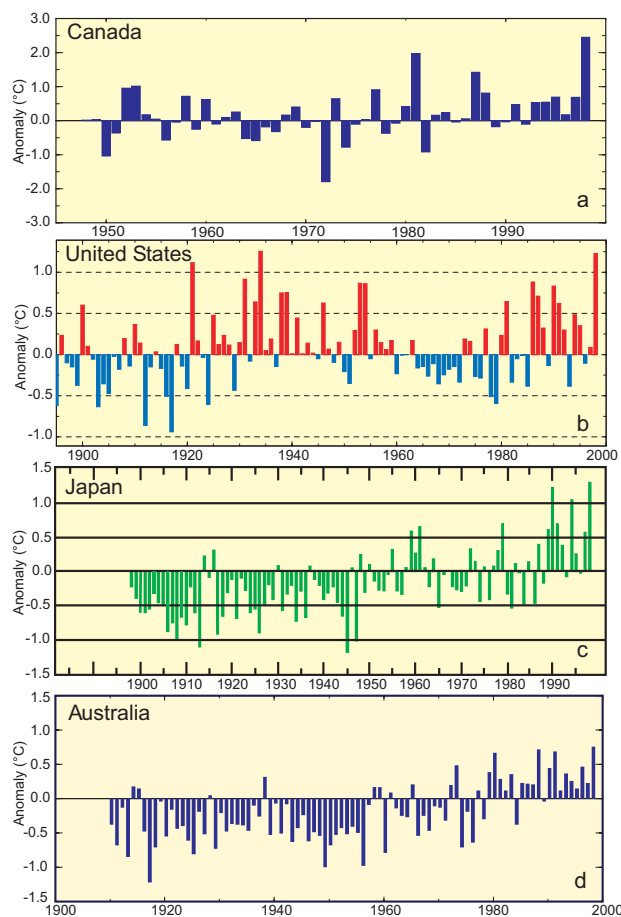
FIG. 5. Annual surface temperature anomalies (°C) for (a) Canada, (b) the contiguous United States, (c) Japan, and (d) Australia. Anomalies are departures from the (a) 1951–80, (b) 1880–1997, and (c, d) 1961–90 base period means. (Sources: (a) Environment Canada, (b) National Climatic Data Center, (c) Japanese Meteorological Agency, and (d) Australian Bureau of Meteorology.)
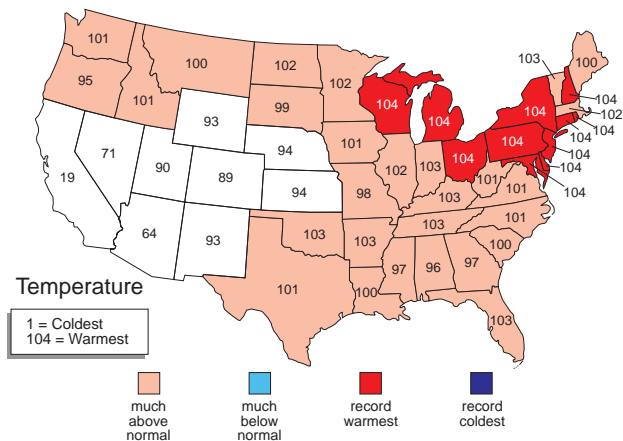

FIG. 6. 1998 annual United States statewide temperature rankings relative to the past 104 yr dating back to 1895. (Source: National Climatic Data Center.)

In the Southern Hemisphere annual temperatures during 1998 averaged 0.5°–2.0°C above normal across most of Australia, southern Africa, and South America, while below-average temperatures were confined to extreme south-central Australia and central South America (Fig. 4). These conditions were generally prominent during all four seasons. In both New Zealand (not shown) and Australia (Fig. 5d), annual mean high temperature records were set in 1998. Australia recorded its highest annual mean temperature (0.73°C above the 1961–90 base period mean) dating back to 1910, which surpassed the previous largest anomaly of 0.69°C set in 1988. Record high minimum temperatures played a major role in this record, as the mean maximum temperature (0.43° above average) was significantly below the previous

highest maximum departure (0.85°C) observed in 1991. According to the Australian Bureau of Meteorology, the higher land temperatures were partly linked to above average SSTs around the country, which developed during the middle of the year in conjunction with the onset of Pacific cold episode conditions (see section 3d).

b. Tropospheric–stratospheric temperatures

1) TROPOSPHERE

Global estimates of mean tropospheric temperatures are obtained from satellite observations and from the NCEP–NCAR reanalysis system (Kalnay et al. 1996). The satellite estimates are obtained from channels 2 and 2R of the Microwave Sounding Unit (MSU) (Spencer et al. 1990; Spencer and Christy 1992) on the National Oceanic and Atmospheric Administration (NOAA) series of polar-orbiting satellites, and are updated and modified in real time by J. Christy (1998, personal communication). The peak in the channel 2 weighting function varies from 400 hPa at extreme scan position to 700 hPa at nadir position. In contrast, the peak in the channel 2R weighting function is near 750 hPa.

To facilitate comparisons between satellite-derived and reanalysis-derived global annual mean tropospheric temperatures (Fig. 7a), the reanalysis data are subjected to a discretized vertical weighting function having the same shape as the channel 2 weighting function. The reanalysis data are used as a replacement for radiosonde-based estimates, which are no longer available in time for this assessment. Overall, time series of global annual mean temperature anomalies
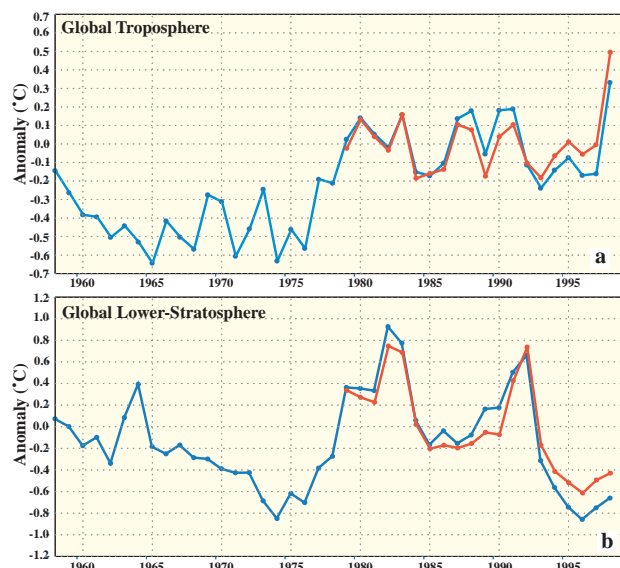
FIG. 7. Global annual mean temperature anomalies (°C) derived from the MSU (red line) and from the CDAS/reanalysis (blue line) in the (a) troposphere and (b) lower stratosphere. Tropospheric temperatures are derived using the MSU channel 2 weighting functions (Spencer et al. 1990). Anomalies are departures from the 1979–95 base period means. (MSU data provided by the University of Alabama in Huntsville.)

derived from both channel 2 and reanalysis data exhibit the same general behavior during the past twenty years. A more detailed intercomparison of these datasets can be found in Chelliah and Ropelewski (1999, manuscript submitted to *J. Climate*).

According to the MSU- (reanalysis-) based estimates, the annual mean global tropospheric temperature during 1998 was 0.5°C (0.33°C) above the 1979–95 base period mean. These are the largest positive anomalies observed in the record, and are the first large positive anomalies observed since the eruption of Mount Pinatubo in 1991. Both datasets also show a record increase in temperature of approximately 0.5°C between 1997 and 1998. The second largest year-to-year increase in global mean tropospheric temperatures (0.4°C) occurred from 1976 to 1977, coincident with major changes in the atmospheric circulation noted previously by several authors (e.g., Trenberth 1990).

The spatial pattern of annual tropospheric temperature anomalies during 1998 derived from channel 2R of the MSU (Fig. 8a) shows generally above-average temperatures between 30°S and 60°N, and below-normal temperatures at high latitudes in the Southern Hemisphere. Negative temperature anomalies were also observed over northeastern and northwestern Russia. This global pattern is very similar to the pattern of annual mean *surface* temperature anomalies (Fig. 4).

Lower-tropospheric temperature anomalies exhibited marked differences between the first and second halves of the year (Figs. 9a,b). These differences largely reflect the influence of warm episode conditions during January–May and cold episode conditions during the second half of the year. During both periods there is considerable zonal symmetry to the anomaly patterns throughout the Tropics, subtropics, and extratropics, as well as considerable interhemispheric symmetry, which is also typical of extremes in the ENSO cycle.

During January–June (Fig. 9a) the zonally symmetric features included abnormally warm temperatures throughout the Tropics and the subtropics of both hemispheres, and a local minimum in temperature anomalies near the 30° latitude band in both hemispheres. These anomalies reflected an increased meridional temperature gradient in the lower midlatitudes of both hemispheres, and a decreased meridional temperature gradient in the 40°–55° latitude bands. These
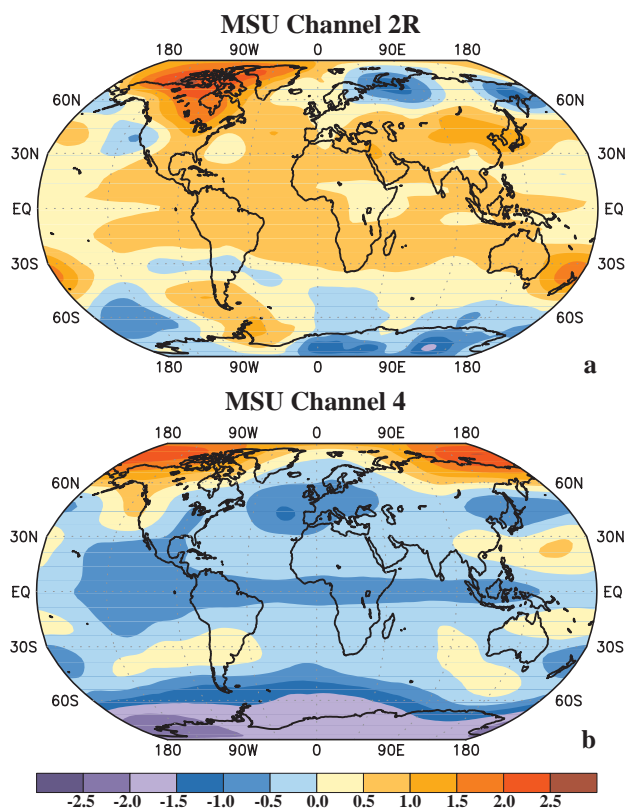
FIG. 8. Annual mean temperature anomalies (°C) during 1998 in the (a) troposphere and (b) lower stratosphere, derived from channel 2R and channel 4 of the MSU, respectively. Anomalies are departures from the 1979–95 base period means. (MSU data provided by the University of Alabama in Huntsville.)

January–June 1998

July–December 1998

FIG. 9. Mean tropospheric temperature anomalies (°C) for (a) January–June 1998 and (b) July–December 1998 derived from the MSU channel 2R. Anomalies are departures from the 1979–95 base period means. (MSU data provided by the University of Alabama in Huntsville.)

conditions are consistent with increased westerlies near 30° latitude in both hemispheres and with decreased westerlies in the 40°–55° latitude bands (see section 3, Figs. 27a,b). They are also consistent with an overall equatorward shift in strong westerly winds in both hemispheres during the period.

In contrast the July–December period (Fig. 9b) featured a relative minimum in mean tropospheric temperature anomalies in the Tropics and subtropics, and a relative maximum in the middle latitudes between 30°–40° latitude bands of both hemispheres. These features reflected both a decreased meridional temperature gradient in the lower midlatitudes of both hemispheres and an increased meridion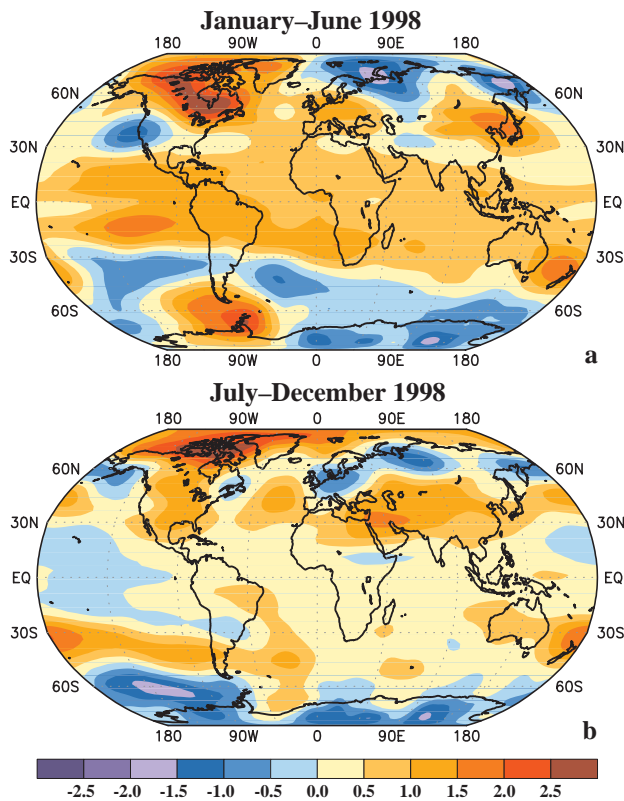al temperature gradient in the 40°–55° latitude bands. These conditions are consistent with decreased westerlies near 30° latitude in both hemispheres and with increased westerlies in the 40°–55° latitude bands (see section 3, Fig. 27d). They are also consistent with an overall poleward shift in strong westerly winds in both hemispheres during the period.

There is also considerable zonal asymmetry evident in the temperature anomaly patterns during both periods, with the largest anomalies observed over the Pacific sector of both hemispheres and over the Americas. These patterns strongly reflect the teleconnective response of the atmospheric circulation to opposite extremes in the ENSO cycle. For example, large positive temperature anomalies in the subtropics of both hemispheres during January–June were collocated with the ENSO-related subtropical anticyclonic circulation anomalies observed at upper levels flanking the region of enhanced tropical convection (see section 3, Figs. 27a,b). These anomalies reflected a dramatic weakening of the upper-level mid-Pacific trough in both hemispheres, and a pronounced eastward extension of the subtropical ridges to well east of the date line (see section 3c). In contrast, the mean July–December conditions were consistent with La Niña–related subtropical cyclonic circulation anomalies at upper levels flanking the region of suppressed tropical convection (see section 3, Fig. 27d). These anomalies reflected a strengthening of the mid-Pacific trough in both hemispheres and a westward retraction of the subtropical ridges toward the western Pacific (see section 3d).

In the middle latitudes, the January–June period featured negative temperature anomalies over both the North and South Pacific, which is consistent with the observed pattern of below-normal heights in these regions (see section 5, Figs. 64, 66). In contrast, positive temperature anomalies and above-normal heights were observed in these regions during July–December.

Large positive temperature anomalies were also observed over Canada and the northern United States during January–June. In combination with the anomaly pattern over the North Pacific, these conditions during winter are consistent with a substantially more zonally-uniform temperature field across the eastern North Pacific and North America than is evident in the climatological mean. More zonally uniform height and wind fields also accompanied these conditions, consistent with the ongoing strong El Niño episode during the period. Specific circulation features that accompanied these conditions (see also section 3b) included 1) a pronounced eastward extension and southward shift of the East Asian jet stream to the southwestern United States; 2) a strengthening of the subtropical jet stream across northern Mexico, the southern United States, and the Gulf of Mexico; 3) a pronounced weakening of the Hudson Bay low; and

4) substantially reduced northwesterly flow throughout central North America.

In the Southern Hemisphere, the January–June temperature anomaly pattern is also consistent with increased jet stream winds across the eastern South Pacific and South America, which produced increased storminess and above-normal rainfall across central South America and the western South Atlantic (see section 4d). These conditions are similar to those observed during the July–December 1997 period, which also featured a pronounced extension of the wintertime jet stream from Australia to the west coast of South America.

In contrast, the temperature and circulation features over the South Pacific during July–December 1998 reflected a westward retraction of the jet steam to Australia (see section 3d, Fig. 31b). This jet structure is consistent with the La Niña–related amplification of the mid-Pacific trough and westward retraction of the subtropical ridge toward the western South Pacific.

2) LOWER STRATOSPHERE

Global estimates of lower-stratospheric temperatures are derived from channel 4 of the MSU and from the NCEP–NCAR reanalysis. The peak in the channel 4 weighting function varies from 70 hPa at extreme scan position to 100 hPa at nadir position. Both analyses show that 1998 was the sixth consecutive year with below-average temperatures (Fig. 7b). During the past 20 years the character of the two time series has been dominated by major volcanic eruptions (i.e., El Chichón in 1982 and Mount Pinatubo in 1991), with above-normal lower-stratospheric temperatures observed immediately after these eruptions followed by a rapid drop in temperatures for several years. Global lower-stratospheric temperatures reached a minimum in 1996 and subsequently increased slightly during 1997 and 1998.

During 1998 the MSU-estimated temperatures averaged 0.4°C below the 1979–95 means, which is the fourth lowest value in the 20-yr record. The reanalysis-estimated temperatures averaged 0.63°C below the 1975–95 means, which is the seventh lowest value dating back to 1958.

The spatial pattern of lower-stratospheric annual temperature anomalies during 1998 (Fig. 8b) shows below-normal temperatures throughout the high latitudes of the Southern Hemisphere, much of the global Tropics and subtropics, and the middle latitudes of the Northern Hemisphere. Large positive strato-

spheric temperature anomalies were evident only at high latitudes of the Northern Hemisphere. This overall anomaly pattern has many features similar to those observed during the July–December 1997 period (Bell and Halpert 1998).

During January–June 1998, lower-stratospheric temperatures were below average throughout the global Tropics and subtropics, over the North Atlantic and Europe, and over the high latitudes of the South Pacific and South Atlantic (Fig. 10a). In the Tropics and subtropics (especially across the central Pacific), negative temperature anomalies were found above an elevated tropopause in association with the El Niño–related enhanced convection and anomalous subtropical anticyclones (see section 3c). These temperature anomalies are opposite to those observed in the troposphere (Fig. 9a).

During July–December 1998, lower-stratospheric temperatures warmed considerably throughout the global Tropics, consistent with the demise of the El Niño conditions and the subsequent development of La Niña
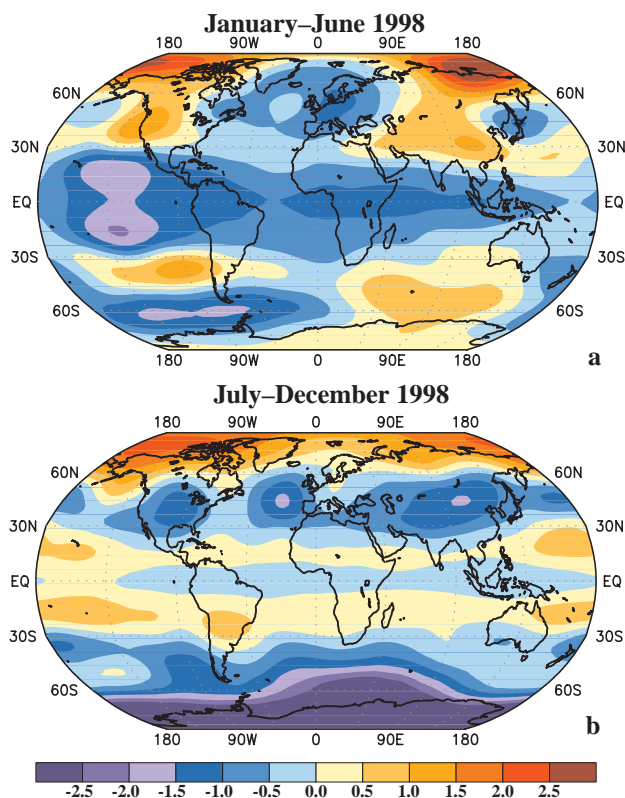

FIG. 10. Mean stratospheric temperature anomalies (°C) for (a) January–June 1998 and (b) July–December 1998 derived from the MSU channel 4. Anomalies are departures from the 1979–95 base period means. (MSU data provided by the University of Alabama in Huntsville.)

conditions. This warming was also associated with a transition to the easterly phase of the stratospheric quasi-biennial oscillation during the year.

In the extratropics January–June temperatures in the lower stratosphere were above normal across the eastern Pacific in both hemispheres, reflecting a lowered tropopause along the cyclonic-shear side of the enhanced westerly jets. Between the Tropics and extratropics the reversal in the sense of the anomalous temperature gradient from that observed in the troposphere (Fig. 9a) is consistent with an increased tropopause slope, and with an anomalously strong decrease in westerly winds with height above the jet stream level. Opposite conditions were observed during July–December (Fig. 9b) over the eastern Pacific in association with the development of La Niña conditions.

Over Antarctica above-average lower-stratospheric temperatures were observed during January–June (Fig. 10a), while significantly below-normal temperatures were observed during July–December 1998 (Fig. 10b). In both periods, these conditions are similar to those observed in 1997. During August–November 1998 these extremely low temperatures were associated with increased ozone destruction due to high chlorofluorocarbon concentrations in polar stratospheric clouds. A record size of the Antarctic ozone hole was measured during October–November [see section 2c(1)].

c. Trace gases
1) Ozone

Total column ozone data were obtained from the National Aeronautics and Space Administration *Nimbus-7* SBUV instrument from 1979 through 1988, from the *NOAA-11* SBUV/2 instrument from January 1989 through August 1994, from the *NOAA-9* SBUV/2 instrument from September 1994 through June 1997, and from the *NOAA-14* SBUV/2 beginning July 1997. Data from the SBUV instruments are only available during daylight viewing conditions; therefore no data are available over polar latitudes during winter. Other sources of ozone data include Dobson spectrophotometer readings and measurements from balloon-borne ozonesondes, both obtained from the NOAA Climate Monitoring and Diagnostics Laboratory (CMDL).

(i) Continental United States

CMDL operates a network of eight Dobson ozone spectrophotometers across the contiguous United States, in addition to instruments at Barrow, Alaska; Mauna Loa, Hawaii; and American Samoa. These instruments provide daily total column ozone amounts (weather and sun permitting), and many Dobson stations have been in operation since the early 1960s. Over the continental United States a large annual cycle in total ozone amounts (Fig. 11a) is evident, resulting from stratospheric ozone transport processes that cause a winter–spring maximum and summer–fall minimum. Since 1980 the average total ozone amount has decreased by about 5%, due mainly to the chemical destruction of stratospheric ozone in reactions with anthropogenic halocarbon compounds. The largest decrease in total ozone occurred from 1979 through 1993 (Fig. 11b). From 1994 to 1998 total ozone concentrations over the continental United States have remained fairly constant, at levels approximately 5% below the 1980 average.
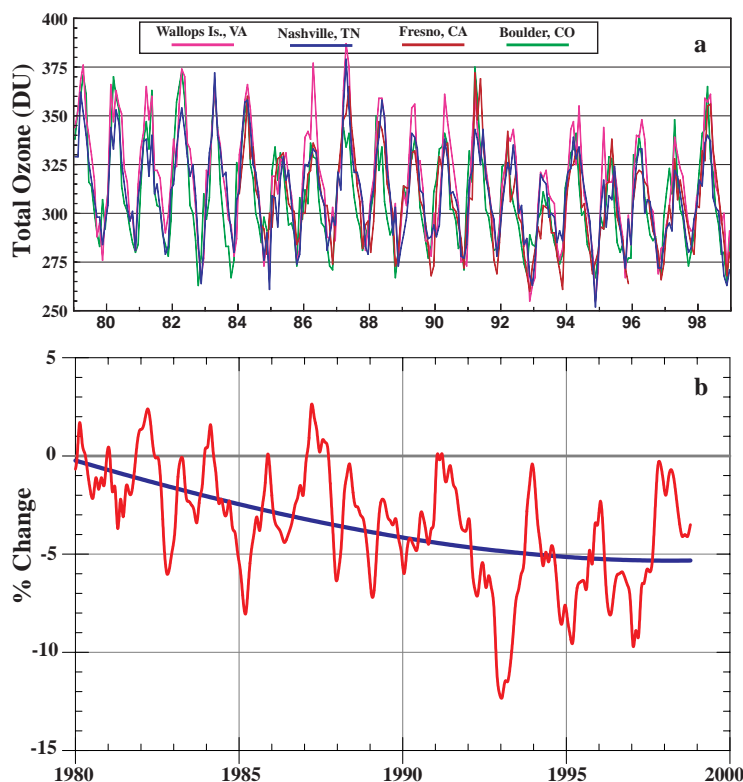

Fig. 11. (a) Monthly average total ozone (DU) and (b) monthly average total column ozone loss (% change) at four midlatitude stations spanning the central United States. Ozone loss is relative to 1980. The blue curve in (b) is a parabolic fit to the ozone loss with 1980 set to 0. (Analysis provided by CMDL.)
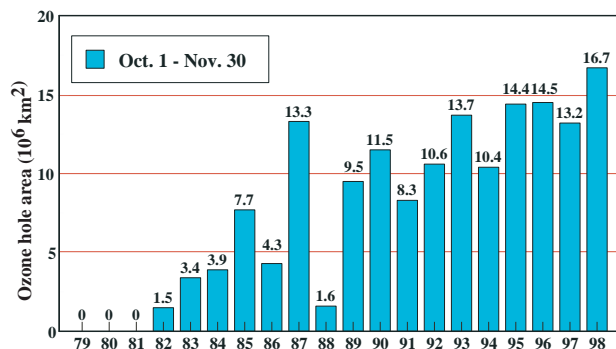
FIG. 12. Average area of the Antarctic ozone hole (total ozone < 220 DU) between 1 October and 30 November as detected by the SBUV/2 instrument on the NOAA polar orbiting satellites .

(ii) Southern Hemisphere

Total column ozone in the Southern Hemisphere also exhibits a well-defined annual cycle, with the lowest values typically observed over Antarctica during September–November. It is in this region that the "ozone hole" is located, denoted by total column ozone concentrations of less than 220 Dobson units (DU). The ozone hole is usually well developed in September and typically reaches its maximum areal extent in late September and early October. It then usually persists well into November and generally disappears by December. The ozone hole first began to appear over the Antarctic region in the early 1980s (Farman et al. 1985). During the past 20 yr (Fig. 12), the average October–November size of the ozone hole area has increased, from a small area of 1.5×10^6 km^2 in 1982 to a record area of 16.7×10^6 km^2 in 1998. This value surpasses the previous record of 14.5×10^6 km^2 set in 1996.

Daily measurements for the period 1987–98 show a record areal extent of the ozone hole during most of October–November 1998 (Fig. 13a), with a maximum extent of more than 25×10^6 km^2 (an area larger than North America) observed during late September. The 1998 ozone hole also persisted into mid-December, which is longer than has been observed in any previous year. This duration is nearly 1 month longer than was observed in 1997, when the ozone hole disappeared by mid-November.

A further inspection of ozone concentrations during 1998, obtained from a sounding at the South Pole on 3 October 1998 (Fig. 14), shows the complete absence of ozone between 15 and 21 km, which is comparable to the vertical extent of ozone depletion observed in 1997. These conditions contrast with the
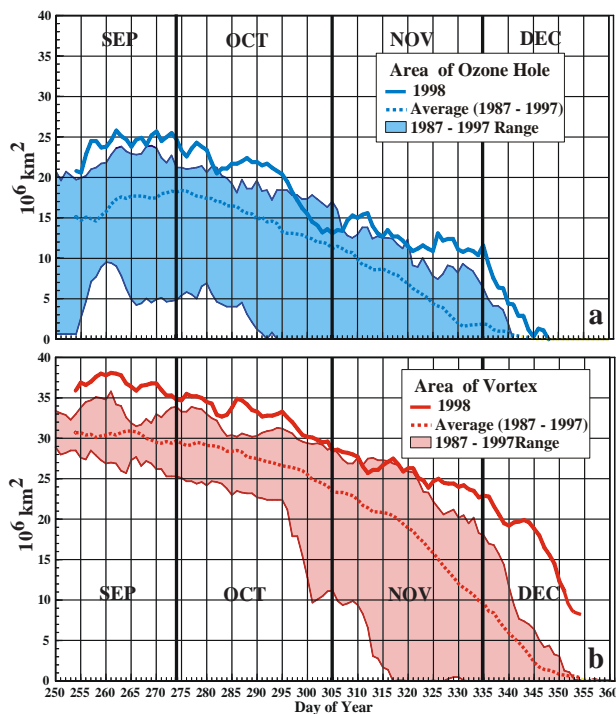

FIG. 13. (a) Area of Antarctic ozone hole (total ozone < 220 DU) and (b) size of the Southern Hemisphere polar vortex (defined by the 32-PVU contour enclosed area on the 450-K isentropic surface) from 6 September 1998 to 31 December 1998.

"pre–ozone hole" period (1967–71) when no ozone depletion was detected between 15 and 20 km, and also with conditions earlier in 1998 before the development of the ozone hole. During 1998, the lowest daily total column ozone concentration within this region was 98 DU. This value is second to the record low concentration of 86 DU measured in 1993.

Total ozone concentrations are closely coupled to lower-stratospheric temperatures through photochemistry. Extremely low stratospheric temperatures (below $-78°$C) contribute to the formation of polar stratospheric clouds, which enhance the production and lifetime of reactive chlorine, thereby leading to ozone depletion (WMO/UNEP 1994). During most of the Southern Hemisphere winter and spring of 1998, the minimum temperatures in the polar region reached or exceeded previous record low values (Fig. 15) and were again sufficiently low to allow for enhanced ozone depletion.

The areal extent of the ozone hole is also closely related to the polar vortex (Fig. 13b), which isolates and concentrates the chemicals that destroy ozone at low temperatures. During most of September– December 1998, this stratospheric polar vortex was
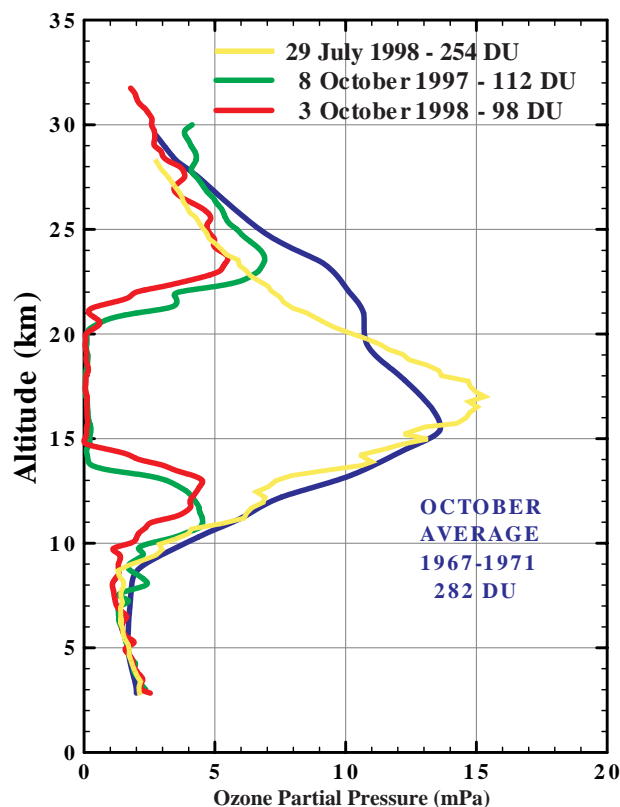
FIG. 14. Ozone profile (partial pressure, mPa) measured by balloon-borne ozonesonde at the South Pole on 3 October 1998 (red line) and comparisons to the October 1967–71 mean (blue line), the 8 October 1997 profile (green line), and the 29 July 1998 profile (yellow line).
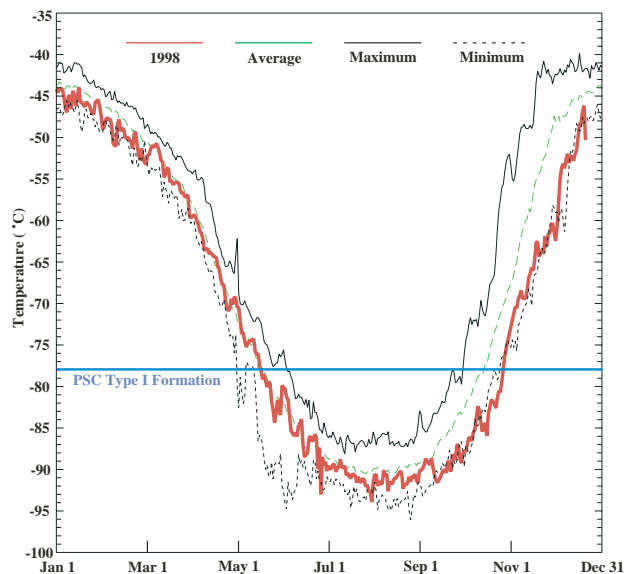

FIG. 15. Daily minimum temperatures at 50 hPa in the region 65°–90°S for 1998 (red line). Mean daily values for the period 1979–97 are shown in green. Record daily maxima (solid black) and minima (dashed black) are also shown. The horizontal blue line indicates the temperature that contributes to the formation of polar-stratospheric clouds.

larger and persisted longer than has been observed previously in the historical record.

A scientific assessment by the World Meteorological Organization (WMO) and UNEP states that the abundance of ozone-depleting substances in the stratosphere is expected to peak by the year 2000. Even though international actions are working well to reduce the use and release of ozone depleting substances, chemicals already in the atmosphere will continue ozone depletion into the twenty-first century. Changing atmospheric conditions and natural ozone variability are expected to complicate the task of detecting the start of the ozone layer recovery. Based on an analysis of 10 yr of ozone vertical profile measurements, Hofmann et al. (1997) estimate that the recovery of the Antarctic ozone hole may not be conclusively detected until the year 2008.

2) CARBON DIOXIDE

The Mauna Loa Observatory is located at an elevation of 3350 m on the flank of Mauna Loa volcano and is an ideal site for carbon dioxide measurements. There is no nearby vegetation, and the prevailing nighttime downslope winds give a representative sampling of midtropospheric air from the central North Pacific Ocean. Thus, the CO_2 record based on measurements at this observatory is taken as a reliable index of long-term carbon dioxide growth. This record is the longest of its kind in existence and shows a continued increase of CO_2 through 1998 (Fig. 16). This result indicates that fossil fuel consumption and deforestation continue to add CO_2 to the atmosphere at a rate faster than uptake by the oceans and biosphere.

The increase in CO_2 concentration has averaged approximately 1.4 ppm yr^{-1} during the 1980s and 1990s but with significant year-to-year variability in the growth rate. The growth rate decreased to 0.5 ppm yr^{-1} during the aftermath of the Mount Pinatubo eruption in 1991 and subsequently increased to more than 2 ppm yr^{-1} during 1995 before dropping back to near 1.4 ppm^{-1} in 1996. The growth rate then increased during 1998 to more than 3 ppm yr^{-1}, which is the highest rate observed since measurements began in 1957. Contributing factors to these interannual variations in growth rate are 1) temperature and precipitation over large areas, which influence the growth of plants and the decay of soil organic matter, and 2) variations in
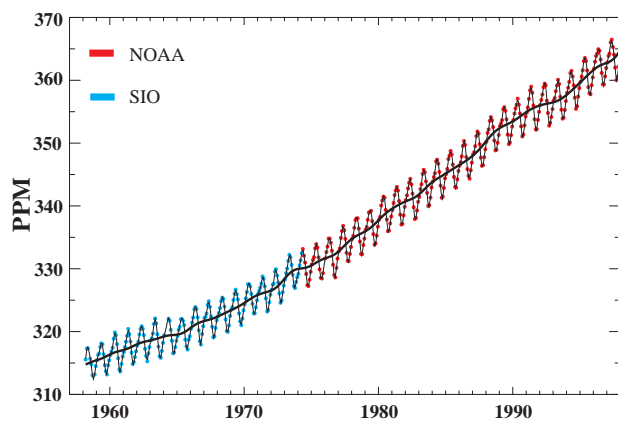
FIG. 16. Monthly mean carbon dioxide concentrations (ppm) measured at Mauna Loa, HI. The black line is the 12-month running mean. The data through April 1974 are from C. D. Keeling at Scripps Institute of Oceanography (SIO, blue dots), and the data since May 1974 are from NOAA (red dots). (Analysis provided by CMDL.)
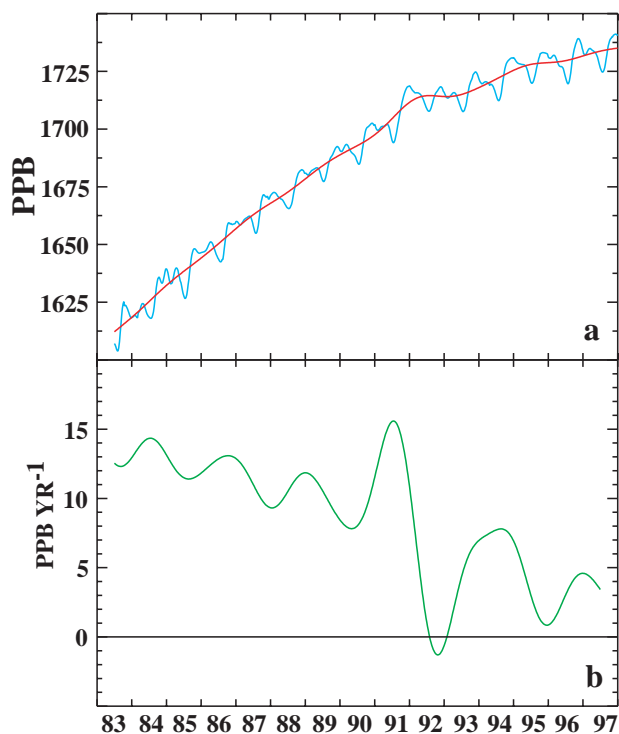

FIG. 17. (a) Globally averaged biweekly methane mixing ratio (ppb) and (b) globally averaged methane growth rate. The red curve in (a) represents the long-term trend. (Analysis provided by the Carbon Cycle Group cooperative air sampling network at CMDL.)

the partial pressure of CO_2 in surface seawater. The large increase in the growth rate during 1998 may have been related to the record warmth experienced during the year.

3) METHANE

The amount of methane in the earth's atmosphere has more than doubled since preindustrial times (Etheridge et al. 1992). This increase is responsible for approximately 20% of the estimated change in direct radiative forcing of the earth's climate due to anthropogenic greenhouse gas emissions (Myhre et al. 1998). Recent measurements by CMDL indicate that although methane concentrations continue to increase, the rate of increase has slowed considerably since the early 1990s (Fig. 17). If global methane and hydroxide emissions remain constant, then globally averaged methane concentrations are projected to increase to approximately 1800 ppb over the next few decades (1997 values are 1730 ppb), with little further change expected in its contribution to the greenhouse effect (Dlugokencky et al. 1998).

4) GLOBAL CHLOROFLUOROCARBONS (CFCS)

The concentrations of two types of ozone depleting CFCs and three types of ozone depleting chlorinated solvents are monitored by CMDL at eight locations from Alert, Northwest Territories, Canada, and Point Barrow, Alaska, to the South Pole (Fig. 18). Each of these five substances show markedly reduced growth rates from those observed in the early 1990s,

with some species showing significant declines in concentration since 1994. These trends are related directly to an end of production of these substances on 1 January 1996 in the developed countries. However, the production of these chemicals continues in a few lesser developed countries.

The atmospheric growth rate of CFC-12 is decreasing with time as a result of emission reductions, although concentrations of this long lifetime atmospheric gas have not yet peaked. CFC-12 was used in pre-1993 auto air conditioners, as an aerosol propellant, and in refrigerators. The accumulation of CFC-11 in the atmosphere peaked during 1993–94 and has been decreasing since that time. CFC-11 was used as a cell-blowing agent for the manufacture of foams, in large air conditioning systems, and in refrigeration. Atmospheric trends of the shorter lifetime chlorinated solvents methyl chloroform (CH_3CCl_3), carbon tetrachloride (CCl_4), and CFC-113 (CCl_2F-$CClF_2$) have all been decreasing at various rates during the 1990s. The concentration of CH_3CCl_3 has decreased most rapidly and has been cut in half between 1993 and 1998. This chemical was used as a metal degreaser in manufac-
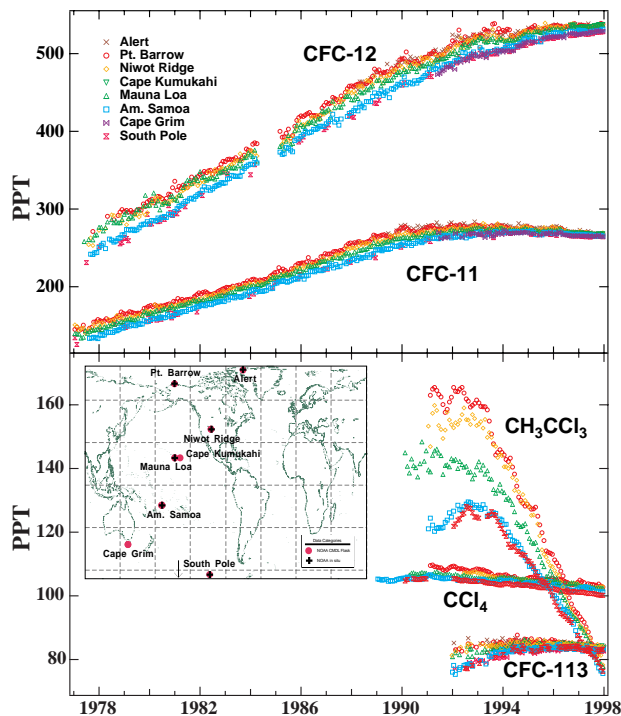
FIG. 18. Trends of various controlled ozone-depleting chlorine species. (Analysis provided by CMDL.)

turing. The concentration of CCl_4 has decreased slowly since 1991. This chemical was used in dry cleaning and in the production of CFCs. The concentrations of CFC-113 have been slowly decreasing since 1995. This chemical was used as a degreaser solvent in the manufacture of circuit boards.

d. Northern Hemisphere snow cover

The areal extent of Northern Hemisphere snow cover during 1998 was below the 1972–97 mean in every month except October (Fig. 19a). During February the snow cover extent was the second lowest in the historical record for that calendar month, eclipsed only by February 1995 conditions.

With the exception of 1996, the 12-month running mean of snow cover extent has been below normal over the hemisphere since 1987. This contrasts with the above-average areal extent of snow cover observed throughout the 1970s. This interdecadal variability in snow cover extent is evident over both Eurasia (Fig. 19b) and North America (Fig. 19c).

Over Eurasia the 1998 snow cover extent (Fig. 19b) was generally below average during January–June and above-average during SON. The DJF 1997/98 season featured a reduced southward extent of the wintertime snow pack across both eastern Asia and western Rus-

sia/eastern Europe (Fig. 20a) and increased snow cover in the region east of the Caspian Sea. The dipole pattern of anomalies in these regions was linked to a large-amplitude atmospheric circulation pattern at upper levels (see section 5, Fig. 64), characterized by a strong ridge over Europe and a very strong trough extending southward from western Siberia to the Caspian Sea. This circulation contributed to anomalously high temperatures across Europe and western Russia (see section 5, Fig. 63) and to reduced precipitation over portions of western Russia (see section 5, Fig. 63), thus leading to reduced snow cover in these regions. Farther east, it contributed to lower-than-normal temperatures and above-normal precipitation, which led to increased snow cover east of the Caspian Sea.

The MAM season featured an early springtime retreat of the snowpack over eastern Asia and a delayed snowmelt across western and central Russia (Fig. 20b), while the SON season featured an expanded region of snow cover across most of Asia and eastern Europe (Fig. 20c). In both seasons, these conditions are consistent with the locations of the upper-level ridges and troughs, and with the attendant temperature and precipitation patterns.

In North America the areal extent of snow cover was below normal throughout the year (Fig. 19c), with record low values observed in February, May, and June and near-record low values observed in January, April, and November. In mid-1998 the 12-month running mean of anomalous snow cover extent dropped a to record low value of -1.0×10^6 km^2.

In Canada, snow cover extent was below normal in all seasons (Fig. 20), as record warmth dominated the country during much of the year (Figs. 4, 5a). In the United States, snow cover was below normal during DJF across the Midwest, the Ohio Valley, and much of the mid-Atlantic region (Fig. 20a), and above-normal in the West. This above-normal snow cover then continued in the West during MAM and was also evident in portions of the central plains states (Fig. 20b).

In both Canada and the United States these conditions were linked to an anomalous upper-level atmospheric circulation that extended across the North Pacific and North America in association with ongoing strong El Niño conditions (see section 3c). Prominent aspects of this circulation included 1) increased zonal flow across the continent, along with significantly reduced northwesterly flow, 2) a very powerful wintertime jet stream and enhanced storm activity over the eastern North Pacific and west-central United States, and 3) an overall shift of the win-
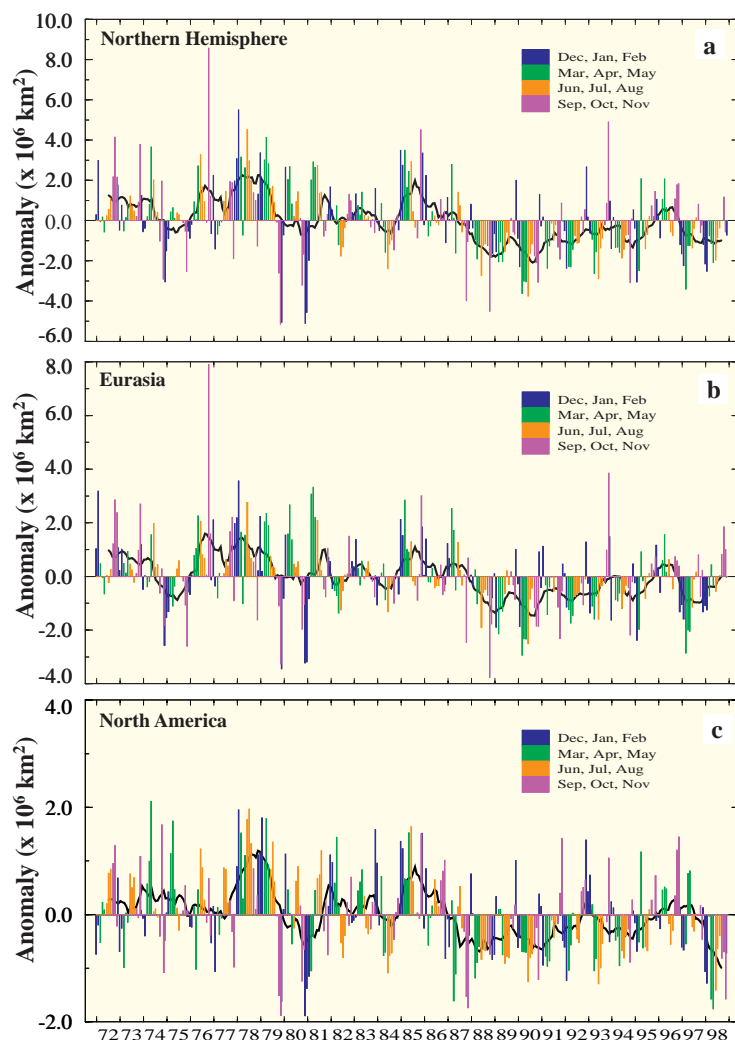
FIG. 19. Anomalies of monthly snow cover extent over (a) the Northern Hemisphere, (b) Eurasia, and (c) North America. Smoothed curve is a 12-month running mean. Anomalies are departures from the 1972–97 base period means. (Analysis provided by Rutgers University.)

eastern United States. During SON, a snow cover deficit of 0.7×10^6 km² and a delayed development of the snowpack were again observed across Canada (Fig. 20c), as extremely warm temperatures persisted across the country.

3. The strong 1997–98 El Niño and transition to a La Niña episode

a. Overview

The global climate during 1998 was affected by both extremes of the ENSO cycle (Fig. 21), with one of the strongest El Niño episodes in the historical record continuing during January–early May and La Niña conditions occurring from July through the remainder of the year. Across the eastern Pacific these ENSO extremes were evident in the time series of subsurface temperature anomalies (Fig. 21a); low-level (850 hPa) equatorial easterly wind anomalies (Fig. 21b); SST anomalies (Fig. 21c); anomalous tropical convective activity, as measured by anomalies of outgoing longwave radiation (OLR) (Fig. 21d); and upper-level (200 hPa) height anomalies (Fig. 21e).

From January through May 1998 strong warm episode conditions contributed to major regional rainfall (Fig. 22) and temperature anomalies over large portions of the Tropics and extratropics, which are generally consistent with those observed during past warm episodes (Ropelewski and Halpert 1987, 1989; Halpert and Ropelewski 1992). El Niño impacts during the period included 1) a continuation of severe drought in Indonesia; 2) a continuation of strong convection and increased rainfall across the eastern half of the tropical Pacific (Figs. 21d, 22); 3) flooding, mudslides, and extremely heavy rainfall in Peru; 4) a continuation into February of the rainy season and strong convective activity across equatorial eastern Africa; 5) below-normal rainfall and forest fires in the Amazon Basin; 6) increased storminess and rainfall over southeastern South America; 7) a wet and stormy 1997/98 winter season across the southern tier of the United States and California; 8) an extremely mild 1997/98 winter and spring season across

tertime jet stream and storm track toward the southern tier of the United States.

These conditions contributed to a widespread flow of mild, marine air throughout the continent and to record warmth across Canada. In the United States the increased storminess contributed to abundant snowfall and above-normal snow cover over the mountainous regions of the West. Also, many of these storms and their attendant cold-frontal boundaries were completely de-coupled from the cooler Canadian air masses to the north. This combination of increased marine air throughout the northern United States, and a nearly complete absence of cold-air outbreaks from Canada, contributed to extremely mild conditions and below-normal snow cover extent across the central and

DJF 1997/98 a

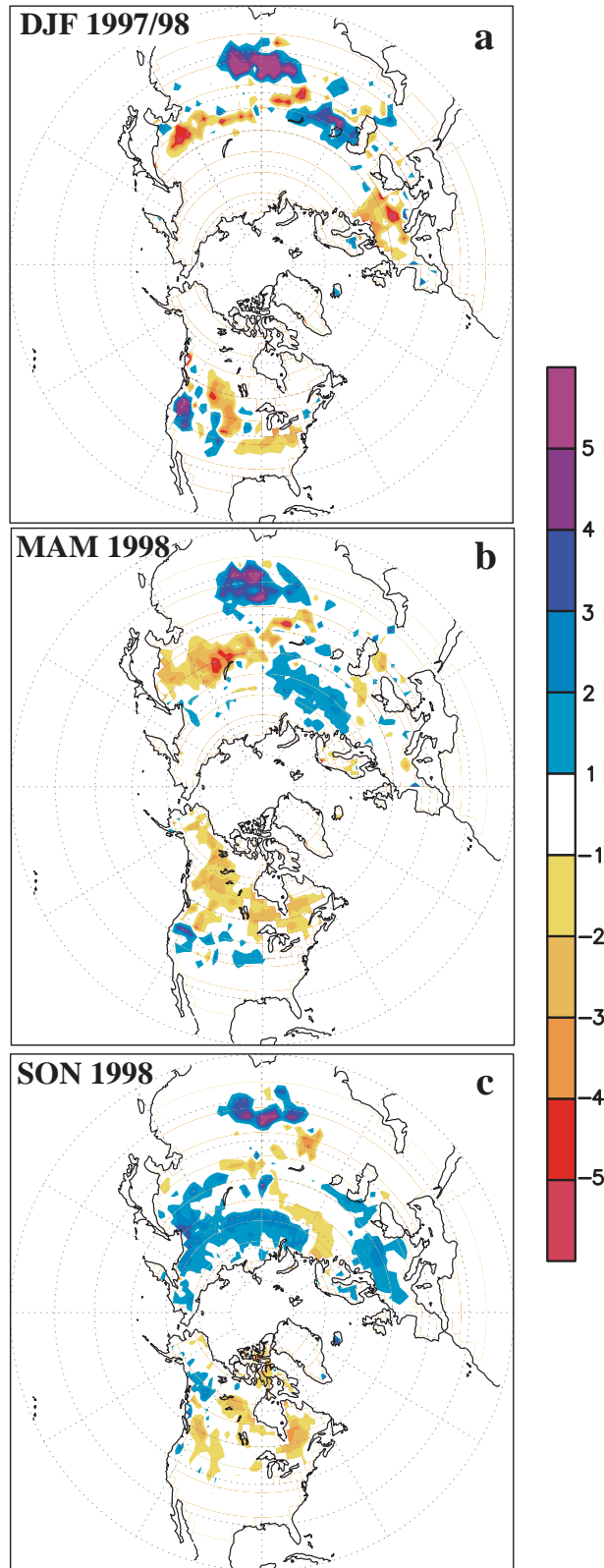**MAM 1998** b

SON 1998 c

FIG. 20. Snow cover duration anomaly (weeks) during (a) December 1997–February 1998, (b) March–May 1998, and (c) September–November 1998. Values are derived from an operational analysis of visual imagery by NOAA/NESDIS. Anomalies are departures from the 1972–98 base period means.
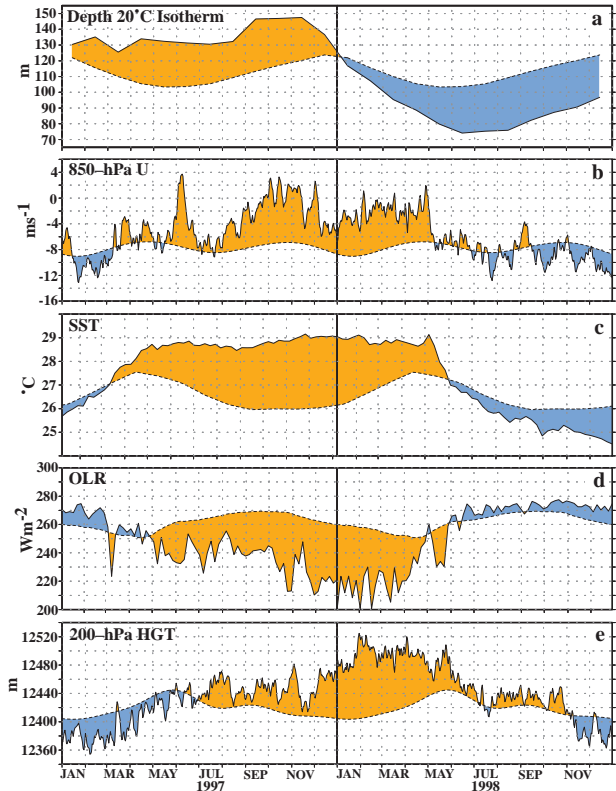

FIG. 21. Monthly time series of (a) the depth of the 20°C isotherm (m), (b) 850-hPa zonal wind speed (m s^{-1}), (c) SST (°C) (d) OLR (W m^{-2}), and (e) 200-hPa height (m). Values in (a)–(d) are determined by averaging over the region bounded by 5°N–5°S and 180°–100°W; in (e) over the region 20°N–20°S and 180°–100°W. The solid curve in all panels shows the monthly mean values and the dashed curved shows the climatological mean. The anomalies are shown shaded, with orange (blue) shading indicating positive (negative) anomalies. The climatology and anomalies are computed with respect to the 1979–95 base period means.

North America, with record temperatures observed over portions of Canada and the United States; 9) extensive dryness and wildfires in Mexico during March–May; 10) record heat and drought across the south-central United States during April–June [see section 4a(2)]; and 11) persistent dryness over the Hawaiian Islands.

Cold episode conditions during the second half of the year also impacted global temperature and precipitation patterns in a manner consistent with past cold episodes (Ropelewski and Halpert 1989; Halpert and Ropelewski 1992). These impacts included 1) above-normal rainfall across Indonesia (Fig. 23); 2) a nearly complete disappearance of rainfall across the east-central equatorial Pacific; 3) a weakening and westward retraction of the wintertime jet stream across the
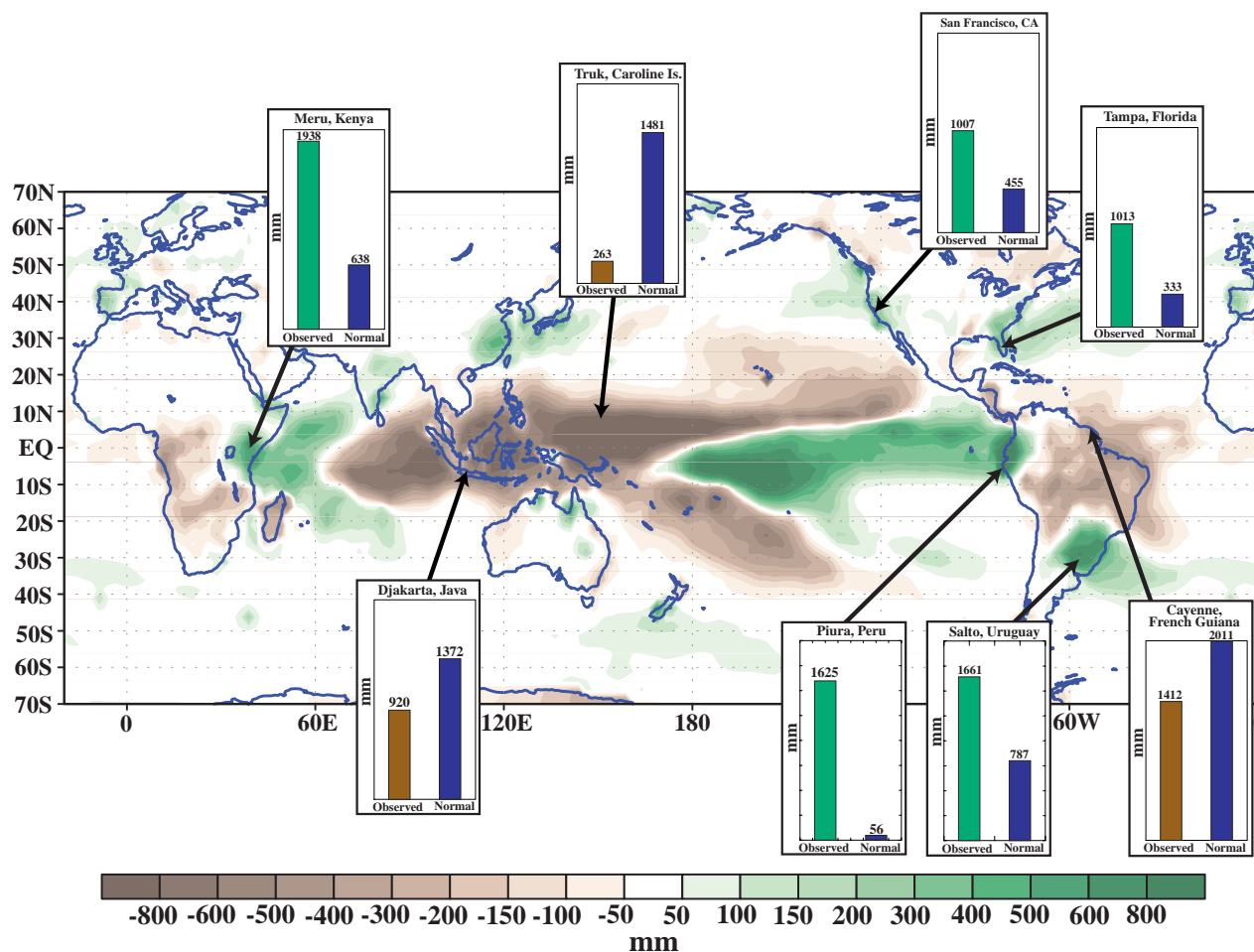
Fig. 22. Accumulated rainfall departures during November 1997–April 1998. Precipitation amounts are obtained by merging rain gauge observations and satellite-derived precipitation estimates. The satellite estimates are generated by the outgoing longwave radiation precipitation index technique (Xie and Arkin 1998), and are merged with rain gauge data via a method adapted from Xie and Arkin (1996). Anomalies are departures from the 1979–95 base period means.

South Pacific during July–September (see section 3d); 4) above-normal tropical storm and hurricane activity across the North Atlantic during August–November [see section 4a(1)]; 5) reduced rainfall across equatorial eastern Africa during the peak of the region's rainy season (October–December) and 6) above-normal rainfall across Central America and the Caribbean Sea during October–December.

b. The 1997–98 El Niño

The 1997–98 El Niño episode featured extremely warm (greater than 28°C) SSTs across the eastern half of the tropical Pacific from May 1997 to early May 1998 (Fig. 21c). These conditions reflected a complete disappearance of the mean annual cycle in SSTs in this region, along with a disappearance of the equatorial "cold tongue," which normally extends westward from

South America to the date line (Figs. 24a,c). The largest SST anomalies over the eastern half of the equatorial Pacific occurred during September–December 1997 (Fig. 21c), which coincides with the time of year in which SSTs are normally coldest and the equatorial cold tongue is best defined.

Smaller, yet substantial, anomalies were recorded during January–April 1998, which coincides with the time of year in which the climatological mean temperatures increase and the equatorial cold tongue becomes progressively less pronounced. Despite the decrease in SST anomalies across the eastern half of the Pacific during this period, the actual SSTs remained nearly constant. Therefore, the apparent "evolution" indicated by the anomaly field (which was also observed during the same period in the 1982–83 El Niño) primarily reflected the climatological mean
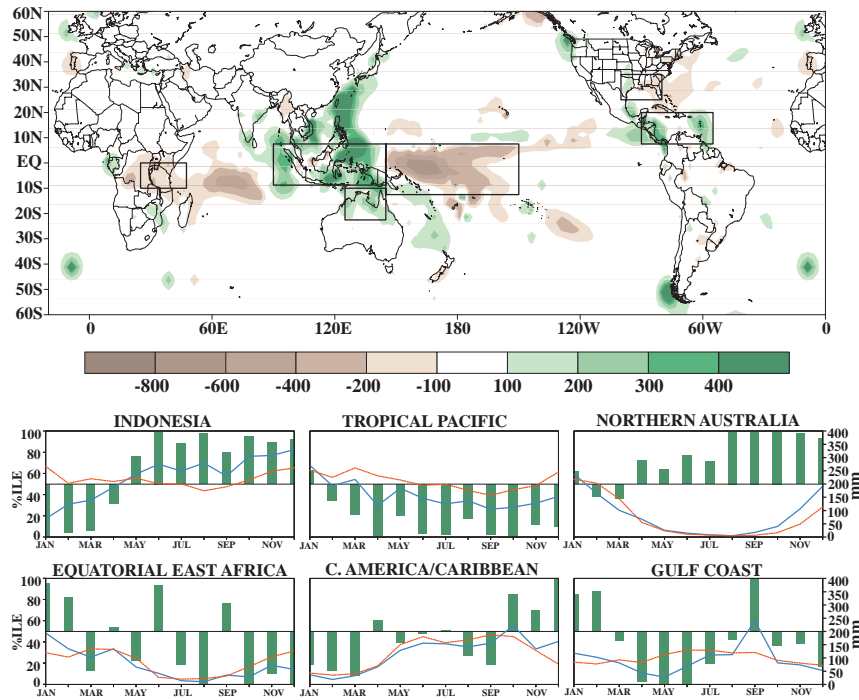
Fɪɢ. 23. October–December 1998 accumulated precipitation anomaly (top), and regional area-averaged estimates of monthly mean precipitation amounts (mm, blue lines) and precipitation percentiles (%, bars) during 1998 for the six boxed regions shown in top panel. The monthly precipitation climatology (mm, red lines) is the 1979–95 base period monthly means. Monthly percentiles are not shown if the monthly mean is less than 5 mm. The percentiles are labeled on the left-hand vertical axis and totals are labeled on the right-hand vertical axis. Precipitation estimates are obtained as described in Fig. 22.

annual cycle in SSTs and not a notable weakening of the El Niño phenomenon. Indeed, the mean and anomalous SST fields during DJF 1997/98 (Figs. 24a,b) and MAM 1998 (Figs. 24c,d) clearly indicate the continuation of extremely strong El Niño conditions throughout the period. This observation highlights the ambiguity inherent in assessing the relative strength of a warm episode and its forcing of the atmospheric circulation based solely on the SST anomalies.

During DJF 1997/98 the anomalously warm ocean waters in the central equatorial Pacific extended down to approximately 70-m depth (Fig. 25a), and overlaid anomalously cold ocean waters at approximately 150-m depth, which resulted in an enhanced thermal contrast in the thermocline in that region (see also Bell and Halpert 1998, their Fig. 25d). Farther east, the abnormally warm ocean waters (exceeding 7°C above normal at 50–100-m depth) extended to more than 150-m depth in association with increased depths of the oceanic thermocline. Overall, these conditions reflected a flat thermocline structure and a disappearance of the normal east–west temperature gradient across the entire equatorial Pacific.

During MAM 1998 shoaling of the oceanic thermocline reflected a decrease in the volume of warm water in the eastern half of the Pacific, and a confinement of the region of positive temperature anomalies to the upper ocean (Fig. 25b). These conditions were accompanied by an increased slope of the thermocline and an increased subsurface temperature gradient across the equatorial Pacific. This subsurface structure set the stage for a rapid transition to below-normal SSTs in the east-central equatorial Pacific, which subsequently began during the first week in May. At that time the low-level equatorial easterly winds returned (Fig. 21b) and were associated with enhanced upwelling bringing cooler ocean waters to the surface throughout the east-central equatorial Pacific (Figs. 21c, 25c).

Throughout the 1997–98 El Niño, atmospheric convection and rainfall were enhanced across the eastern half of the tropical Pacific (Fig. 22) and monsoonal precipitation was suppressed across Indonesia and the western tropical Pacific. The combined zonal extent of these anomalies spanned a distance more than one-half the circumference of the earth.

Within the Indonesia sector, a nearly complete lack of tropical rainfall in portions of Sumatra and Borneo from mid-July 1997 through early September 1997, followed by substantially below-normal rainfall during the next three months, contributed to extensive wildfires and an ecological disaster (Bell and Halpert 1998). These fires were started by dry-season burning, which takes place each year to clear land for planting crops.

During DJF 1997/98 and MAM 1998 the anomalous convective activity was accompanied by an almost complete absence of the normal low-level (850 hPa) equatorial easterly winds across the eastern half of the Pacific (Fig. 21b), as indicated by strong westerly wind anomalies throughout the region (Figs. 26a,b). The anomalous tropical convection was also accompanied by a collapse of the westerly winds normally observed at upper levels (200 hPa) across the eastern equatorial
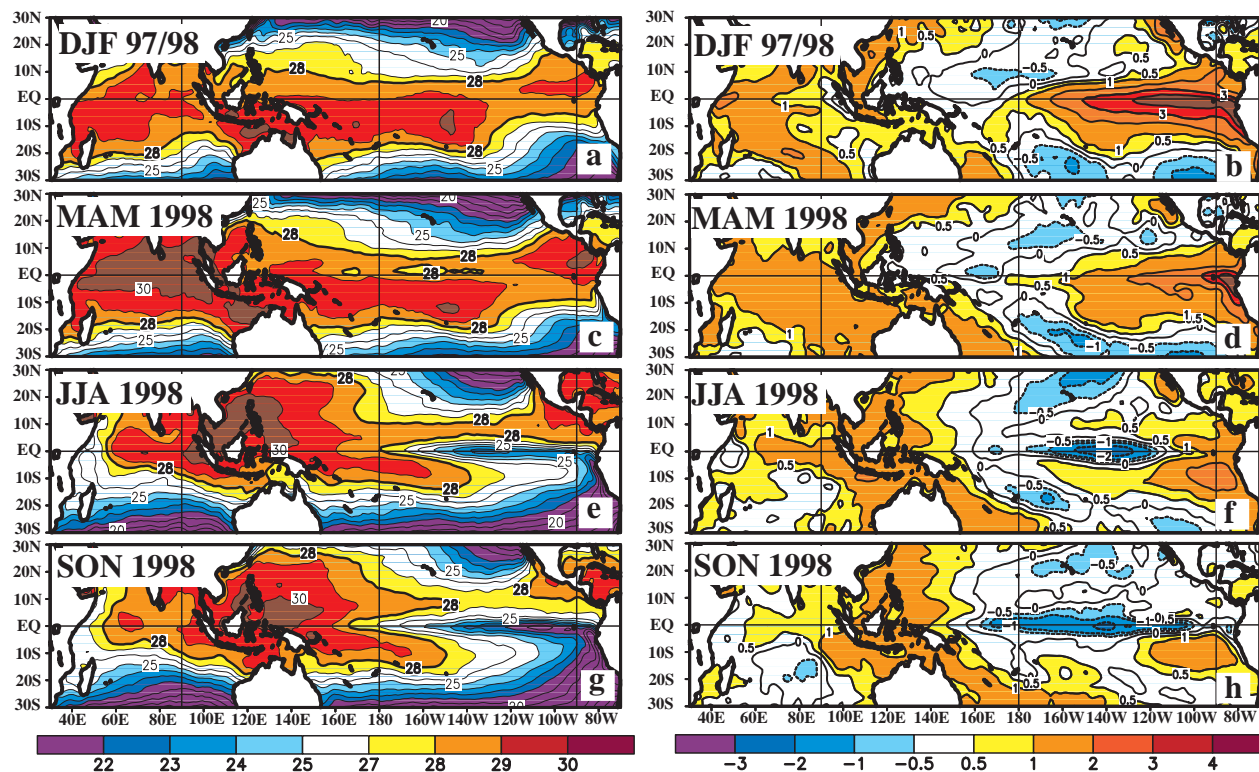
FIG. 24. Seasonal SST (left) and anomaly (right) for (a, b) DJF 1997/98, (c, d) MAM 1998, (e, f) JJA 1998 and (g, h) SON 1998. Contour interval is 1°C, with the 0.5°C anomaly contour included. Anomalies are departures from the 1950–79 adjusted OI climatology (Reynolds and Smith 1995).
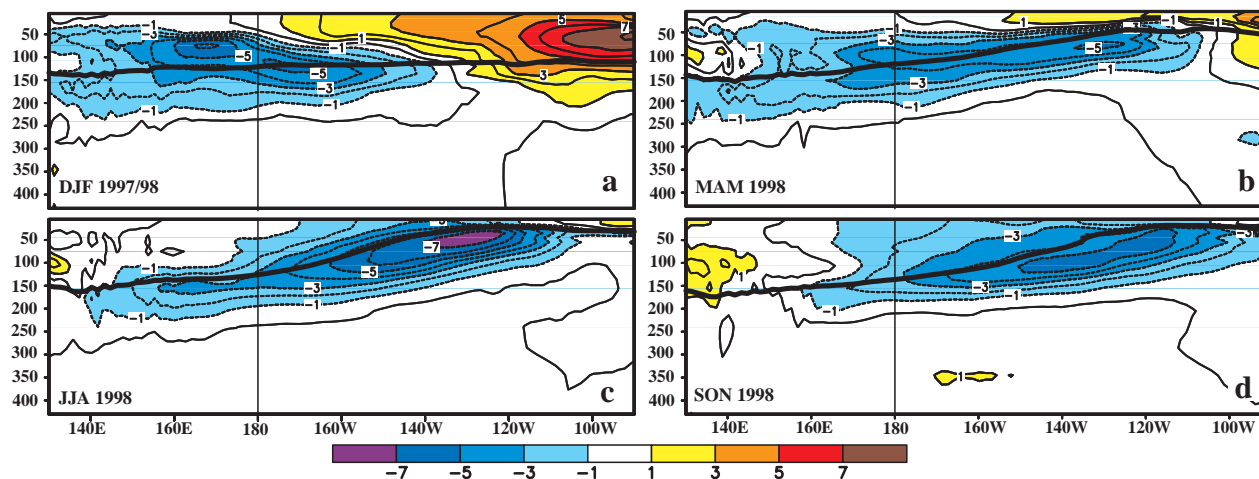

FIG. 25. Equatorial depth–longitude section of ocean temperature anomalies for (a) DJF 1997/98, (b) MAM 1998, (c) JJA 1998, and (d) SON 1998. Contour interval is 1°C. The dark line is the 20°C isotherm. Data are derived from an analysis system that assimilates oceanic observations into an oceanic GCM (Behringer et al. 1998). Anomalies are departures from the 1983–92 base period means.

Pacific, as indicated by anomalous easterly flow exceeding 10 m s^{-1} throughout the region (Figs. 27a,b). The combined patterns of vertical motion and atmospheric winds and anomalies (Figs. 28a,b) are consistent with a complete disappearance of the normal equatorial Walker circulation during the period. Similar conditions were noted during the previous two seasons by Bell and Halpert (1998, see their Fig. 28).

Other major rainfall systems were also affected by the strong El Niño conditions, including a weakening

of the South American/Central American monsoon and a shift of heavy rainfall typical of interior equatorial Africa toward eastern equatorial Africa and the western Indian Ocean. Overall, these shifts in rainfall patterns represented a more zonally uniform distribution of rainfall and deep tropospheric heating throughout the global Tropics and subtropics than is evident in the climatological mean. This shift in the heating patterns imparted a substantial forcing onto the atmospheric circulation of both hemispheres by contributing to increased heights (Fig. 21e) and temperatures across the eastern tropical Pacific and ultimately throughout the global Tropics and subtropics (see section 5, Figs. 64, 66).

As a reflection of these increased heights and temperatures, pronounced upper-level anticyclonic circulation anomalies during both DJF 1997/98 and MAM 1998 covered the subtropical eastern Pacific in both hemispheres (Figs. 27a,b). This anomaly dipole flanked the region of enhanced tropical convection and was linked directly to the strong El Niño conditions. In the Northern Hemisphere, the anticyclonic circulation anomaly also extended downstream across southern Mexico, central America, and the Caribbean during DJF 1997/98, and subsequently shifted poleward during MAM to cover northern Mexico and the southern United States.

Over the Pacific sector these circulation anomalies reflected several important changes in the flow throughout the Tropics (e.g., the disappearance of the equatorial Walker circulation), the subtropics, and the extratropics. In these latter regions, they reflected the elimination of the climatological midoceanic troughs and a pronounced extension to the eastern Pacific of both the mean subtropical ridge (compare Figs. 29a,c) and the region of strong north–south temperature contrast [see section 2b(1), Fig. 9a].

It is evident from thermal wind arguments that these basic-state changes in the subtropical height and temperature field must also be associated with a more zonally uniform westerly flow across the subtropics than is observed in the climatological mean. In the winter hemisphere, this more zonally uniform flow is associated with an eastward extension of the wintertime jet stream across the central and eastern Pacific (cf. Northern Hemisphere, Figs. 29b and 29d; Southern Hemisphere,

Figs. 31a and 31c). Thus, the anomalous subtropical ridge also establishes an inherent structural and dynamical link between ENSO-related variations in tropical convection and interannual variations in the wintertime jet stream in both hemispheres [Bell and Kousky 1995; Halpert et al. 1996, their section 4a(1)].

The January–March (JFM) period also featured negative height anomalies in the middle and upper troposphere across the extratropical eastern North Pacific and western North America in the vicinity of the climatological mean ridge (Fig. 29c), and over the south-central United States along the cyclonic shear side of the amplified subtropical jet. In contrast, positive height anomalies dominated central and eastern Canada in the vicinity of the climatological mean Hudson Bay trough. This pattern, combined with the anticyclonic circulation anomaly over the subtropical North Pacific, is often referred to as an anomalous
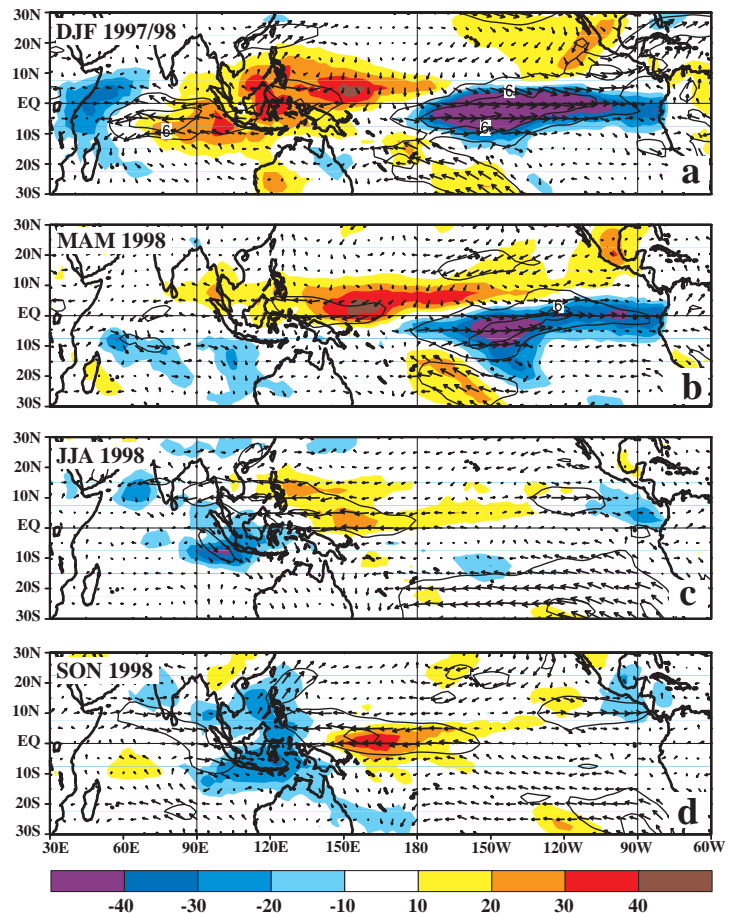

FIG. 26. OLR anomalies (shaded) and 850-hPa vector wind anomalies and isotachs for (a) DJF 1997/98, (b) MAM 1998, (c) JJA 1998, and (d) SON 1998. Contour interval for isotachs is 3 m s^{-1}. Shading interval for OLR anomalies is 10 W m^{-2}. Anomalies are departures from the 1979–95 base period monthly means.

wave train [sometimes referred to as a Pacific–North American or tropical–Northern Hemisphere teleconnection pattern (Wallace and Gutzler 1981; Barnston et al. 1991)] emanating from the subtropics and extending downstream into the extratropics (Sardeshmukh and Hoskins 1988). However, a juxtaposition of the anomaly pattern with the climatological mean height field indicates that these anomalies actually represent a *flattening* of the climatological mean wave features throughout the eastern North Pacific and North America, consistent with the eastward extension of the wintertime jet from Asia to the southwestern United States.

This interpretation shows that anomaly fields alone cannot accurately represent basic flow features such as extratropical jets (which are integrally related to

FIG. 27. OLR anomalies (shaded) and 200-hPa vector wind anomalies and isotachs for (a) DJF 1997/98, (b) MAM 1998, (c) JJA 1998, and d) SON 1998. Contour interval for isotachs is 4 m s^{-1}. Shading interval for OLR anomalies is 10 W m^{-2}. Anomalies are departures from the 1979–95 base period monthly means.

baroclinic dynamical processes) and waves. Thus, they alone cannot accurately represent the essential dynamical processes, geostrophic adjustment process, and parcel accelerations accompanying the basic-state changes in the atmospheric circulation during extremes in the ENSO cycle.

c. The jet streams across the North Pacific and North America during January–March 1998

In addition to thermal wind arguments the ENSO-related variations in the subtropical ridges represent a major dynamical forcing of the atmospheric circulation that is strongly baroclinic in nature and that dramatically impacts both the geostrophic adjustment process and the transverse ageostrophic circulation throughout the jet exit region. During JFM 1998 the extended subtropical ridge contributed to reduced diffluent flow across the central subtropical North Pacific, and to an eastward shift in the region of strong diffluence to the eastern Pacific and California (cf. Fig. 30a with Fig. 30c). These conditions were accompanied by an eastward shift in the jet exit region toward the eastern Pacific and western United States, and by a concurrent shift in the thermally indirect transverse ageostrophic circulation and strong deceleration that help to define the exit region (cf. Fig. 30d with Fig. 30b). Bell and Halpert (1998) noted similar changes in these features within the jet exit region during JJA 1997 in association with the extended Southern Hemisphere wintertime jet stream (Fig. 31c, also see their Figs. 29 and 30). In both cases these basic-state changes in the subtropical ridges, the wintertime jet stream, the structural characteristics of the jet exit region, and the entire transverse ageostrophic circulation in the jet exit region reflected a mean flow configuration that is internally consistent with jetstream dynamics (Keyser and Shapiro 1986) and that is also thermodynamically consistent with the distribution of tropical heating.

During JFM 1998 the extended East Asian jet stream was accompanied by a strengthening of the subtropical jet across the southern tier of the United States (Fig. 29d). Moreover, this subtropical jet reflected a deep baroclinic structure and was no longer confined solely to the upper troposphere.
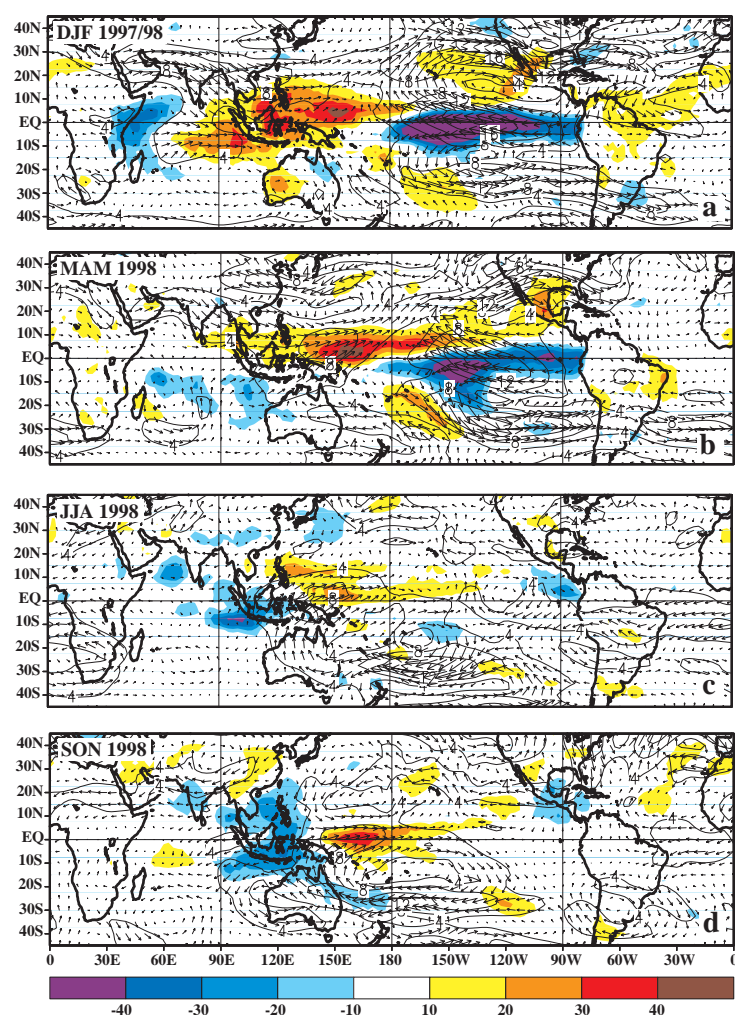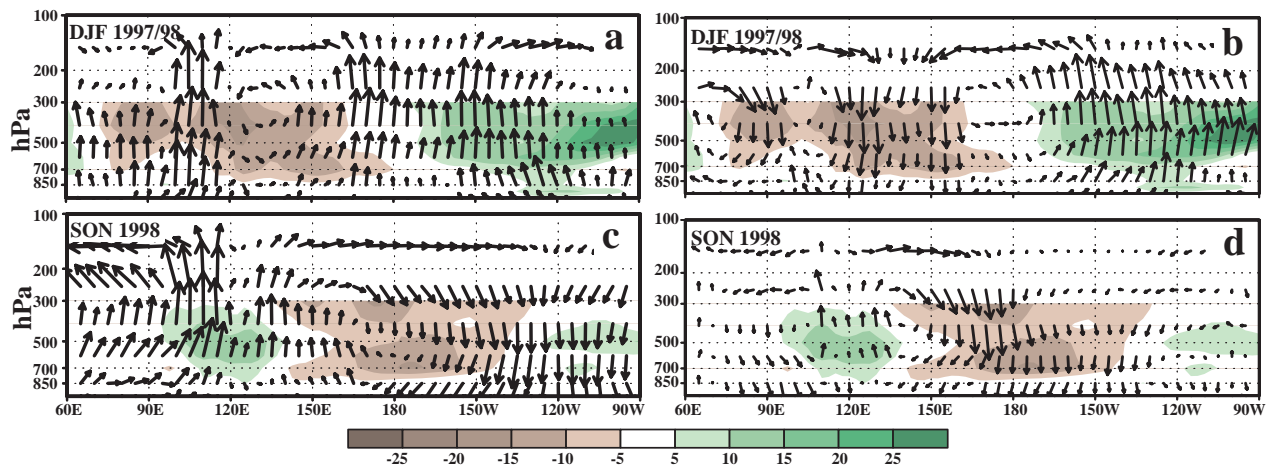
FIG. 28. Mean (left) and anomalous (right) pressure–longitude sections of the equatorial Walker circulation for (a), (b) DJF 1997/98 and (c), (d) SON 1998. Vertical component of vectors is the scaled pressure vertical velocity, and horizontal component is the zonal component of the divergent wind. The pressure vertical velocity was subjectively scaled to give a sense of the relative vertical motion in the equatorial plane. Shading in all panels shows relative humidity anomalies (%). Note that the relative humidity in the NCEP–NCAR reanalysis extends upward to only the 300-hPa level.

JFM Climatology

JFM 1998
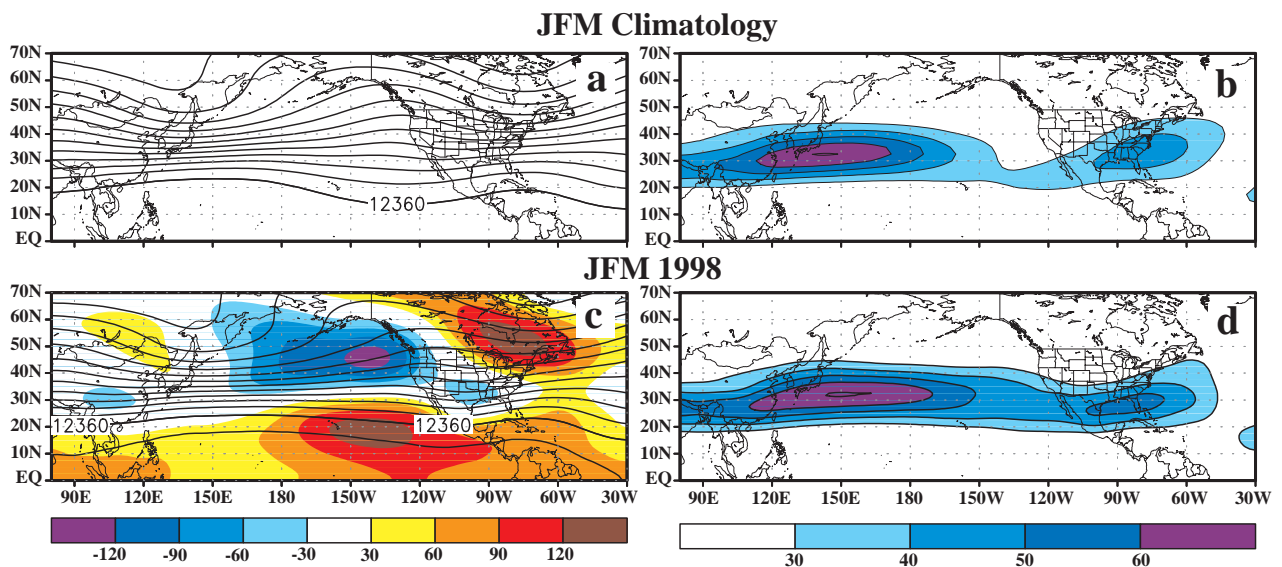
FIG. 29. January–March patterns at 200-hPa showing conditions at 200-hPa associated with the Northern Hemisphere wintertime East Asian jet stream for (top) the climatological mean and (bottom) the 1998 mean. Panels (a), (c) show heights (contours, interval is 120 m) and panels (b), (d) show zonal wind speed (m s^{-1}). Panel (c) also shows height anomalies (shaded). The climatology and height anomalies are computed from the 1979–95 base period means.

Accompanying this flow structure was a significantly reduced amplitude of the circulation features that typically characterize the entrance regions of both the subtropical jet and North Atlantic jet. For example, across the central United States in the left jet entrance region, the more prominent of these changes included substantially reduced geostrophic confluence (cf. Figs. 30a and 30c) and a reduced strength of both the thermally direct transverse ageostrophic circulation and Lagrangian kinetic energy tendencies (cf. Figs. 30b and 30d). Consistent with these conditions, the ageostrophic wind vectors along the axis of the subtropical jet entrance region were aligned nearly parallel to the isotachs and height contours. This orientation indicates that the primary geostrophic adjustment was linked to flow curvature associated with the large-scale trough over Mexico at this time (Fig. 30c), and no longer linked to alongstream speed variations
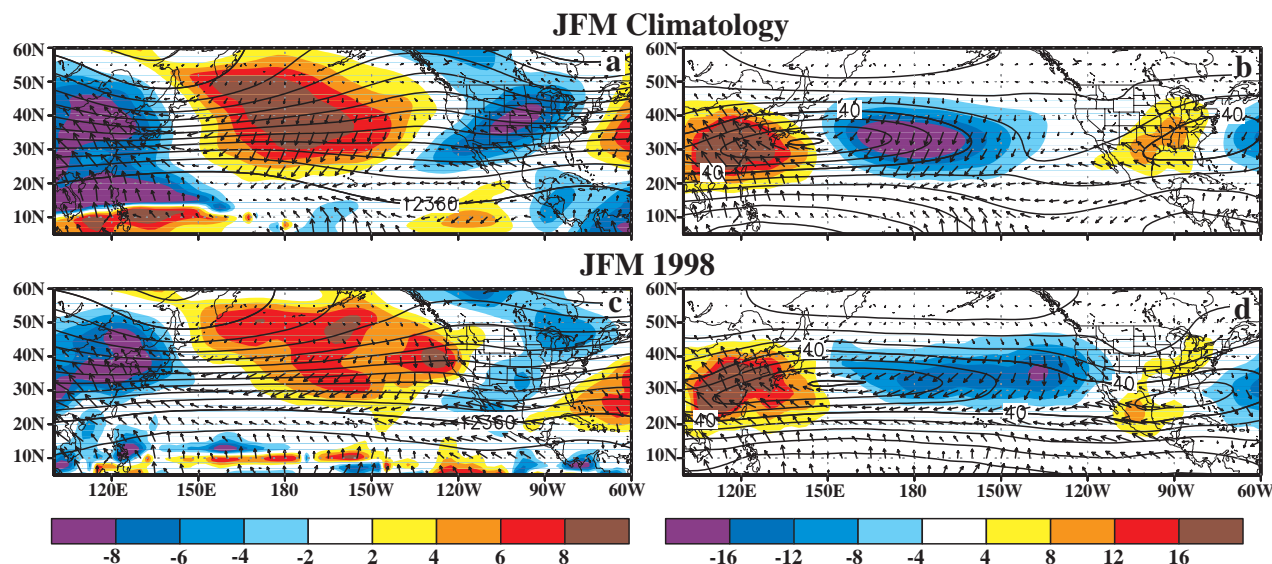
JFM Climatology

FIG. 30. January–March patterns showing conditions at 200-hPa associated with the Northern Hemisphere wintertime East Asian jet stream for (top) the climatological mean and (bottom) the 1998 mean. Shading in panels (a), (c) show geostrophic diffluence/ confluence (interval is 2×10^{-6} s^{-1}), and in panels (b), (d) show Lagrangian kinetic energy tendency (interval is 4×10^{-3} m^2 s^{-3}). The horizontal ageostrophic wind vector is also shown in all panels. For reference, the height field (contours, interval is 120 m) is overlaid in panels (a), (c) and the zonal wind field (contours, interval is 10 m s^{-1}) is overlaid in panels (b), (d). Diffluence and confluence are indicated by positive and negative values, respectively, and are calculated in Cartesian coordinates based on the transformation equations presented by Bell and Keyser (1993). Climatology is the 1979–95 base period means.

and dynamical processes typical of a jet entrance region. This interpretation is consistent with the theoretical analysis of Keyser and Shapiro (1986) showing the relative orientation of the ageostrophic wind vector to the isotachs and height contours in idealized jet stream and gradient wave configurations.

The combined structural changes in the East Asian jet and in the subtropical jet impacted the regions of cyclogenesis and subsequent storm movement across the North Pacific and the United States, as well as the large-scale patterns of vertical motion, precipitation, and temperature across North America. In particular, they contributed to 1) a notable absence of blocking activity at high latitudes of the central North Pacific; 2) enhanced storm activity and precipitation across California and the southern tier of the United States; 3) extreme warmth over most of North America, with record or near-record temperatures across central Canada and large portions of the central and northeastern United States; and 4) a continuation of severe drought in Mexico [see section 4a(3)].

d. Evolution of the 1998 La Niña

The JJA and SON 1998 seasons featured the evolution to cold episode conditions in the tropical Pacific, as indicated by the establishment of a well-defined

tongue of abnormally cold SSTs extending from the west coast of South America toward the date line (Figs. 24e–h). During this period a continuation of oceanic upwelling contributed to a strongly sloped oceanic thermocline, with much shallower than normal thermocline depths evident across nearly the entire eastern half of the equatorial Pacific (Figs. 25c,d). Accompanying this structure, the depth of the 20°C isotherm shoaled to near 30 m, in stark contrast to the 120–150-m depths observed during the peak of the 1997–98 warm episode.

The evolution to cold episode conditions was accompanied by a dramatic adjustment of the global monsoon systems, as evidenced by both the OLR and atmospheric wind anomaly patterns (Figs. 26c,d, 27c,d). In particular, enhanced convective activity developed across portions of Indonesia during JJA, while suppressed convection was evident across the western and central equatorial Pacific. By SON, this rainfall anomaly pattern had become well defined (Figs. 23, 26d), indicating a confinement of deep tropical convection to the Indonesian sector and a strengthening of the Australasian monsoon system. Also observed during SON was increased rainfall across Central America and southern Mexico in association with a strengthening of that region's monsoon system. These precipi-

S24

tation patterns are in marked contrast to those observed during the 1997–98 warm episode, which featured weakened monsoon systems across Australasia and Central America in association with the eastward extension of tropical convection across the eastern Pacific.

Accompanying the transition to cold episode conditions, the low-level easterly winds during JJA (Fig. 26c) were stronger than normal across the western equatorial Pacific, and generally near normal east of the date line. These conditions contrasted with those observed during the 1997–98 warm episode, when equatorial zonal winds were weak or even westerly across the Pacific basin. By SON enhanced easterly winds were observed across the western and central equatorial Pacific (Fig. 26d), while near-average winds remained over the eastern equatorial Pacific.

At upper levels these periods featured a return to near-normal winds across the eastern equatorial Pacific (Figs. 27c,d) and a continuation of westerly wind anomalies over the western equatorial Pacific. By SON these westerly anomalies had extended to well east of the date line and were accompanied by the development of cyclonic circulation anomalies in the subtropics of both hemispheres flanking the region of suppressed tropical convection. Collectively, these conditions reflected several prominent changes in the atmospheric circulation in the Tropics, subtropics, and extratropics which contrasted to those observed during the 1997–98 warm episode. First, they reflected a strengthening of the equatorial Walker circulation (Figs. 28b,d), compared to a nearly absent Walker circulation earlier in the year (Figs. 28a,b). Second, they reflected a pronounced westward retraction of the subtropical ridges in both hemispheres, along with a strengthening of the mid-Pacific troughs (Fig. 31b). Third, they reflected a weaker and substantial westward retraction of the wintertime jetstream over the South Pacific (Fig. 31b), which is in dramatic contrast to the well-defined jet stream that extended across the entire South Pacific during JJA 1997 [Fig. 31c; see also Bell and Halpert (1998), their Figs. 29 and 30].

4. Regional climate highlights

a. North America
1) THE 1998 NORTH ATLANTIC AND EASTERN NORTH PACIFIC HURRICANE SEASON
(i) Overview

The North Atlantic hurricane season runs from June through November and exhibits a peak in activ-
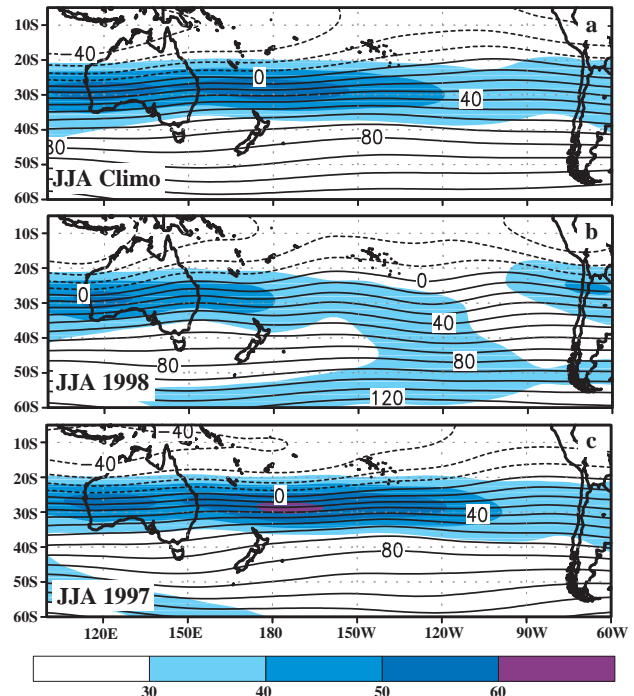

FIG. 31. June–August 200-hPa stream function (contours, interval is 10×10^6 m^2 s^{-1}) and zonal wind speed (shaded, m s^{-1}) associated with the wintertime South Pacific jet stream for (a) the climatological mean, (b) the 1998 cold episode conditions, and (c) the 1997 warm episode conditions. Climatology is the 1979–95 base period means.

ity from August–October, primarily in response to systems developing from African easterly wave disturbances. The 1998 hurricane season was extremely active and one of the deadliest in history with 11 629 lives claimed. The season also featured the strongest October hurricane (Mitch) on record, which claimed more than 11 000 lives in Central America. The last time that a single Atlantic hurricane caused so many deaths was 1780.

Overall, 9–10 named tropical storms are observed over the North Atlantic in an average season, with 5–6 becoming hurricanes and 2 reaching intense hurricane status [measured by a category 3, 4, or 5 on the Saffir–Simpson scale (Simpson 1974)]. The 1998 hurricane season featured 14 named storms (Fig. 32), with 9 of these systems becoming hurricanes and 3 reaching intense hurricane status. These conditions are in marked contrast to the suppressed 1997 hurricane season, which featured seven named storms (Fig. 32), with three of these systems becoming hurricanes and only one reaching intense hurricane status.

Most of the storms during the 1998 season developed during the 35-day period of 19 August–23 Sep-
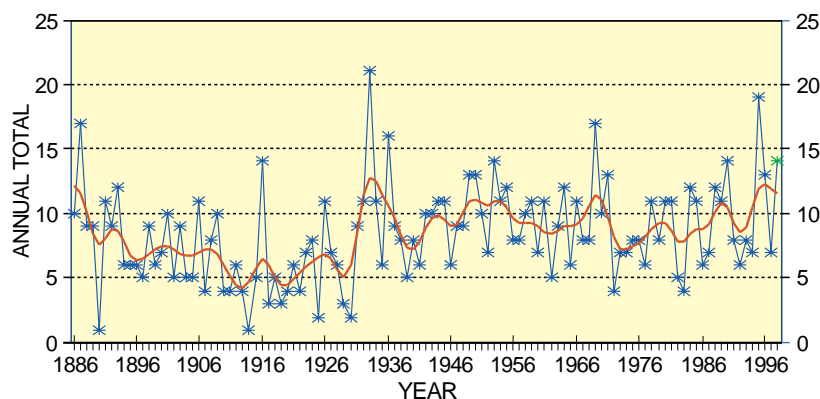
FIG. 32. Number of hurricanes and tropical storms for the North Atlantic basin: 1998 is shown in green. (Source: National Climatic Data Center.)

tember when 10 tropical storms formed (7 of which became hurricanes). During the peak of activity on 25 September, there were four Atlantic hurricanes in progress at the same time. This is the first time since 1893 that such an event has occurred. In contrast, August–September 1997 featured the formation of only one hurricane (Erica) over the entire North Atlantic basin, which is a record low for the period since the beginning of the aircraft reconnaissance era in 1944.

Other aspects of the 1998 Atlantic hurricane season included an exceptionally late start to the tropical storm activity, with the first tropical storm (Alex) developing on 27 July. The season also featured a continuation of activity well into November, with the final system of the season (Nicole) becoming a tropical storm on 24 November and a hurricane on 29 November.

Over the eastern North Pacific the 1998 hurricane season featured slightly below-normal activity, with 13 named storms (normal is 16), 9 of which became hurricanes (normal is 9). The season also featured a reduced area of tropical cyclone activity compared to normal, particularly along the west coast of North America where only one system (Hurricane Isis) made landfall in Mexico. Normally, three or four tropical storms impact this region during the eastern Pacific hurricane season.

(ii) June–July

Tropical storm and hurricane activity over both the North Atlantic and eastern North Pacific Ocean basins is strongly affected by the vertical wind shear between the upper (200 hPa) and lower (850 hPa) levels of the atmosphere. Strong vertical shear inhibits tropical cyclogenesis while weak vertical shear (less than ap-

proximately 8 m s^{-1}) favors tropical cyclogenesis and possible hurricane development.

During June–July 1998, the lack of tropical cyclone activity over the North Atlantic and Caribbean Sea was linked to very strong vertical wind shear throughout the region (Fig. 33a), with larger-than-normal values dominating the region off the southeastern coast of the United States, the central subtropical Atlantic, and central Caribbean Sea (Fig. 33c). The high wind shear off the eastern seaboard of the United States was linked to enhanced upper-level westerly winds along the eastern flank of a very strong subtropical ridge that dominated the southern tier of the United States from April through mid-July [see section 4a(2), Fig. 40b]. This amplified ridge was directly linked to intense convection over the eastern equatorial Pacific in association with strong El Niño conditions (see section 3). Farther east, the high wind shear over the central subtropical Atlantic was linked to enhanced upper-level southwesterly flow in association with a stronger-than-normal tropical upper-tropospheric trough (TUTT) situated immediately downstream of the subtropical ridge. These conditions contrasted with the low shear observed across the western Atlantic during June–July 1997 (Figs. 33b,d) in association with a reduced strength of the TUTT. Three tropical depressions formed in this region during that period.

Farther south during June–July 1998 lower-than-average shear values in the vicinity of the subtropical ridge axis covered Mexico, the southern Gulf of Mexico, and the northern Caribbean. Nonetheless, the actual shear values in these regions, which far exceeded 8 m s^{-1}, combined with strong upper-level convergence and sinking motion (not shown), inhibited tropical cyclone formation during the period.

(iii) August–November

The inactivity during June–July 1998 was followed by an extremely active August and September, with 10 tropical storms (7 of which became hurricanes) forming during the period. This transition to well-above-normal activity during the climatologically active part of the season contrasts to the previous year, when only one Atlantic basin hurricane formed during August–September 1997.
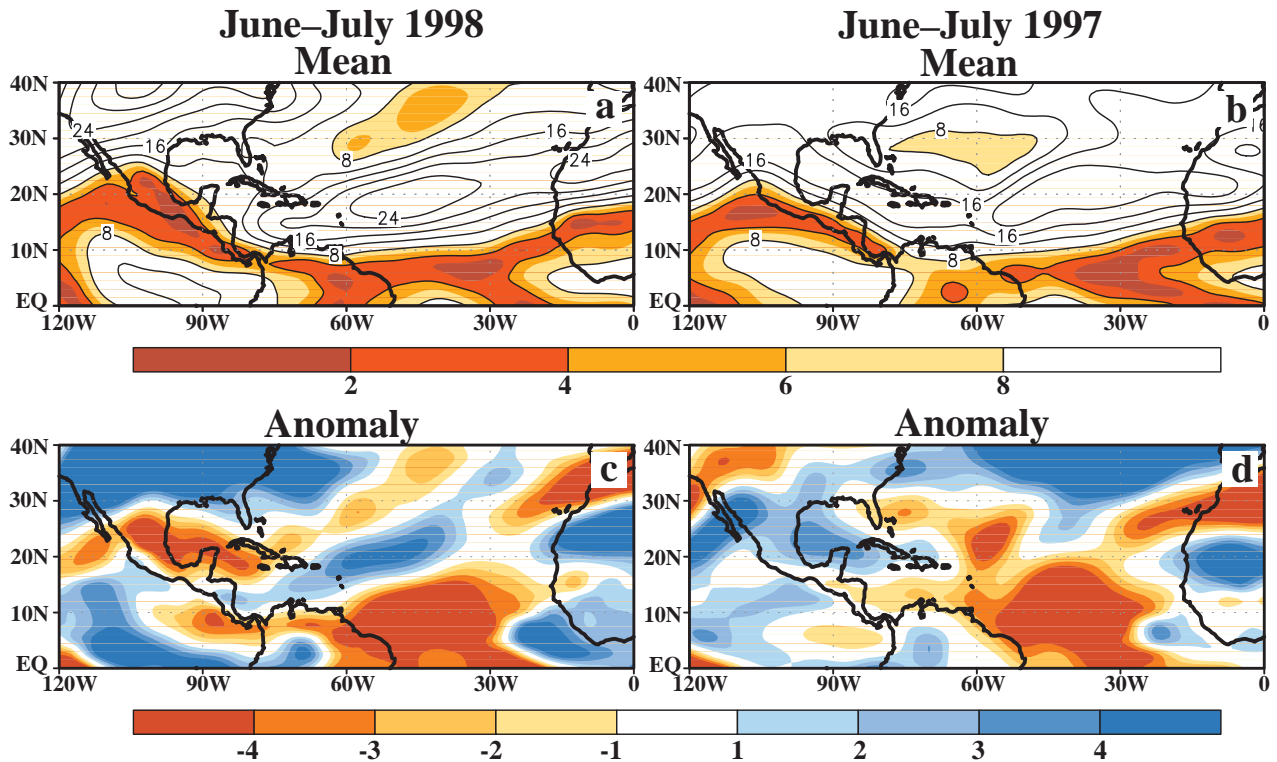
FIG. 33. Vertical wind shear and departure from normal during (a), (c) June–July 1998 and (b), (d) June–July 1997. Wind shear is calculated as the difference in wind speeds between 200- and 850-hPa (contour interval is 4 m s⁻¹). Shaded areas in (a), (b) indicate where the vertical wind shear is less than 8 m s⁻¹ and are considered favorable for tropical cyclone formation.

Climatologically, tropical storms and hurricanes often develop from African easterly waves during August–September. These wave disturbances move across western Africa between 10°–15°N and then propagate westward across the subtropical North Atlantic. However, the potential for tropical storm development within the easterly waves is heavily influenced by two factors: the vertical wind shear (Gray 1984) and the structure/location of the low-level African easterly jet within which the disturbances move and evolve (Reed et al. 1977). The coherent interannual variations in these two fields is discussed by Bell and Halpert (1998) and Bell and Chelliah (1999).

Climatologically, the region of low vertical wind shear during August–September extends from Africa to northwestern South America (Fig. 34a), with the lowest shear values centered near 10°S over the central North Atlantic. High vertical wind shear typically dominates much of the subtropical North Atlantic and the Caribbean sector, making these regions unfavorable for tropical cyclogenesis. In contrast, active hurricane years such as 1998 (Fig. 34c) feature low vertical wind shear across the entire North Atlantic between 10°–15°N and throughout the Caribbean sector (see also Landsea et al. 1998; Bell and Halpert 1998; Bell and Chelliah 1999). A vertical profile of the atmospheric winds over the Caribbean Sea region during August and September 1998 (blue curves in Figs. 35a,b) shows that the reduced vertical wind shear resulted from the development of easterly winds at upper levels and from anomalous westerly winds at lower levels. Similarly, the extremely active August–October 1995 season was associated with very low vertical wind shear across the Caribbean throughout the 3-month period (green curves).

In contrast, both the inactive August–October 1997 (Fig. 34e) and October 1998 periods featured an expanded region of high wind shear across the western North Atlantic and Caribbean, and a confinement of low shear values to the central and eastern Atlantic. A vertical profile of the atmospheric winds over the Caribbean Sea region during August–October 1997 and October 1998 (Figs. 35a–c, and 35c, respectively) indicates that the enhanced vertical shear resulted primarily from strong upper-level westerly winds across the region, which is a reversal in wind direction at these levels from that observed during the active periods.
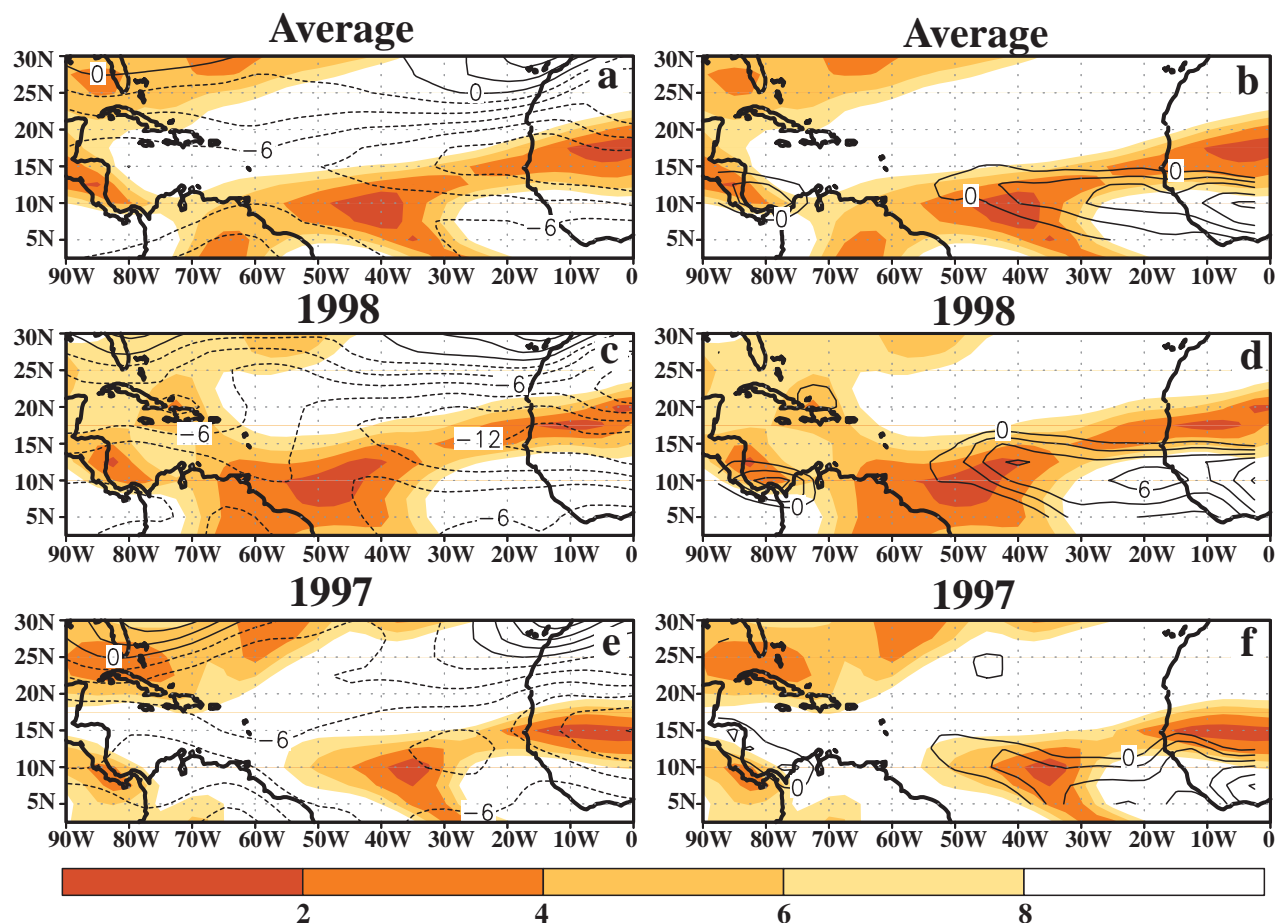
FIG. 34. August–September mean 200-850-hPa vertical wind shear (shaded, m s^{-1}), overlaid with (a), (c), (e) 600-hPa zonal wind (contours, interval is 2 m s^{-1}) and (b), (d), (f) 600-hPa cyclonic relative vorticity (contours, interval is 2×10^{-6} s^{-1}). Panels (a), (b) show 1979–95 climatological mean conditions. Panels (c), (d) show conditions during the active 1998 period and panels (e), (f) show conditions during the inactive 1997 period.

There are also considerable changes in the location and structure of the African easterly jet between active and inactive hurricane years (Bell and Halpert 1998; Bell and Chelliah 1999). This easterly jet normally extends from western Africa to the central subtropical North Atlantic (Fig. 34a), with the jet core located near 15°N. The jet reaches peak strength between the 600–700-hPa levels and provides the "steering flow" for the easterly waves. It is also an important initial energy source for the easterly waves, which propagate through the cyclonic shear zone (Fig. 34b) along the southern flank of the jet (Reed et al. 1977). This cyclonic-shear zone is normally well defined over the eastern tropical North Atlantic and western Africa between 8°–15°N and overlaps the area of low vertical wind shear (Fig. 34b). This overlap is normally most extensive in September during the climatological peak in the Atlantic tropical cyclone activity.

During the active August–September 1998 period (Fig. 34c) the African easterly jet was well defined and shifted approximately 2.5° north of its normal position. It was also stronger than normal across virtually the entire subtropical North Atlantic, with an increased meridional gradient in zonal wind in the region immediately south of the jet core. These conditions resulted in large areas of cyclonic relative vorticity covering the entire central and eastern North Atlantic between 10° and 15°N (Fig. 34d). Also, there was a substantially increased overlap of the regions of large cyclonic relative vorticity and low vertical wind shear between 10° and 15°N across the central and eastern North Atlantic, particularly when compared to that associated with the climatological mean and the inactive 1997 period (Fig. 34f). This favorable location and horizontal structure of the African easterly jet during August–September 1998, combined with its
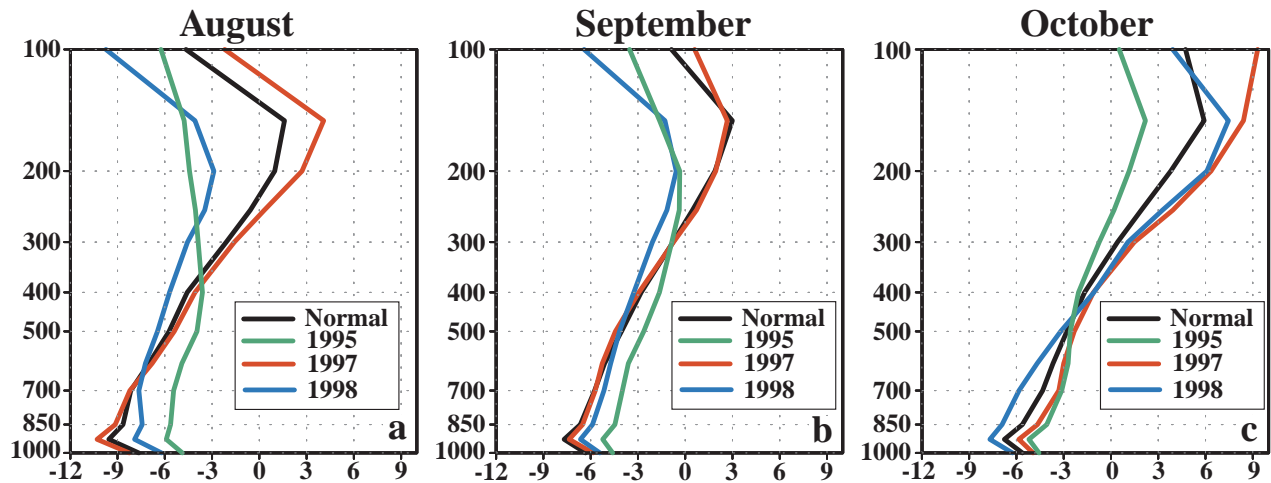
FIG. 35. Vertical profile of atmospheric zonal winds (m s⁻¹) averaged over the Caribbean Sea sector during Aug, Sept, and Oct. Negative values indicate easterly winds and positive values indicate westerly winds. The black curve indicates the 1979–95 normal conditions, the green curve indicates 1998 conditions, the red curve indicates 1997 conditions, and the blue curve indicates 1995 conditions.

proximity to the extended region of low vertical wind shear, contributed to recurring tropical cyclogenesis and intense hurricane development from easterly waves throughout the period.

In contrast, the African easterly jet during the inactive August–September 1997 period was centered near 12.5°N over the eastern Atlantic (Fig. 34e), which is 2°–3° south of normal and approximately 5° south of its mean 1998 position. The jet core was also weaker and more diffuse than normal, with a weaker meridional gradient in wind speed evident along its cyclonic-shear side. As a result, the primary region of cyclonic vorticity was displaced to south of 10°N (Fig. 34f), which is generally considered too far south to favor efficient tropical cyclogenesis. This area of weak cyclonic vorticity was also displaced well south of the region of low vertical wind shear, with comparatively little overlap of the two features present. This combination of both an unfavorable structure and location of the African easterly jet, along with high vertical wind shear across the western Atlantic and Caribbean, resulted in suppressed development of the African easterly waves and a dearth of tropical cyclogenesis during the period.

2) APRIL–JUNE 1998 U.S. DROUGHT IN THE SOUTH; FLOODING IN THE MIDWEST AND NORTHEAST
(i) Temperature and rainfall

Extreme dryness during April–June 1998 covered much of the south-central and southeastern United States (Fig. 36), with record low statewide rainfall to-

tals dating back to 1895 observed in New Mexico, Texas, Louisiana, and Florida. Many locations across Florida and Louisiana received under 150 mm of rain during the period, which is less than half the long-term average. Broad sections of Texas and New Mexico received 25–100 mm of rain, which is less than 25% of the long-term average. This dryness was a dramatic change from the surplus rainfall observed in much of these areas from late 1997 through March 1998.

The dryness was accompanied during May–June by record heat in Texas, Louisiana, Arkansas, and Florida (Fig. 37), with temperatures averaging 2°–4°C above normal across most of the region. Temperatures across much of Texas and parts of Florida, Georgia, and Alabama reached or exceeded 35°C on more than 50% of the days during May–June (Fig. 38). These conditions resulted in widespread drought from New Mexico to Florida, with the most severe drought occurring in Texas and Florida.

In Florida, one consequence of these extreme conditions was the development of widespread wildfires during June–early July 1998 in all 67 counties. By 5 July, 483 000 acres and 356 structures had been consumed by fires, resulting in an estimated $276 million in damages according to the Florida State Emergency Operations Center (1998, personal communication). Over 100 000 people had been ordered to leave their dwellings during this period, including the entire population of Flagler County. Increased rainfall and humidity over the 4 July weekend allowed firefighters to make progress toward controlling sev-
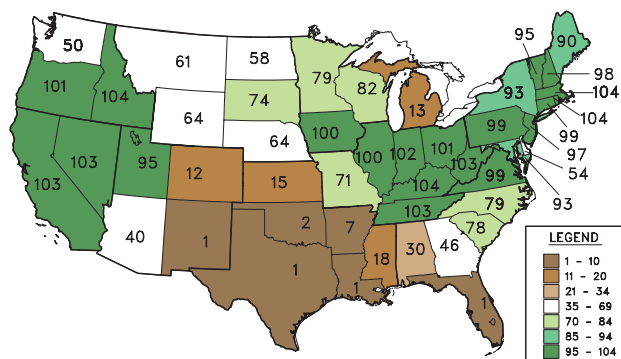
FIG. 36. Statewide rankings of April–June 1998 precipitation totals based on the 1895–1998 period. A ranking of 1 (104) indicates that April–June 1998 was the driest (wettest) such period in the historical record.
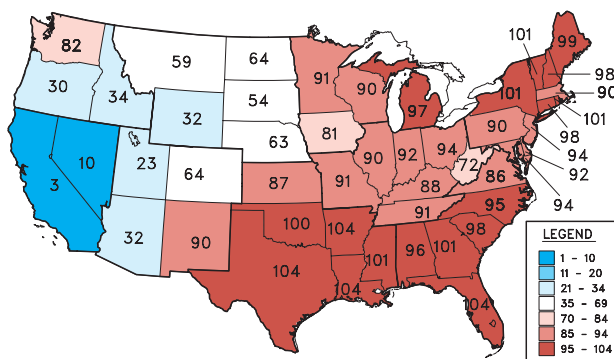

FIG. 37. Statewide rankings of May–June 1998 mean temperature based on the 1895–1998 period. A ranking of 1 (104) indicates that May–June 1998 was the coolest (warmest) such period in the historical record.

eral large wildfires. Additional control of the fires, particularly those in Flagler County, came on 6–7 July as widespread rainfall covered central Florida. Wildfires also occurred in Texas during May–June and burned an estimated 143 000 acres, according to the Texas Emergency Response Division (1998, personal communication).

In contrast, above-normal rainfall covered much of the western, midwestern, and northeastern portions of the country during April–June (Fig. 36), with totals exceeding 400 mm in most of the primary cities in the Ohio Valley, Tennessee Valley, central Appalachians, and lower Northeast (Fig. 39). Record high statewide rainfall totals (dating back to 1895) were observed in Rhode Island and Massachusetts, while the third and fourth highest totals in the record were observed in Tennessee and Iowa, respectively. The rains during May and June were often associated with strong thunderstorms, including tornadoes, hail, damaging winds, and flash floods. According to data from the National Severe Storm Prediction Center (1998, personal communication) 372 tornadoes were recorded during June over the nation as a whole, which is nearly 200 more than average. The rainfall was particularly intense in some states during June, which was the second wettest June in 104 yr in Massachusetts, New Hampshire, Rhode Island, and Vermont, and the third wettest in Iowa and Maine.

(ii) Atmospheric circulation

The anomalous temperature and rainfall patterns observed across North America during April–June were essentially manifestations of an exceptionally persistent, large-scale atmospheric circulation pattern (Fig. 40). Primary features of this pattern included 1)

a pronounced amplification of the subtropical ridge across the eastern North Pacific, Mexico, and the south-central United States (Fig. 40a); 2) increased jet stream winds [1.5–2 times normal] (Fig. 40b) and increased storminess across the central and northern United States; 3) an amplified upper-level trough over the western United States, which acted as a continuous source region for the storms; and 4) above-normal heights and weaker-than-normal jet stream winds across Canada, which helped to concentrate the jet stream and storminess over the central United States.

All of these features were linked to the 1997–98 El Niño and many were prominent aspects of the atmospheric circulation since January. In fact, one difference in the atmospheric circulation features between January–March (see Figs. 29c,d) and April–May was simply an overall poleward shift of the anomaly centers in the Northern Hemisphere in association with the normal progression of the seasons. Another difference was the establishment of the amplified ridge di-
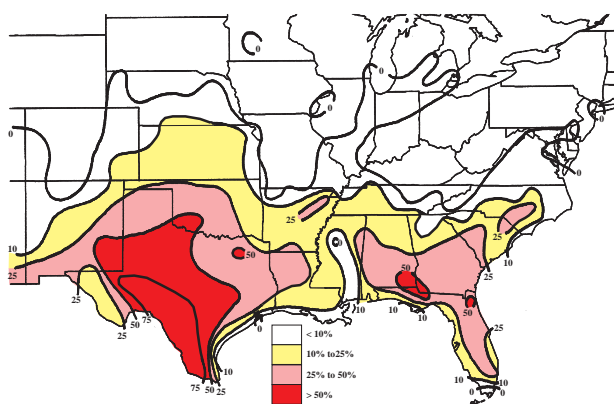

FIG. 38. Percentage of days during May–June 1998 in which the daily maximum temperature reached or exceeded 35°C (95°F).
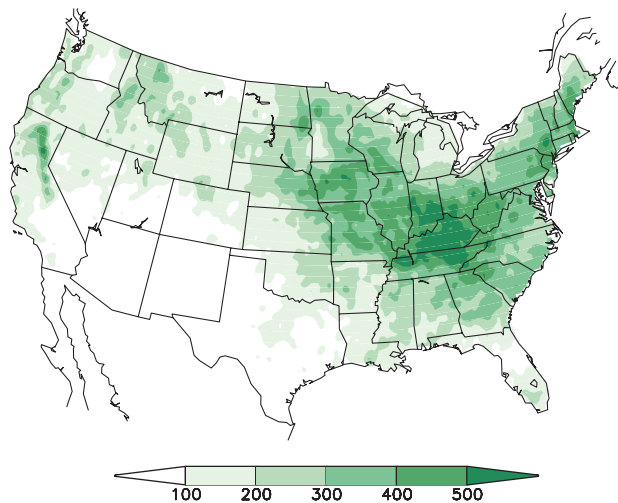
FIG. 39. April–June 1998 rainfall totals (mm) over the United States.

FIG. 40. April–June 1998 upper-level (200 hPa) (a) heights (m, contours) and departures from normal (shading), and (b) wind speed (m s⁻¹, contours) and departures from normal (shading). Departures are from the 1979–95 base period means.

rectly over Mexico and the southern United States, which resulted from a collocation of El Niño–related positive height anomalies with the development of the climatological mean ridge over Mexico. Accompanying these conditions was a corresponding northward movement in the regions of hot and dry conditions from Central America and southern Mexico [see section 4a(3)] to northern Mexico and the Gulf Coast states, and in the regions of strong storminess, increased rainfall, and severe weather from the southern states to the central and northern sections of the United States.

The links between the above circulation features and the 1997/98 El Niño are further highlighted in Figs. 40–42. The enhanced subtropical ridge during April–June 1998 was associated with a large-scale pattern of above-normal heights that spanned the entire Tropics and subtropics of both hemispheres (Fig. 40a). These areas of above-normal heights are consistent with the strong convection that prevailed across the eastern half of the tropical Pacific for most of the period (Figs. 27a,b). Moreover, a remarkably coherent and symmetric pattern of height, temperature, and wind anomalies was evident over the eastern Pacific in the subtropics and extratropics of both hemispheres during the period (Fig. 41). Thus, the amplified subtropical ridge reflected only one of many components of the large-scale atmospheric circulation, which remained linked to the patterns of anomalous tropical convection during the period. During June, the continuation of an enhanced subtropical ridge across Mexico and the southern United States was also consistent with a continuation of enhanced tropical rain-
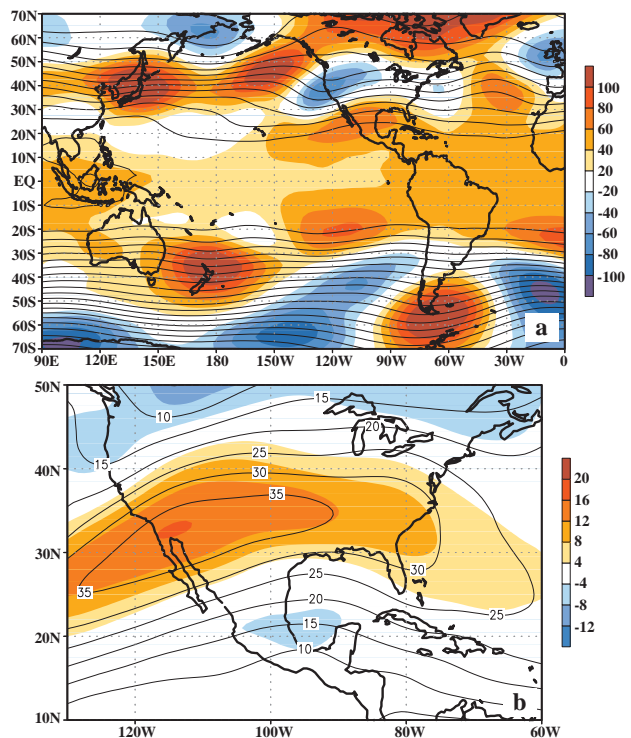
fall (Fig. 42a) and abnormally warm sea surface temperatures (Fig. 42b) over the extreme eastern tropical and subtropical North Pacific. Thus, while SSTs had cooled significantly in the central equatorial Pacific by June, residual warm waters in the extreme eastern Pacific helped to maintain the amplified subtropical ridge over the southern United States and Mexico.

3) THE 1997/98 MEXICAN DROUGHT

In Mexico the July 1997 through June 1998 period was the driest in the historical record dating back to 1945 (Fig. 43), with below-normal rainfall observed in every month except November 1997. During March–June 1998 this dryness, in combination with prolonged periods of extreme heat, led to an intensification of drought conditions which culminated in widespread forest fires. The onset, intensity, and duration of the Mexican drought were also linked to the strong 1997–98 El Niño.

The onset of the drier-than-normal conditions occurred during JJA 1997 (Fig. 44a), in association with the establishment of strong El Niño conditions. During this period rainfall totals averaged 20%–60% of normal over much of the country, with the largest defi-
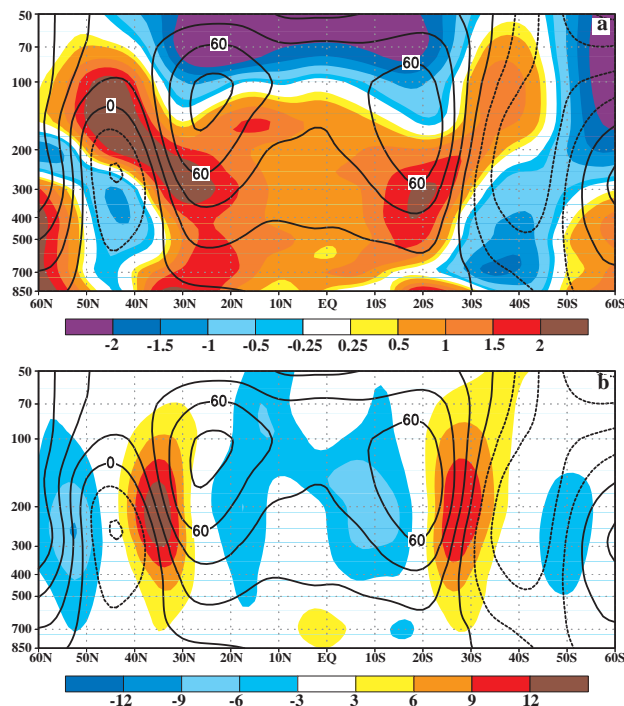
FIG. 41. April–June 1998 height–latitude section at 115°W of (a) height anomalies (m, contours) and temperature anomalies (°C, shading), and (b) height anomalies and zonal wind speed anomalies (m s^{-1}, shading). Anomalies are departures from the 1979–95 base period means.

FIG. 42. June 1998 upper-level (200 hPa) (a) height anomalies (m, contours) and OLR anomalies (W m^{-2}, shaded), and (b) SST anomalies (°C, shaded). Anomalies are departures from the (a) 1979–95 and (b) 1950–79 base period means.

cits observed in the southern and eastern sectors. This dryness is attributed to a substantially weakened monsoon trough and a southward displacement of the intertropical convergence zone (ITCZ). In the north, the generally drier-than-normal conditions were linked to a persistent upper-level ridge that was embedded within an anomalous large-scale circulation pattern across the United States and Mexico.

During SON 1997 drier-than-normal conditions persisted across large sections of interior Mexico (Fig. 44b), in response to an early retreat of the summer monsoon. These conditions were associated with an El Niño–related strengthening of the subtropical ridge from the central North Pacific to the Caribbean Sea (see Bell and Halpert 1998, their Fig. 27d). In contrast to this dryness, the Baja Peninsula recorded above-normal precipitation during the season, in response to rains associated with Hurricane Nora in September. Portions of southern Mexico also recorded above-normal precipitation during the season, in response to three tropical systems during October and November.

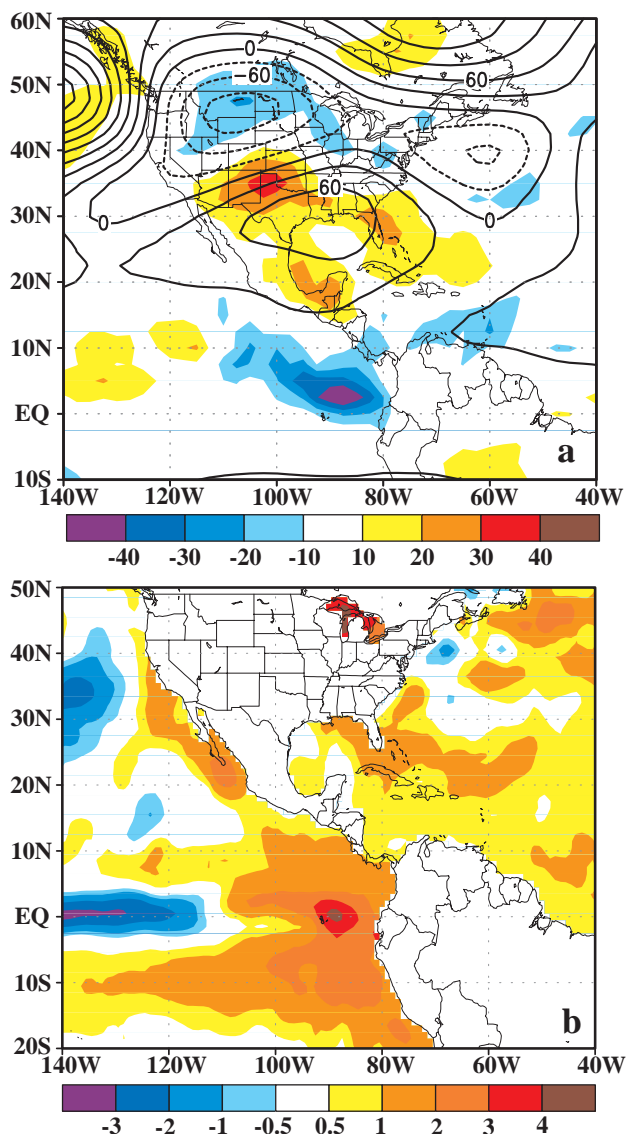An unusual aspect of the Mexican drought was the continuation of substantially below-normal rainfall during DJF 1997–98 across most of the country (Fig. 44c), despite the continuation of strong El Niño conditions. Historically, above-normal winter rainfall is observed across central and northern Mexico during these episodes (Ropelewski and Halpert 1986), which helps to alleviate the rainfall deficits that typically develop during the previous summer and fall.

This continuation of drought conditions during DJF 1997–98 was related to three distinct changes in the large-scale flow and vertical motion field. First, much of Mexico was situated slightly upstream of the mean upper-level trough axis in a region of descend-
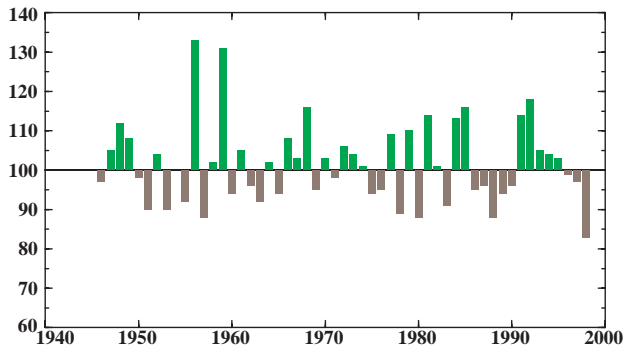
FIG. 43. Aerially weighted percent of normal precipitation relative to the 1961–90 base period for the July–June period over Mexico. (Analysis provided by the Mexican Meteorological Service.)

with respect to the upper-level trough differs from the climatological mean, in which the country is situated downstream of the mid-Pacific trough in a region of broad southwesterly flow and ascending motion.

Second, the atmosphere over Mexico also experiences ascending motion in the climatological mean due to its location in the right entrance region of the subtropical jet. However during DJF 1997–98, this jet entrance region was exceptionally ill defined (see section 3c) and did not favor ascending motion over much of the country. Third, dryness during the period also resulted from reduced storminess across Mexico, in response to a very intense wintertime jet stream that kept the main storm track over the southern tier of the United States.

Although the MAM season is normally dry in Mexico, precipitation totals during MAM 1998 were less than 20% of normal throughout most of the country (Fig. 44d). This dryness was directly related to strong subsidence beneath the highly amplified subtropical ridge (Figs. 27b, 40). The dryness during May and June reflected a 4–6-week delay in the onset

ing motion (see Fig. 29c). This feature represented an extreme eastward shift of the mid-Pacific trough to the Americas, and was consistent with previously described El Niño–related changes in the upper-level height field across the subtropical North Pacific (see section 3c, Figs. 29, 30). This positioning of Mexico
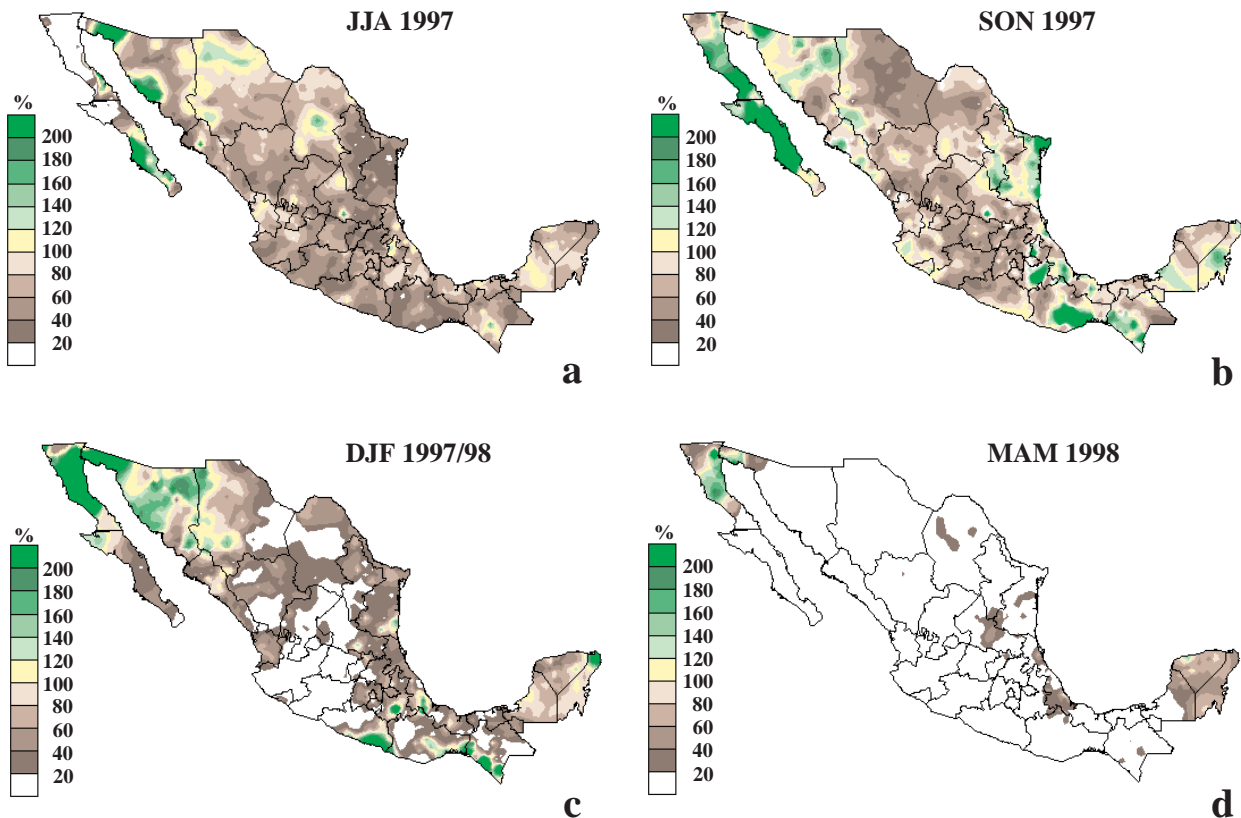

FIG. 44. Percent of normal precipitation relative to the 1961–90 base period across Mexico for (a) JJA 1997, (b) SON 1997, (c) DJF 1997/98, and (d) MAM 1998. Note: White indicates areas that received less than 20% of normal precipitation for the season. (Analysis provided by Mexican Meteorological Service.)

of monsoon rains and culminated in widespread forest fires, which peaked in May and early June 1998. Accompanying these conditions, extreme drought also developed across the Gulf Coast states of the United States during May–June 1998 [see section 4a(2)]. The Mexican drought eased considerably during July and August, as the ITCZ shifted northward and the monsoonal rains became reestablished in association with the development of La Niña conditions.

b. Asia

1) INDIAN SUMMER MONSOON

The Indian summer monsoon typically lasts from June through September, with large areas of western and central India receiving more than 90% of their total annual rainfall during the period, and southern and northwestern India receiving 50%–75% of their total annual rainfall. Overall, area-averaged monthly rainfall totals range from 200 to 300 mm, with the largest values observed during the July–August peak in the monsoon season (Fig. 45c).

Overall, area-averaged rainfall was near normal across India during June and July 1998, and above normal during both August and September (Fig. 45c). Abundant rains then continued through October, when area-averaged totals reached 130 mm and exceeded the long-term average by 30%.

Regionally, the 1998 season featured abundant rains (1200–1600 mm) in the typically heavy rainfall area of western India (Fig. 45a), which is 200–600 mm above the long-term mean (Fig. 45b). Elsewhere, seasonal rainfall was near normal over most of India, with above-normal totals confined to western Nepal and adjacent India and below-normal totals observed in the extremely heavy rainfall areas of Burma and Bangladesh.

The 1998 monsoon season also featured several episodes of catastrophic human loss. Locally heavy rains and flooding killed more than 2800 people in India and Bangladesh and another 250 people in Nepal. Farther west, a major Arabian Sea cyclone hit Gujarat, India, on 9 June, claiming 1126 lives. In Pakistan and northwestern India very hot temperatures typically precede the monsoon rains. From mid-May through early June 1998, this heat was extreme with temperatures occasionally exceeding 50°C (122°F). This heat wave claimed an estimated 2500 lives.

The upper-level monsoon ridge typically extends from northeastern Africa to southeastern Asia (Fig. 46a) and exhibits considerable interannual variability in its strength and zonal extent. During JJA 1998 the ridge was stronger than average across northern Africa, the Indian subcontinent, and southeastern Asia (Fig. 46b). This enhanced ridge was associated with a persistent pattern of above-normal heights across the subtropical North Atlantic and most of Eurasia, suggesting a link to the larger-scale circulation features and not to the localized regions of enhanced rainfall over India. In the region downstream of the amplified ridge enhanced cyclonic flow during June and July contributed to excessive rainfall and catastrophic flooding in the Yangtze River basin of central China [see section 4b(2)].

In contrast, the 1997 monsoon season featured a suppressed monsoon ridge from northern Africa eastward to southeastern Asia, despite a pattern of rainfall anomalies over India (Bell and Halpert 1998, see
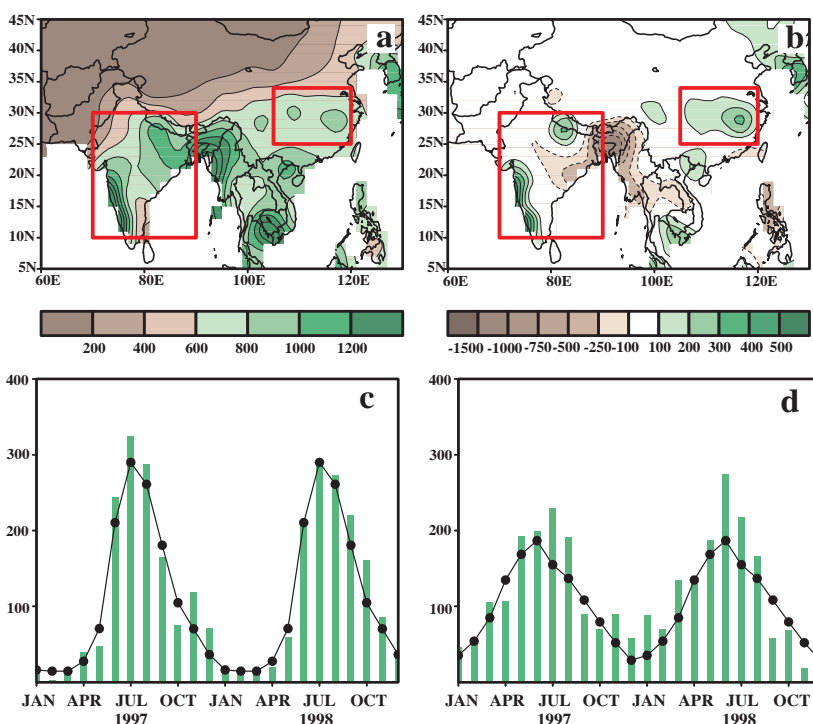

FIG. 45. (a) Total precipitation (mm) and (b) precipitation anomalies (mm) for June–September 1998. Monthly time series of total precipitation (mm, bars) and the 1961–90 mean (mm, line) averaged over (c) the boxed region centered on India and (d) the boxed region centered on eastern China.

their Figs. 49 and 52) that was similar to that observed in 1998. Accompanying this suppressed ridge was a pronounced southward shift in the extratropical westerly winds along its northern flank, with westerly disturbances impacting northern India and southeastern Asia during much of June–July 1997. These conditions led to severe flooding in southern China and southeastern Asia, which contrasts with the flooding in central China observed during 1998.

2) Yangtze River flooding: July–August 1998

The Yangtze River extends from the Tibetan Plateau to eastern China and is the third longest river in the world. During 1998, record flooding of the Yangtze River and adjacent river valleys ultimately affected more than one-fifth of the entire population of that country and was associated with more than 3600 deaths. The flooding destroyed approximately 7.3 million houses and damaged another 13.8 million. It also destroyed 45 000 schools, which directly affected 8.5 million school children. The estimated total damage from the flooding was $32 billion (U.S.).

The catchment basin of the Yangtze River, approximated by the boxed region in Fig. 45a, experiences a well-defined rainy season, with the largest totals typically observed during the April–August warm season and the smallest totals observed during the November–March cool season (Fig. 45d). Area-averaged rainfall totals are largest during May–July, with a peak of 200 mm normally observed in June. There is also considerable interdecadal and interannual variability in summertime rainfall across the Yangtze River basin (Fig. 47). For the period 1930–present, particularly wet periods [illustrated by a time series of June–July rainfall totals at Nanchang, which is located in the northeastern part of the Yangtze River basin (Fig. 48a)] have included 1930–40, 1962–80 and 1992–98, while dry periods have included 1955–62 and 1980–90.

During June–September 1998 area-averaged precipitation totals were significantly above normal in the Yangtze River basin (Fig. 45d). The most excessive rainfall occurred during June and July, when area-
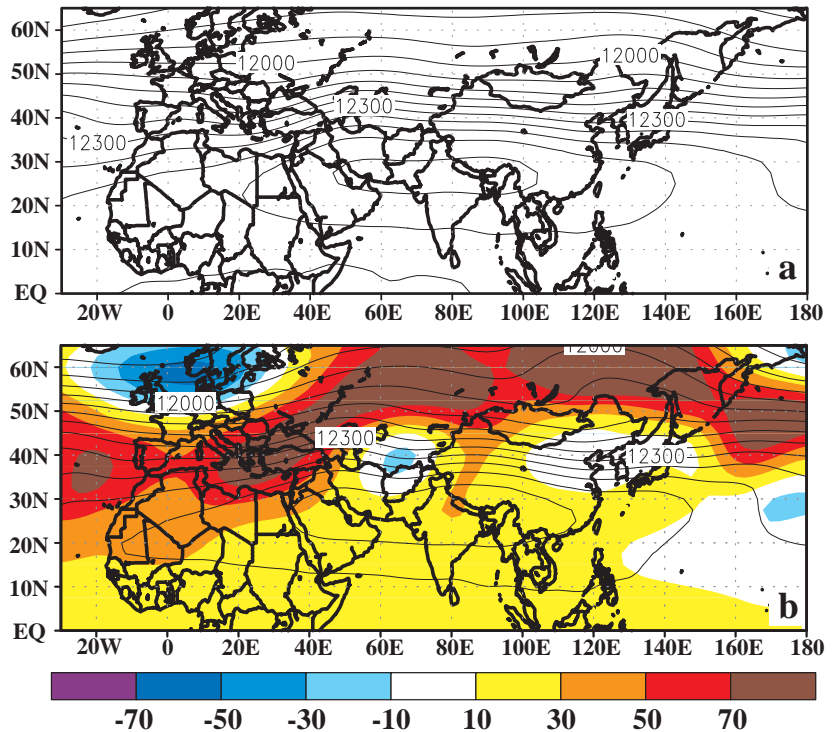

Fig. 46. June–August 200-hPa height (contours, m) for (a) the climatological mean and (b) the 1998 season. Anomalies (shaded, m) are also shown for the 1998 season in (b). Climatology and anomalies are computed from the 1979–95 base period means.

averaged totals exceeded 300 mm and 220 mm, respectively. Overall, the largest anomalies were observed over the eastern portion of the basin in the region, which includes Nanchang (Fig. 45b). At this location, record June–July 1998 rainfall totals of 1000 mm surpassed the previous record of approximately 950 mm set in 1954 (Fig. 47).

In June more than 200 mm of rain was observed throughout the southern half of the Yangtze River basin (Fig. 48a), with totals exceeding 400 mm (150%–200% of normal, Fig. 48b) in the vicinity of Nanchang, in the south-central region near Guilin and in the southwest near Kumming. Much of this excessive rainfall occurred between 12 and 26 June, when Nanchang and Guilin recorded 510 mm and 650 mm, respectively (Fig. 49). These stations recorded more than 25 mm of rain on 6 and 8 days, respectively, during this 15-day period, and each recorded more than 50 mm of rain on 5 days. These excessive rains followed a prolonged period of above-normal precipitation and snowfall during the 1997–98 cool season, which increased the flood potential by producing higher than normal river levels prior to the onset of the rainy season. These conditions then contributed to the

onset of the first major flooding of the Yangtze River beginning in early July.

During July an additional 200–400 mm of rain was observed throughout the southern half of the basin (Fig. 50a), with the largest totals again observed in the eastern, south-central, and southwestern sections. Monthly rainfall totals averaged more than 150% of normal in the east, with many locations recording totals of 200%–300% of normal (Fig. 50b). The largest totals exceeded 600 mm in the region northwest of Nanchang, which is more than 400% of the normal July total. Much of the excessive rainfall at Nanchang occurred during 20–25 July when more than 345 mm were recorded (Fig. 49). During this 6-day period, totals exceeded 25 mm on 5 days and exceeded 60 mm on 3 days. This excessive rainfall contributed to additional flooding at the end of the month.

During August, rainfall returned to near normal in the region south of the Yangtze River (Fig. 51a), but averaged 200–300 mm (150%–200% of normal) along and north of the river (Fig. 51b). Despite these lower totals, the continuation of normal and above-normal rainfall over such a large portion of the Yangtze River basin further exacerbated flooding conditions.

Much of the summertime rainfall across the Yangtze River basin and southern China is convective in nature and is sometimes triggered by midlatitude disturbances embedded in the westerly flow in the region north of the Asian monsoon ridge. The interannual variability of this westerly flow and therefore the interannual variability of rainfall in the Yangtze River basin, can be influenced by both the amplitude and northward/eastward extent of the monsoon ridge. For example, Bell and Halpert (1998) noted that excessive rainfall across southern China during 1997 was linked to a series of powerful extratropical disturbances moving well south of their nor-

mal position in response to a poorly developed and much weaker-than-average strength of the upper level monsoon ridge. During 1998 the excessive rainfall during both 12–26 June and 20–25 July was linked to the persistence of a strong low-level cyclonic circulation centered over the heart of the Yangtze River basin (near 30°N, 110°E) and to its attendant warm frontal boundary and very strong wind shift line which extended eastward along an axis nearly coincident with the eastern half of the river basin (Figs. 52a,b). During both periods these features were linked to extratropical low pressure areas and were strengthened at times by powerful upper-level midlatitude disturbances propagating eastward along the northern flank of an amplified monsoon ridge (see Fig. 46b).

c. Africa

1) June–September 1998: Western Africa rainy season

The Sahel region (bounded by 8°–18°N, 17°W–20°E and indicated by the boxed region in Fig. 53) re-
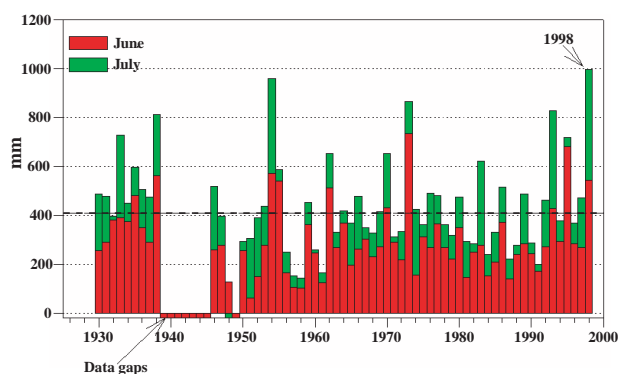

FIG. 47. June–July rainfall totals (mm) at Nanchang, China (location shown in Fig. 48a), dating back to 1930. (Analysis provided by GPCC.)
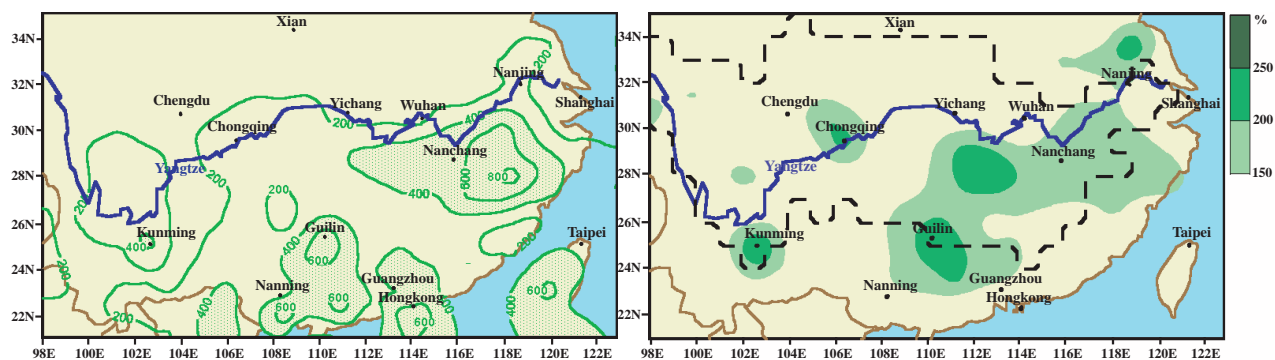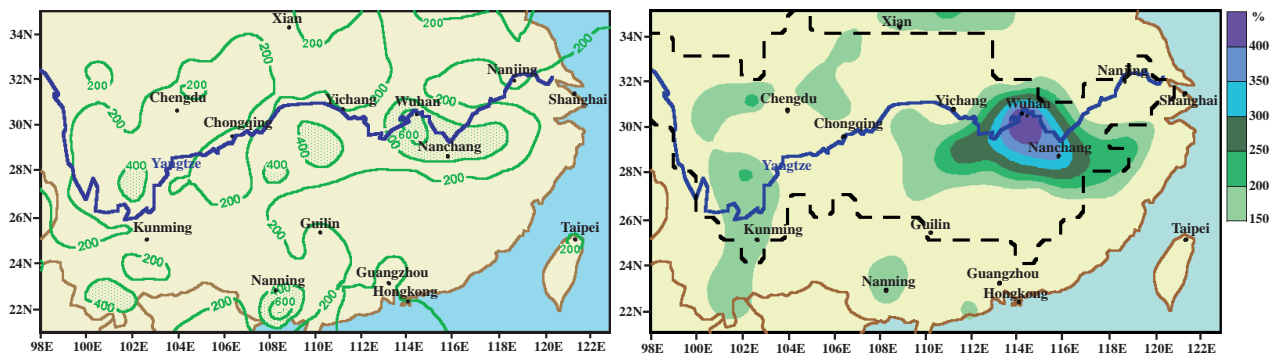

FIG. 48. June 1998 (a) rainfall anomalies (mm) and (b) percentage of normal rainfall across China. Anomalies are calculated from the 1961–90 base period means. Dashed region in (b) approximates the Yangtze River catchment basin. (Analysis provided by GPCC.)

ceives approximately 90% of its mean annual rainfall during the June–September period. This rainfall pattern is closely related to the north–south movement of the ITCZ, which starts its northward movement in March and reaches its northernmost position (near 15°N) in August. Rainfall typically varies widely across the region, with long-term average totals reaching 1300 mm in the southwest, 700 mm in the southeast, and 100–300 mm in the north. Overall, the Sahel region as a whole experienced a near-normal rainy season during 1998 (Fig. 53b), which followed significantly below-normal rainfall during the 1997 season (Bell and Halpert 1998).

During 1998 below-normal rainfall was confined to the southwestern Sahel, with the largest deficits (exceeding 500 mm) observed in Guinea and northern Liberia. Other regions experiencing below-normal rainfall included southern Senegal, Guinea-Bissau, and southwestern Mali. In contrast, rainfall averaged 100–200 mm above normal (120%–200% of normal) over much of Niger during the season. Rainfall totals were particularly large during September, which resulted in devastating floods over eastern Mali, western Niger, and southeastern Niger.

Despite near-normal rains for the season as a whole, the onset of the rains was delayed across central and northern Senegal, Mauritania, western Mali, and southwestern Chad. In June and July, rainfall totals across northern Senegal and Mauritania only
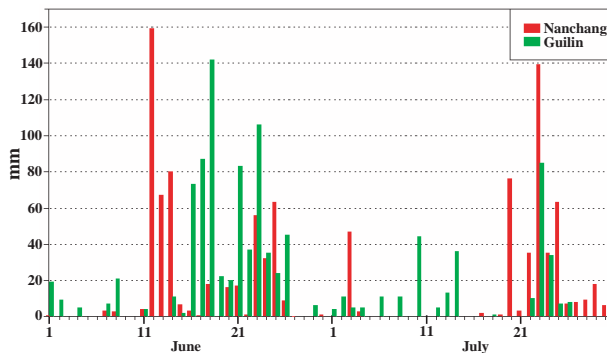
FIG. 49. Daily rainfall totals (mm) at Nanchang, China (red), and Guilin, China (green), during June–July 1998. (Analysis provided by GPCC.)

FIG. 50. July 1998 (a) rainfall anomalies (mm) and (b) percentage of normal rainfall across China. Anomalies are calculated from the 1961–90 base period means. Dashed region in (b) approximates the Yangtze River catchment basin. (Analysis provided by GPCC.)
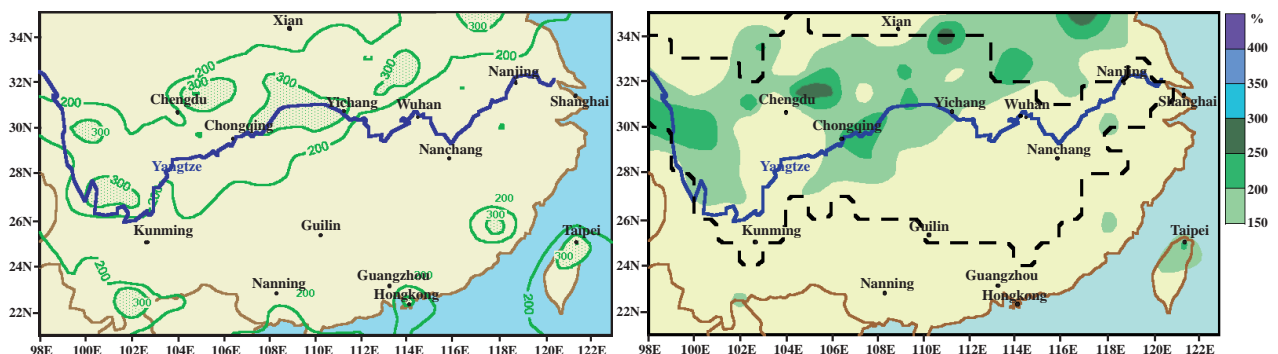
FIG. 51. August 1998 (a) rainfall anomalies (mm) and (b) percentage of normal rainfall across China. Anomalies are calculated from the 1961–90 base period means. Dashed region in (b) approximates the Yangtze River catchment basin. (Analysis provided by GPCC.)

reached 50% of normal. However, the dryness in these regions was alleviated by heavy rains during the second half of August and September.

2) OCTOBER 1997–APRIL 1998: SOUTHERN AFRICA RAINY SEASON

The southern Africa rainy season typically lasts from October to April and reaches maximum strength from December through March. Most locations receive more than 75% of their mean annual rainfall during the rainy season, with some parts in the northwest receiving 90% of their normal annual rainfall. The interannual variability of rainfall over southern Africa shows a strong relationship to the ENSO cycle (Ropelewski and Halpert 1987, 1989), with below-normal rains typically observed during El Niño episodes and above-normal rains observed during La Niña episodes.

Overall, southern Africa experienced a drier and shorter-than-normal rainy season during 1997/98 (Fig. 54), with substantial rainfall ending in March and exceptional dryness occurring during December 1997, February and April 1998 (Fig. 54d). These conditions were consistent with the ongoing strong 1997/98 El Niño, and contrasted with the active and prolonged 1996–97 rainy season (Bell and Halpert 1998).

During 1998 the most abundant rains (Fig. 54a) covered the climatologically wet region of eastern South Africa (50–100 mm above normal) and Mozambique (100–500 mm below normal). Significantly below-normal seasonal rainfall (Fig. 54b) was observed in the climatologically dry regions of western South Africa, Namibia, and western Botswana, where totals in many locations (50–150-mm deficits) dropped below the fifth percentile (Fig. 54c).

Significantly drier-than-normal conditions (50%–65% of normal rainfall) were also observed in northeastern South Africa and southern Zimbabwe, where totals were also generally below the fifth percentile. Accumulated rainfall and daily rainfall totals during November 1997–April 1998 are shown for two reporting stations located within these dry regions: Pietersburg, South Africa (Fig. 55), and Bulawayo Airport, Zimbabwe (Fig. 56). In both regions, rainfall was suppressed (Figs. 55a, 56a) and episodic (Figs. 55b, 56b) during the season, with prolonged periods of little to no rainfall recorded. In Pietersburg, exceptional dryness persisted from late November 1997 into late January (Fig. 55b), and again from mid-February through April when only two substantial (exceeding 25 mm) rain events occurred. At Bulawayo Airport, nearly all
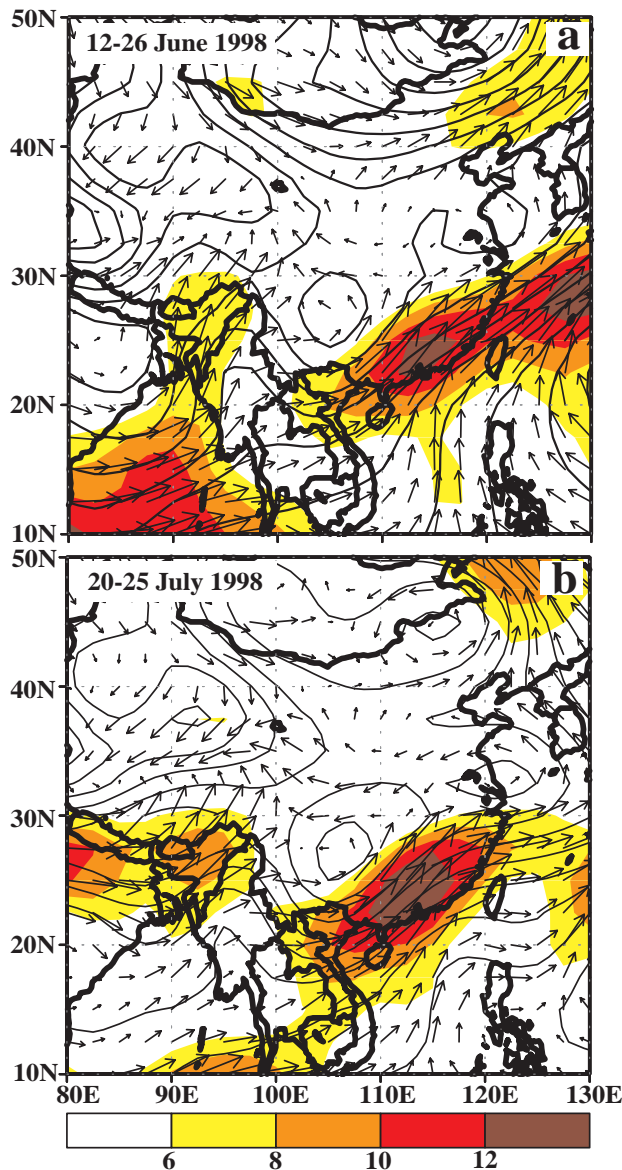

FIG. 52. The 850-hPa heights (contours, m), wind speeds (shaded, m s^{-1}), and wind vectors during (a) 12–26 June 1998 and (b) 20–25 July 1998.

of the substantial precipitation occurred during January (Fig. 56b), and dryness at this station was particularly acute during February–April when only three days of measurable precipitation were recorded.

d. South America

During the first half of 1998 the strong Pacific warm episode greatly impacted temperature (Fig. 9a) and precipitation (Figs. 57a,b) patterns over South America. Typical El Niño–related impacts (see, e.g., Ropelewski and Halpert 1987, 1989; Aceituno 1988; Halpert and Ropelewski 1992; Kousky and Kayano
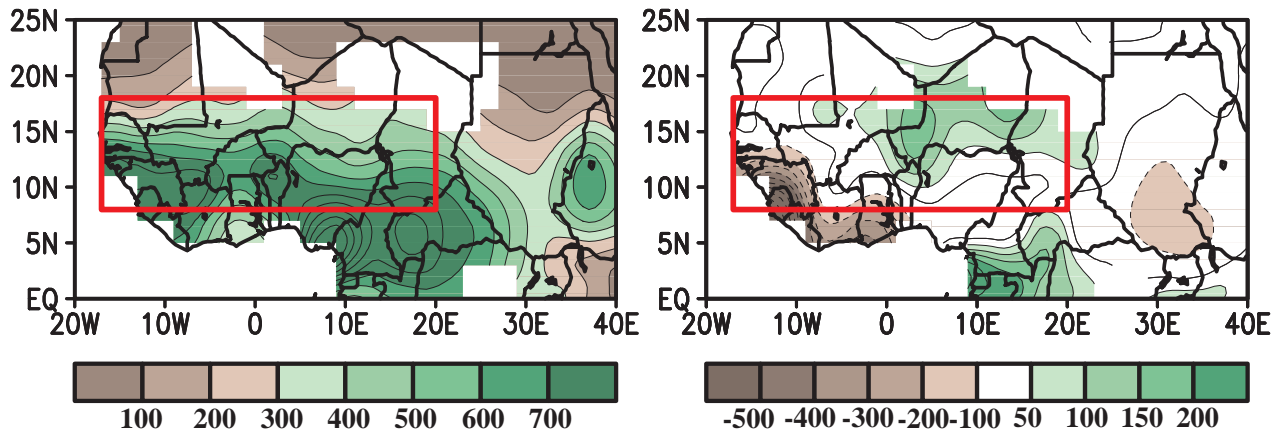
FIG. 53. June–September 1998 (a) total precipitation (mm) and (b) anomalies (mm) for the African Sahel region. The boxed region denotes the approximate boundaries of the West African Sahel region.

1994) at various times of the year over South America include 1) drier-than-normal conditions over northern South America, the Amazon Basin, and northeastern Brazil; 2) wetter-than-normal conditions over southern Brazil, Uruguay, northeastern Argentina, and over coastal Ecuador and northern Peru; and 3) above-normal temperatures over eastern Brazil. All of these features were evident during the 1997–98 El Niño.

During December 1997–May 1998 drier-than-normal conditions extended across most of northern South America, except for western sections of Ecuador and northern Peru. Rainfall deficits of more than 300 mm were observed during DJF (Fig. 57a) in the central and western Amazon Basin, and more than 400 mm during MAM over portions of northeastern Brazil (Fig. 57b). This dryness contributed to unprecedented wildfire activity in the northern Amazon Basin during January–March, and in southwestern Brazil and Bolivia later in the year.

In contrast, excessive rainfall (up to 10 times normal) covered western Peru and Ecuador from

November 1997 through May 1998, leading to severe flooding and mudslides in both countries that killed 450 people and caused more than $3 billion (U.S.) in
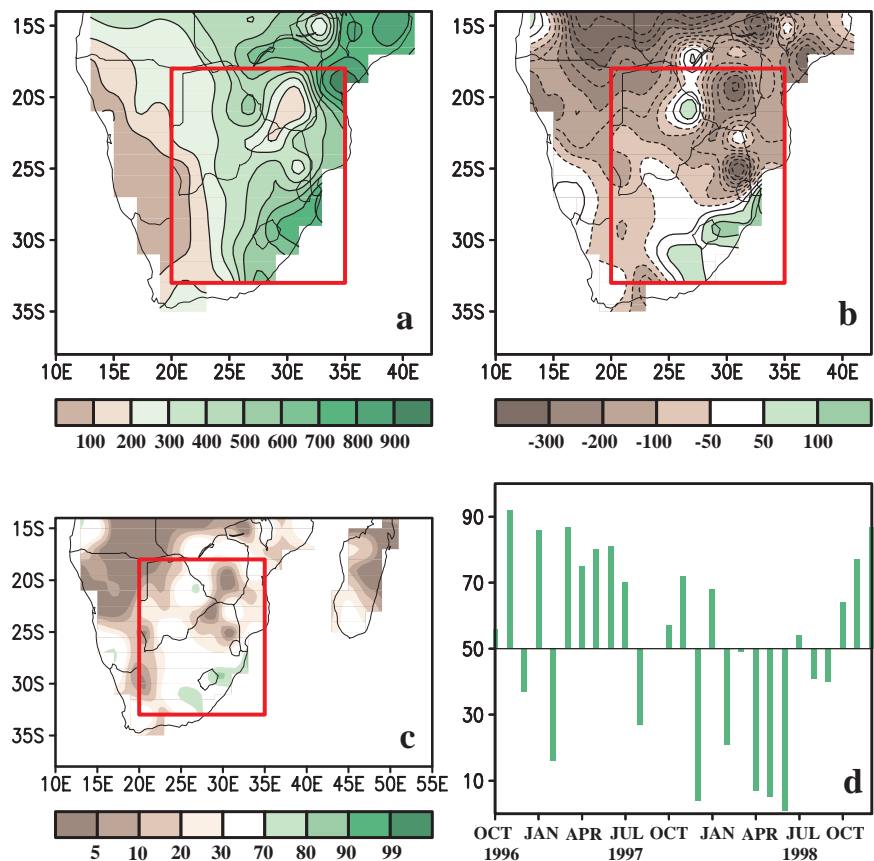
FIG. 54. October 1997–April 1998 (a) total precipitation (mm), (b) precipitation anomalies (mm), and (c) precipitation percentiles based on a gamma distribution fit to the 1961–90 base period. (d) A monthly time series of precipitation percentiles, based on precipitation totals averaged over the boxed region depicted in (a)–(c).

damage. In coastal Peru, where very little rainfall normally occurs, totals during the period reached 1500–2200 mm (Fig. 58). In extreme northwestern Peru, the city of Tumbes (Fig. 58a) experienced much of this rain during January–April, when totals reached 1750 mm. Overall, more than 300 mm of precipitation was measured in each of these months at this location, with the largest totals (700 mm) observed in February. Farther south in Piura, Peru (Fig. 58b), the excessive rainfall (approximately 1450 mm) was observed during January–March, with the largest totals (650 mm) recorded in January.

Above-normal rainfall was also observed during December 1997–May 1998 over southern Brazil, Paraguay, Uruguay, and northeastern Argentina (Figs. 57a,b), with many areas recording surpluses exceeding 200 mm in each season. In April alone rainfall in southern Paraguay and northeastern Argentina reached 400 mm (200%–400% of normal). Overall, the excessive rains led to major flooding in each of these countries.

The excessive rainfall in Uruguay and southern Brazil during December 1997–May 1998 is highlighted by time series for two individual stations (Fig. 59). At Salto, Uruguay (Fig. 59a), 1450 mm of rain was recorded between mid-December 1997 and mid-April 1998 (normal is 450 mm), with 900 mm of rain observed during the 41-day period 20 December 1997–31 January 1998. Precipitation after this period was episodic, falling mainly during two extreme rain events that occurred in early March and mid-April. In extreme southern Brazil, Santa Maria experienced

the onset of heavy rains in mid-December, and a continuation of excessive precipitation through May (Fig. 59b). Totals during the period reached 1300 mm (normal accumulation is 1000 mm), with the bulk of the rain occurring during three distinct periods: late December (375 mm), late January–early February (175 mm), and the first half of March (350 mm).

This above-normal rainfall was associated with persistent upper-level circulation features over the subtropics and extratropics. Prominent aspects of this circulation (Figs. 57c,d) included 1) positive upper-level height anomalies throughout the Tropics and subtropics; 2) negative height anomalies in the midlatitudes; 3) an enhanced thermal contrast, with positive temperature anomalies to the north of 25°S and negative anomalies over portions of central and northern Argentina (Fig. 9a); and 4) an enhanced jet stream and increased storminess in the subtropics along the poleward flank of the enhanced subtropical ridge. Similar circulation features also contributed to enhanced rainfall in these regions during June–November 1997 (Bell and Halpert 1998, see their Figs. 27c,d, and 29b).

As the rapid transition from El Niño to La Niña conditions occurred in the equatorial Pacific during May–June (see section 3a), upper-level circulation features over the South Pacific also evolved rapidly from those typical of warm episodes to those commonly found during cold episodes. For example, the negative height anomalies and anomalous cyclonic circulation observed near 40°S across the eastern South Pacific during the first half of 1998 were replaced by above-normal heights and an anomalous anticyclonic circu-
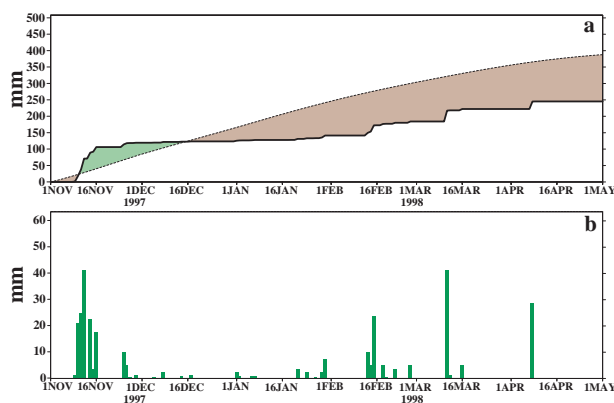

Fig. 55. Daily rainfall (mm) at Pietersburg, South Africa, during November 1997–April 1998: (a) accumulated observed (thick line) and accumulated climatological mean (thin line, 1961–90 base period), and (b) observed daily total. Shading in (a) shows the accumulated departure from normal, with brown shading indicating negative departures.
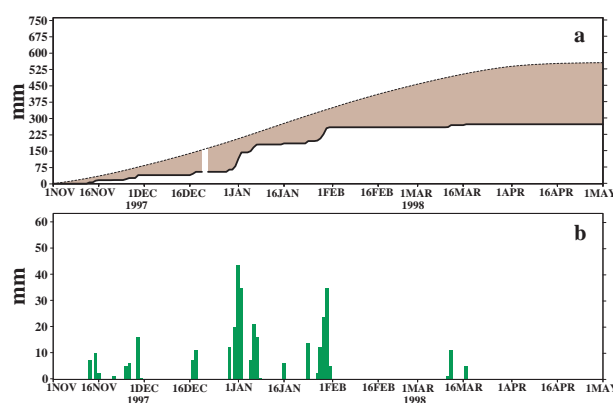

Fig. 56. Daily rainfall (mm) at Bulawayo, Zimbabwe, during November 1997–April 1998: (a) accumulated observed (thick line) and accumulated climatological mean (thin line, 1961–90 base period), and (b) observed daily total. Shading in (a) shows the accumulated departure from normal, with brown shading indicating negative departures.
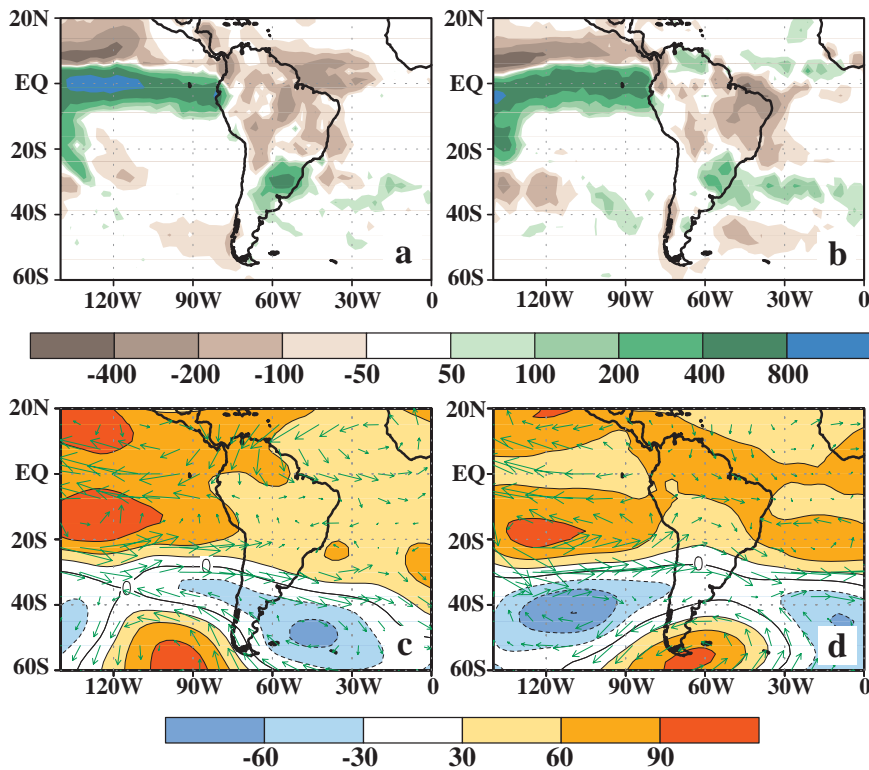
FIG. 57. (top) Precipitation anomalies during (a) DJF 1997–98 and (b) MAM 1998. (bottom) 200-hPa height and wind vector anomalies during (c) DJF 1997–98 and (d) MAM 1998. Anomalies are departures from the 1979–95 base period means.

tween 20° and 40°S across the eastern South Pacific (Figs. 60a,b) extending into central Chile and portions of southern Argentina, and to enhanced rainfall at higher latitudes of the South Pacific between 40° and 60°S.

e. Australia

Northern Australia (indicated by the boxed area in Fig. 61a) experiences a tropical climate with a well-defined rainy season that typically begins during October and ends in April (Fig. 61c). Much of the area receives more than 75% of its mean annual rainfall during this 7-month period, with portions of extreme northern Australia recording more than 90%. This annual cycle is strongly modulated by the Southern Oscillation, with below- (above-) normal rainfall often observed during Pacific warm (cold) episodes (Ropelewski and Halpert 1987, 1989).

Overall, the 1997–98 rainy season featured below-normal rainfall across the southern and central sections of this region, and above-normal rainfall in the vicinity of Darwin and in southern portions of the Cape York Peninsula (Fig. 61a). For the region as a whole, the above-normal rainfall occurred primarily

lation during JJA and SON (Figs. 60c,d). Also, the anomalous anticyclonic circulation in the subtropics was replaced by a cyclonic circulation anomaly. Accompanying these changes the jet stream shifted to well south of its normal position and completely disappeared from the 20°–40°S band (see Fig. 31b). This pattern contributed to drier-than-normal conditions be-
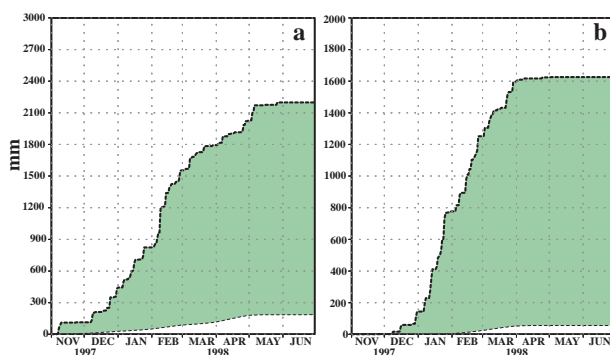

FIG. 58. November 1997–June 1998 accumulated observed (thick line) and accumulated climatological mean (thin line, 1961–90 base period) rainfall totals (mm) at (a) Tumbes, Peru, and (b) Piura, Peru. Shading shows the accumulated departure from normal, with green shading indicating positive departures.
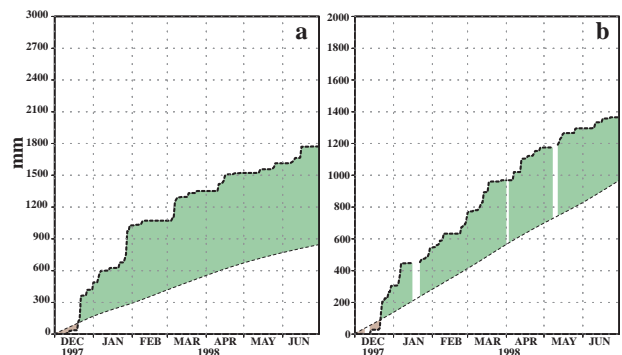

FIG. 59. December 1997–June 1998 accumulated observed (thick line) and accumulated climatological mean (thin line, 1961–90 base period) rainfall totals (mm) at (a) Salto, Uruguay, and (b) Santa Maria, Brazil. Shading shows the accumulated departure from normal, with green shading indicating positive departures.

during December 1997 and January 1998 (Fig. 61c), with substantially below-normal totals observed during October–November 1997 and February–March 1998.

In the extreme north, a series of intense rainfall episodes and tropical storms during December 1997–Jaunary 1998 contributed to record October–April rainfall totals at Darwin (2499 mm). At Katherine, located southeast of Darwin, a series of major rainfall episodes during late December (Fig. 62) was followed by an additional 914 mm of rain in January. For comparison, the annual average rainfall total at this station is 1000 mm. This excessive rain culminated with a major flooding episode in late January, triggered by more than 375 mm of rain during 25–26 January.

Elsewhere during the season, rainfall was below normal along most of the east coast, as well as across sections of the west and northwest. The most significant dryness was observed along the coastal regions of Queensland and New South Wales, where deficits at many locations exceeded 400 mm. However, these deficits soon disappeared as above-normal rainfall covered eastern Australia (defined by the boxed region in Fig. 61b) from April through November (Fig. 61d), including the climatologically drier months of June–September. This above-normal rainfall was consistent with the development and intensification of La Niña conditions. For the April–November period as a whole, rainfall surpluses averaged 50–200 mm over most of the region, with the largest anomalies (exceeding +400 mm) observed in eastern New South Wales. Above-normal rainfall (50–200-mm surpluses) also covered much of central and western Australia during this period. In association with this excess precipitation, the areas most affected by flooding included extreme southern Queensland, much of the northern half of New South Wales, and northwestern Australia.

In contrast, extreme southeastern Australia again experienced below-normal rainfall throughout the year, as severe rainfall deficiencies extended beyond 2 yr. The most severely affected regions were located immediately east and southeast of Melbourne, which experienced their driest two-year period in the historical record.
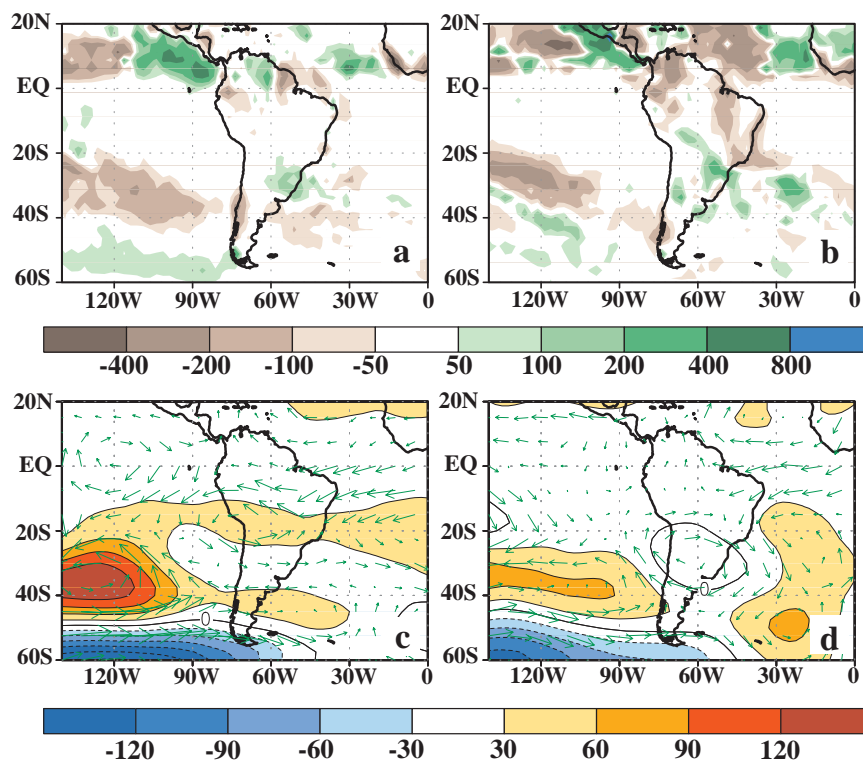

FIG. 60. (top) Precipitation anomalies during (a) JJA 1998 and (b) SON 1998. (bottom) 200-hPa height and wind vector anomalies during (c) JJA 1998 and (d) SON 1998. Anomalies are departures from the 1979–95 base period means.
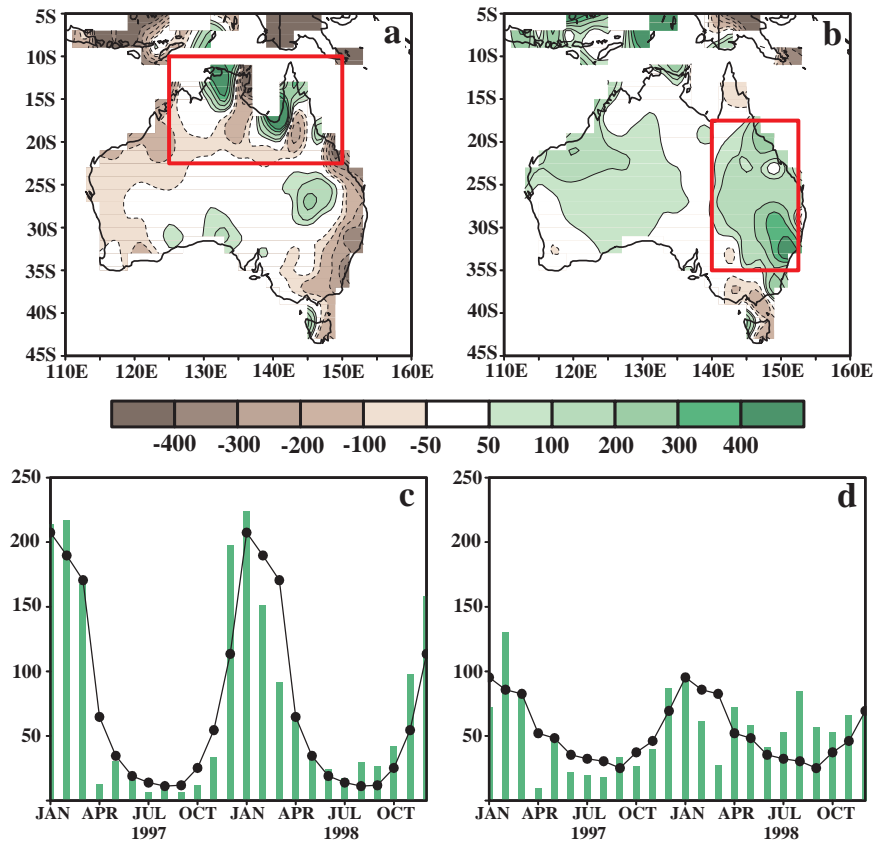
FIG. 61. Precipitation anomalies (mm) for (a) October 1997–April 1998 and (b) April–November 1998. Monthly time series of total precipitation (mm, bars) and the 1961–90 mean (mm, line) averaged over (c) the boxed region centered on Northern Australia and (d) the boxed region centered on eastern Australia.
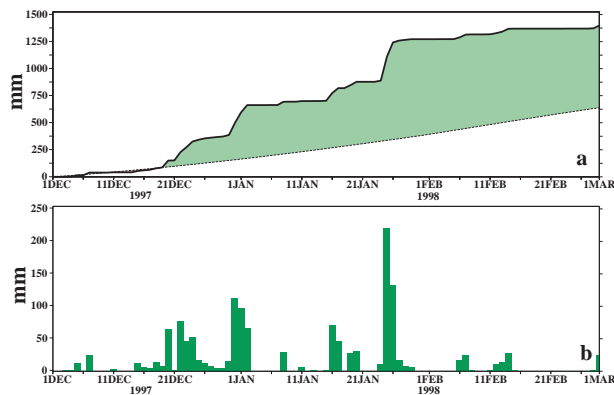

FIG. 62. Daily rainfall (mm) at Katherine, Northern Territory, Australia during December 1997–February 1998: (a) accumulated observed (thick line) and accumulated climatological mean (thin line, 1961–90 base period), and (b) observed daily total. Shading in (a) shows the accumulated departure from normal, with green shading indicating positive departures.
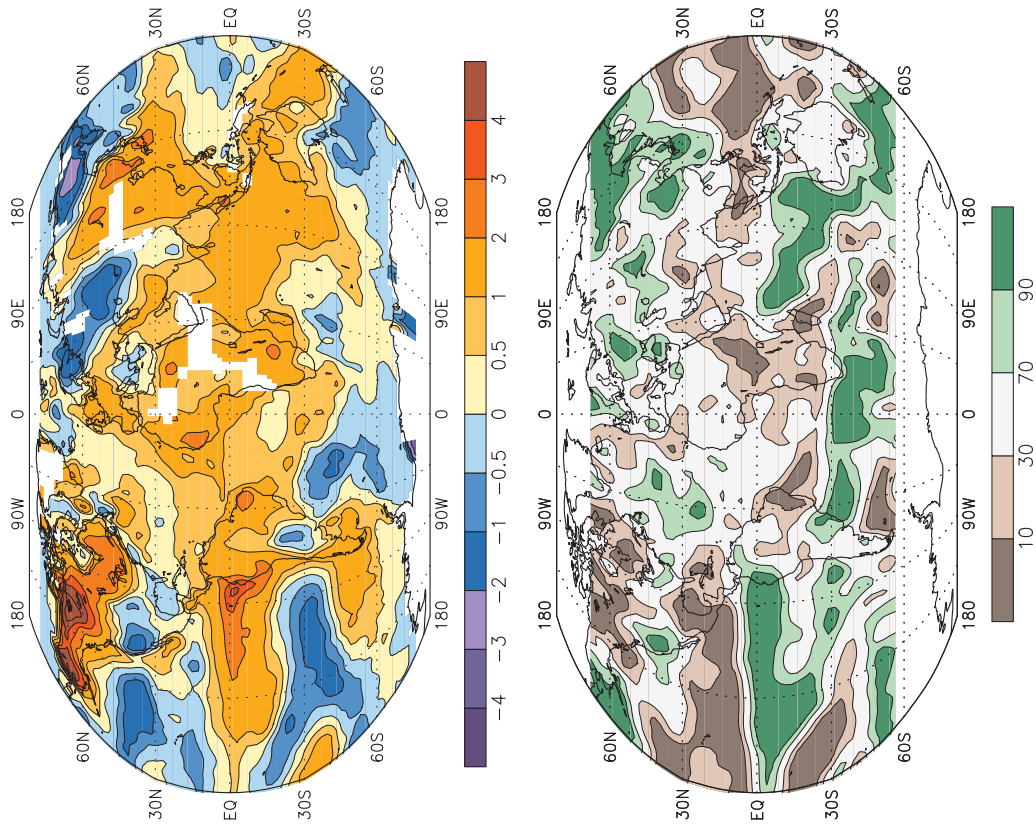
5. Seasonal summaries
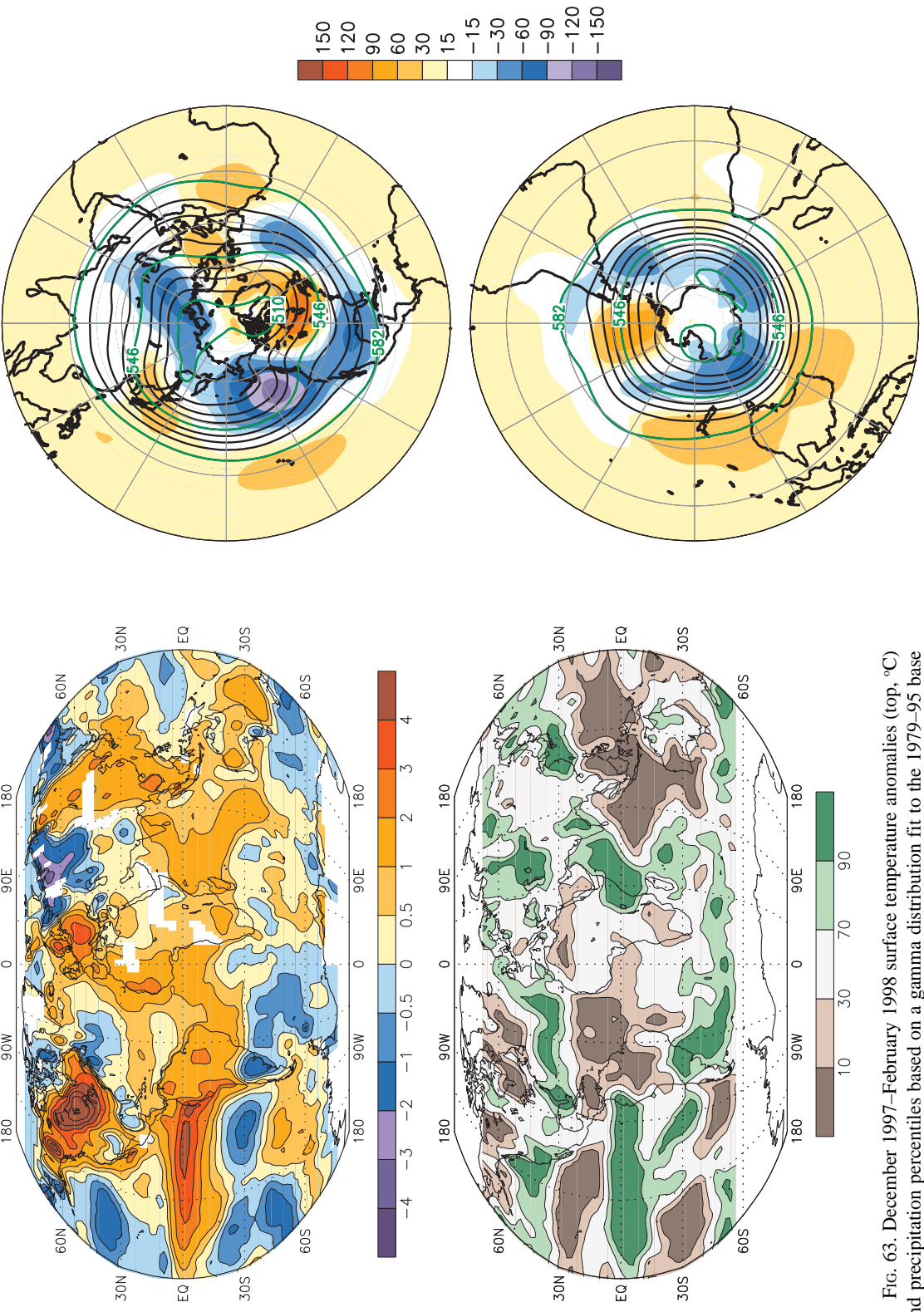
Fig. 63. December 1997–February 1998 surface temperature anomalies (top, °C) and precipitation percentiles based on a gamma distribution fit to the 1979–95 base period (bottom). Temperature anomalies (1961–90 base period) are based on station data over land and sea surface temperature data over water. Precipitation data are obtained from a merge of rain gauge observations and satellite-derived precipitation estimates (see Fig. 22 for analysis details). The analysis is omitted in data-sparse regions (white areas).
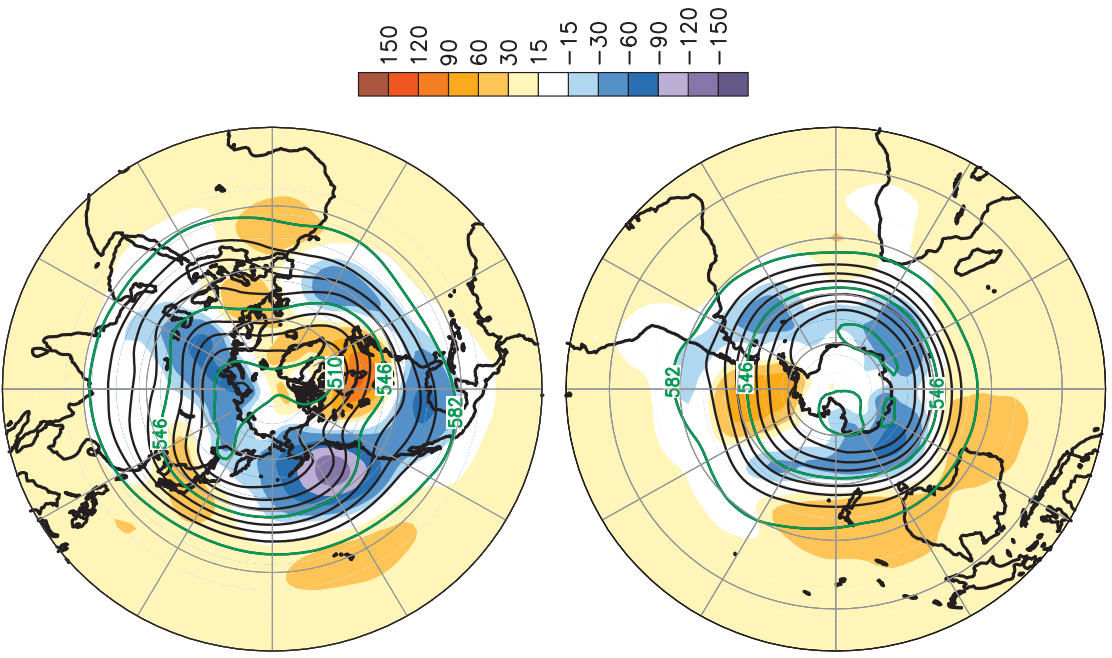
Fig. 64. December 1997–February 1998 Northern Hemisphere (top) and Southern Hemisphere (bottom) 500-hPa geopotential heights (contours, interval is 9 dam) and anomalies (shading). Anomalies are departures from the 1979–95 base period means.
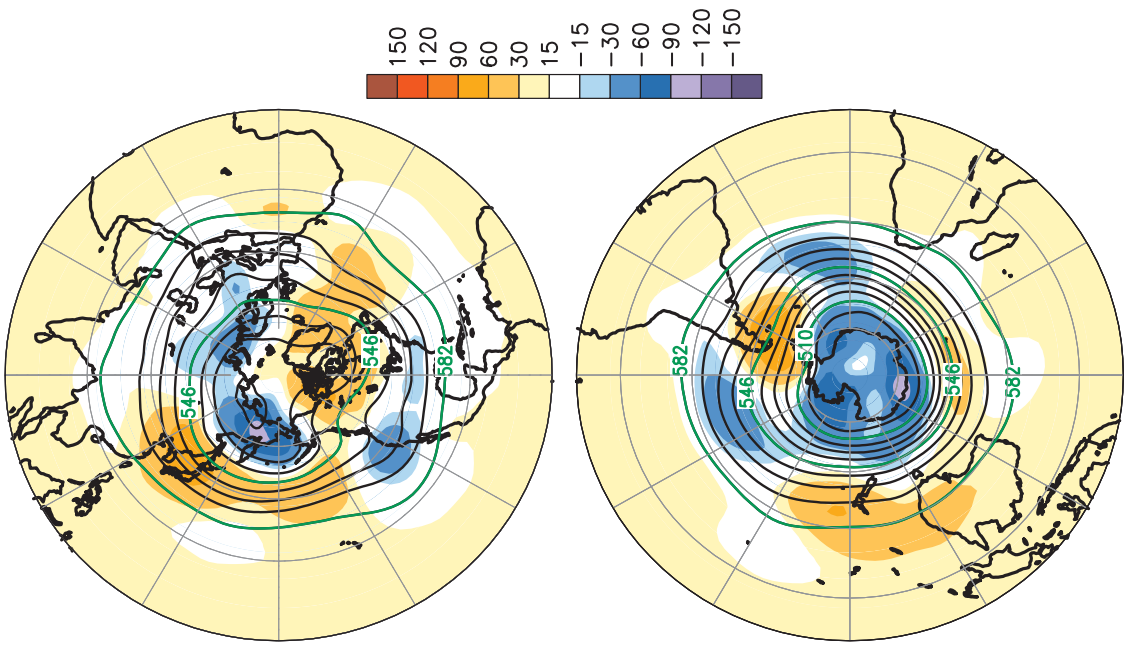
FIG. 66. March–May 1998 Northern Hemisphere (top) and Southern Hemisphere (bottom) 500-hPa geopotential heights (contours, interval is 9 dam) and anomalies (shading). Anomalies are departures from the 1979–95 base period means.

FIG. 65. March–May 1998 surface temperature anomalies (top, °C) and precipitation percentiles based on a gamma distribution fit to the 1979–95 base period (bottom). Temperature anomalies (1961–90 base period) are based on station data over land and sea surface temperature data over water. Precipitation data are obtained from a merge of rain gauge observations and satellite-derived precipitation estimates (see Fig. 22 for analysis details). The analysis is omitted in data-sparse regions (white areas).

Fig. 68. June–August 1998 Northern Hemisphere (top) and Southern Hemisphere (bottom) 500-hPa geopotential heights (contours, interval is 9 dam) and anomalies (shading). Anomalies are departures from the 1979–95 base period means.
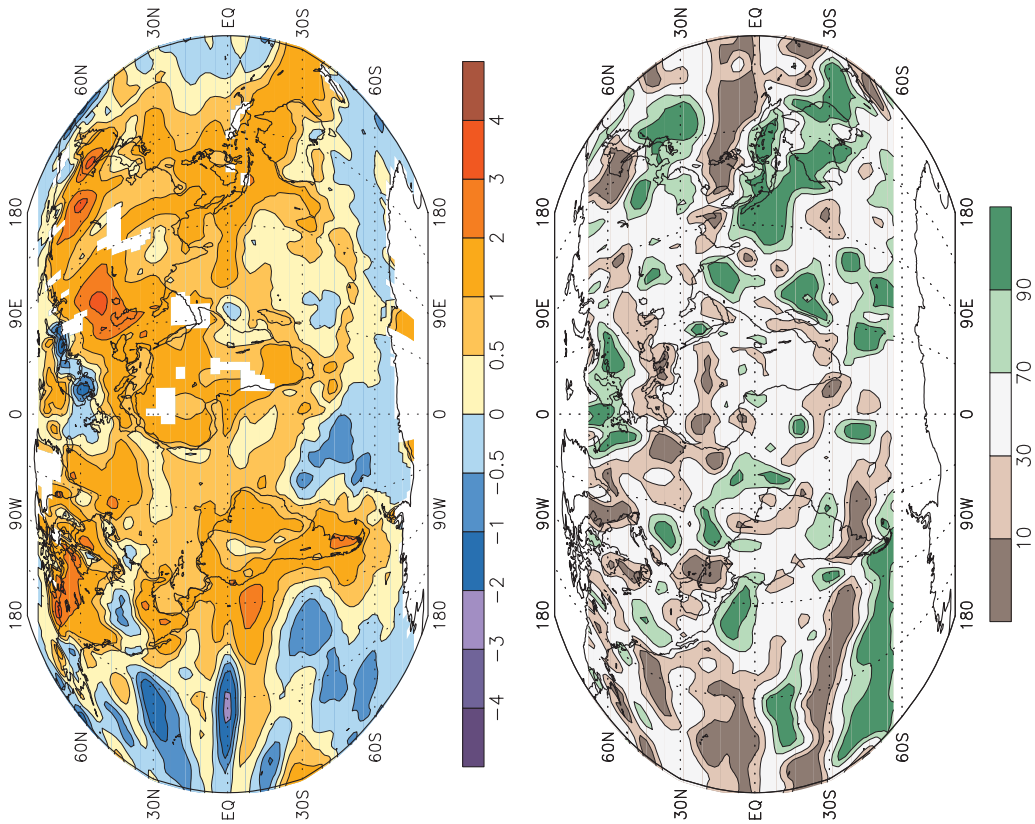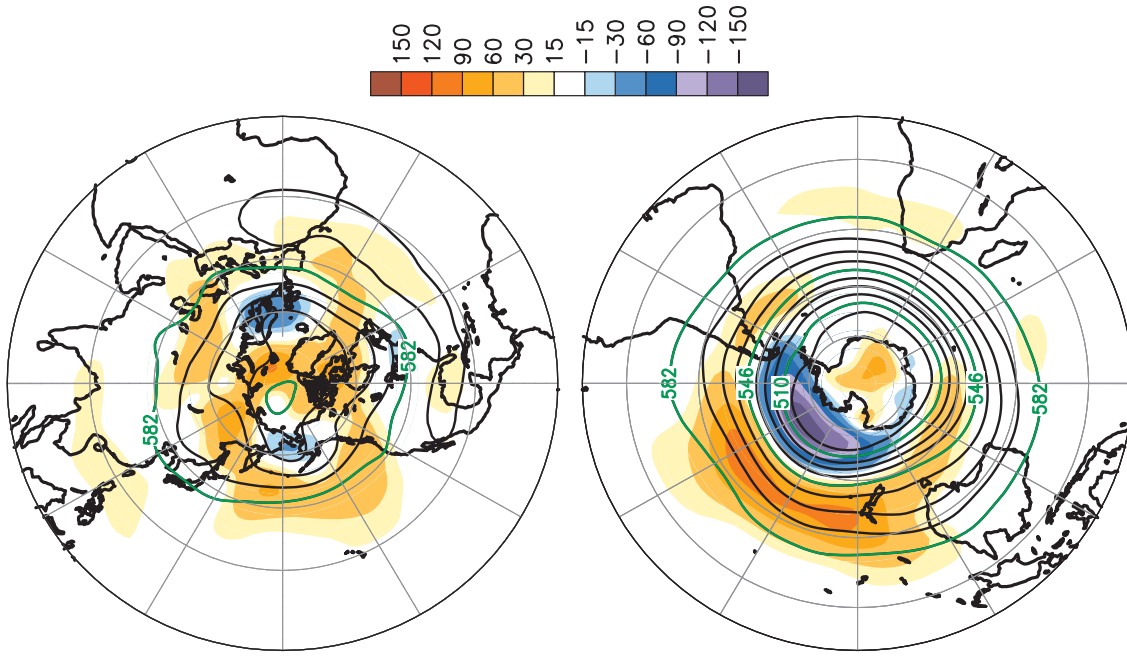

Fig. 67. June–August 1998 surface temperature anomalies (top, °C) and precipitation percentiles based on a gamma distribution fit to the 1979–95 base period (bottom). Temperature anomalies (1961–90 base period) are based on station data over land and sea surface temperature data over water. Precipitation data are obtained from a merge of rain gauge observations and satellite-derived precipitation estimates (see Fig. 22 for analysis details). The analysis is omitted in data-sparse regions (white areas).

Fig. 70. September–November 1998 Northern Hemisphere (top) and Southern Hemisphere (bottom) 500-hPa geopotential heights (contours, interval is 9 dam) and anomalies (shading). Anomalies are departures from the 1979–95 base period means.
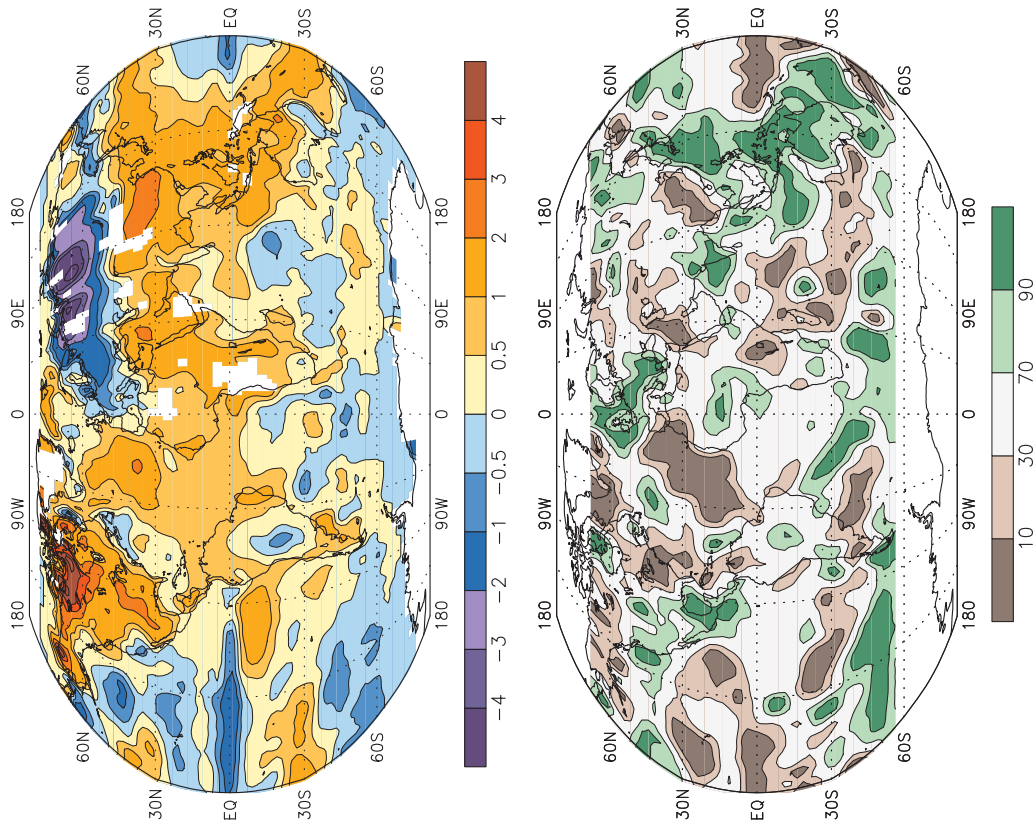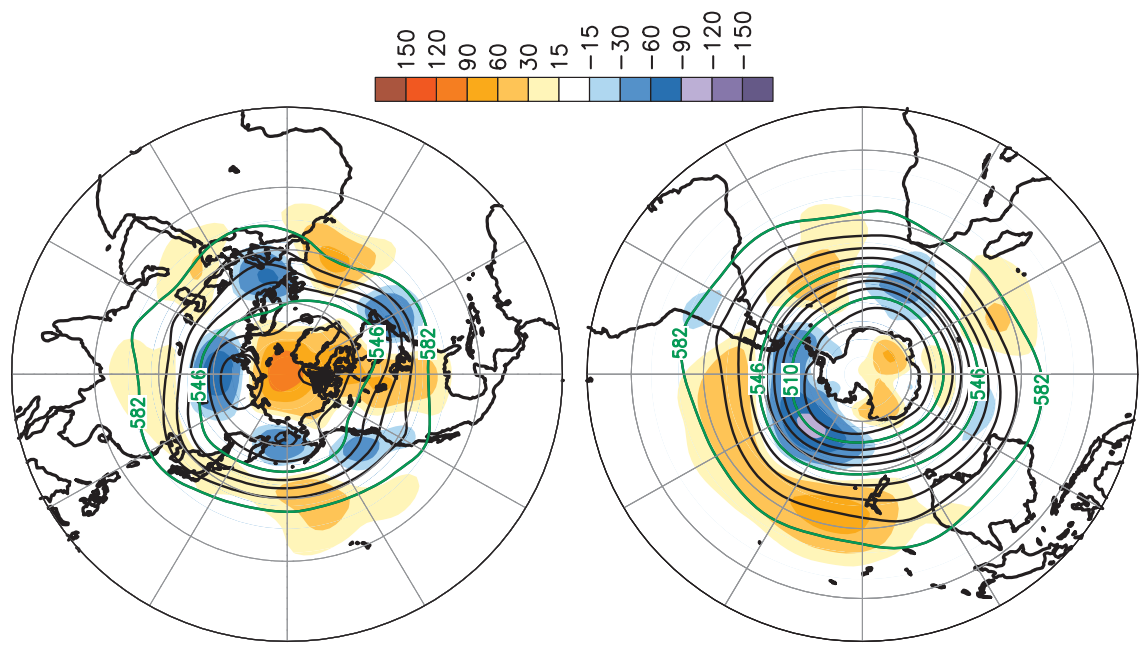

Fig. 69. September–November 1998 surface temperature anomalies (top, °C) and precipitation percentiles based on a gamma distribution fit to the 1979–95 base period (bottom). Temperature anomalies (1961–90 base period) are based on station data over land and sea surface temperature data over water. Precipitation data are obtained from a merge of rain gauge observations and satellite-derived precipitation estimates (see Fig. 22 for analysis details). The analysis is omitted in data-sparse regions (white areas).

Appendix: Contributors

Atmospheric Environment Service, Environment Canada
- D. Phillips
- R. Whitewood

Centro de Previsão de Tempo e Estudos Climáticos (CPTEC), Brazil
- I. Cavalcanti
- J. Marengo

Climate Analysis Section, National Climate Centre, Australian Bureau of Meteorology
- W. Wright

Climate Prediction Center/NCEP/NWS/NOAA
- D. Garrett
- J. Janowiak
- D. Lecompte
- C. Long
- P. Sabol
- W. Thiao
- R. Tinker

Climate Monitoring and Diagnostics Laboratory/ERL/NOAA
- J. Elkins
- D. Hofmann
- K. Masarie
- S. Oltmans

Climatic Research Unit, University of East Anglia, United Kingdom
- P. Jones

Department of Geography, Rutgers University
- D. Robinson

Global Precipitation Climatology Center, Deutscher Wetterdienst
- T. Fuchs
- B. Rudolph

Hadley Centre for Climate Prediction and Research, United Kingdom
- B. Horton
- M. O'Donnell
- D. Parker

Japan Meteorological Agency
- K. Shida

Mexican Meteorological Service (SMN)
- J. Espinosa

National Climatic Data Center/NESDIS/NOAA
- W. Brown
- R. Heim Jr.

Office of the New Jersey State Climatologist
- T. Estilow

References

Aceituno, P., 1988: On the functioning of the Southern Oscillation in the South American sector. *Mon. Wea. Rev.*, **116,** 505–525.

Barnston, A. G., R. E. Livezey, and M. S. Halpert, 1991: Modulation of Southern Oscillation–Northern Hemisphere mid-winter climate relationships by the QBO. *J. Climate*, **4**, 203–217.

Behringer, D. W., M. Ji, and A. Leetmaa, 1998: An improved coupled model for ENSO prediction and implications for ocean initialization. Part I: The ocean data assimilation system. *Mon. Wea. Rev.*, **126**, 1013–1021.

Bell, G. D., and D. Keyser, 1993: Shear curvature vorticity and potential-vorticity interchanges: Interpretation and application to a cutoff cyclone event. *Mon. Wea. Rev.*, **121**, 76–102.

——, and V. E. Kousky, 1995: Diagnosing the midlatitude atmospheric response to ENSO. *Proc. 20th Annual Climate Diagnostics Workshop,* Seattle, WA, NOAA/Climate Prediction Center, 9–12.

——, and M. S. Halpert, 1998: Climate assessment for 1997. *Bull. Amer. Meteor. Soc.*, **79** (May), S1–S50.

——, and M. Chelliah, 1999: The African easterly jet and its link to Atlantic basin tropical cyclone activity and the global monsoon system. *Proc. 23rd Annual Climate Diagnostics Workshop,* Miami, FL, NOAA/Climate Prediction Center, 215–218.

Dlugokencky, E. J., K. A. Masarie, P.M. Lang and P. P. Tans, 1998: Continuing decline in the growth rate of the atmospheric methane burden. *Nature*, **393**, 447–450.

Etheridge, D. M., G. I. Pearman, and P. J. Fraser, 1992: Changes in tropospheric methane between 1841 and 1978 from a high accumulation rate Antarctic ice core. *Tellus*, **44**, 282–294.

Farman, J. C., B. G. Gardiner, and J. D. Shanklin, 1985: Large losses of total ozone in Antarctica reveal seasonal CLOx/NOx interaction. *Nature*, **315**, 207–210.

Gray, W. M., 1984: Atlantic seasonal hurricane frequency: Part I: El Niño and 30-mb quasibiennial oscillation influences. *Mon. Wea. Rev.*, **112**, 1669–1683.

Halpert, M. S., and C. F. Ropelewski, 1992: Surface temperature patterns associated with the Southern Oscillation. *J. Climate*, **5**, 577–593.

——, G. D. Bell, V. E. Kousky, and C. F. Ropelewski, 1996: Climate assessment for 1995. *Bull. Amer. Meteor. Soc.*, **77** (May), S1–S44.

Hofmann, D. J., S. J. Oltmans, J. M. Harris, B. J. Johnson, and J. A. Lathrop, 1997: Ten years of ozonesonde measurements at the South Pole: implications for recovery of springtime Antarctic ozone. *J. Geophys. Res.*, **102**, 8931–8943.

Hurrell, J. W., 1995: Decadal trends in the North Atlantic oscillation: Regional temperature and precipitation. *Science*, **269**, 676–697.

Kalnay, E., and Coauthors, 1996: The NCEP/NCAR 40-Year Reanalysis Project. *Bull. Amer. Meteor. Soc.*, **77**, 437–471.

Keyser, D., and M. A. Shapiro, 1986: A review of the structure and dynamics of upper-level frontal zones. *Mon. Wea. Rev.*, **114**, 452–499.

Kousky, V. E., and M. T. Kayano, 1994: Principal modes of outgoing longwave radiation and 250-mb circulation for the South American sector. *J. Climate*, **7**, 1131–1143.

Landsea, C. W., G. D. Bell, W. M. Gray, and S. B. Goldenberg, 1998: The extremely active 1995 Atlantic hurricane season: Environment conditions and verification of seasonal forecasts. *Mon. Wea. Rev.*, **126**, 1174–1193.

Myhre, G., E. J. Highwood, K. P. Shine, and F. Stordal, 1998: New estimates of radiative forcing due to well mixed greenhouse gases. *Geophys. Res. Lett.*, **25**, 2715–2718.

Reed, R. J., D. C. Norquist, and E. E. Recker, 1977: The structure and properties of African wave disturbances as observed during phase III of GATE. *Mon. Wea. Rev.*, **105**, 317–333.

Reynolds, R. W., and T. Smith, 1995: A high-resolution global sea surface temperature climatology. *J. Climate*, **8**, 1571–1583.

Ropelewski, C. F., and M. S. Halpert, 1986: North American precipitation and temperature patterns associated with the El Niño–Southern Oscillation (ENSO). *Mon. Wea. Rev.*, **114**, 2352–2362.

——, and ——, 1987: Global and regional scale precipitation patterns associated with the El Niño/Southern Oscillation. *Mon. Wea. Rev.*, **115**, 1606–1626.

——, and ——, 1989: Precipitation patterns associated with the high index phase of the Southern Oscillation. *J. Climate*, **2**, 268–284.

Sardeshmukh, P. D., and B. J. Hoskins, 1988: The generation of global rotational flow by steady idealized tropical divergence. *J. Atmos. Sci.*, **45**, 1228–1251.

Simpson, R. H., 1974: The hurricane disaster potential scale. *Weatherwise*, **27**, 169–186.

Spencer, R. W., and J. R. Christy, 1992: Precision and radiosonde validation of satellite gridpoint temperature anomalies. Part II: A tropospheric retrieval and trends during 1979–90. *J. Climate*, **5**, 858–866.

——, ——, and N. C. Grody, 1990: Global atmospheric temperature monitoring with satellite microwave measurements: Method and results 1979–84. *J. Climate*, **3**, 1111–1128.

Trenberth, K., 1990: Recent observed interdecadal climatic changes in the Northern Hemisphere. *Bull. Amer. Meteor. Soc.*, **71**, 988–993.

Wallace, J. M., and D. S. Gutzler, 1981: Teleconnections in the geopotential height field during the Northern Hemisphere winter. *Mon. Wea. Rev.*, **109**, 785–812.

WMO/UNEP, 1994: Scientific assessment of ozone depletion: 1994. WMO Rep. 37. [Available from the World Meteorological Organization, Case Postale No. 2300, 1211 Geneva, Switzerland.]

Xie, P., and P. A. Arkin, 1996: Analyses of global monthly precipitation using gauge observations, satellite summaries, and numerical model predictions. *J. Climate*, **9**, 840–858.

——, and ——, 1998: Global monthly precipitation estimates from satellite-observed outgoing longwave radiation. *J. Climate*, **11**, 137–164.